ADVANCING ANION-EXCHANGE-MEMBRANE WATER ELECTROLYZER

DEVICES: CATALYST LAYER INTERACTIONS, DEGRADATION

PATHWAYS, AND OPERATIONAL DEVELOPMENT

by

GRACE A. LINDQUIST

A DISSERTATION

Presented to the Department of Chemistry and Biochemistry
and the Division of Graduate Studies of the University of Oregon
in partial fulfillment of the requirements
for the degree of
Doctor of Philosophy

June 2023

DISSERTATION APPROVAL PAGE

Student: Grace A. Lindquist

Title: Advancing Anion-Exchange-Membrane Water Electrolyzer Devices: Catalyst Layer Interactions, Degradation Pathways, and Operational Development

This dissertation has been accepted and approved in partial fulfillment of the requirements for the Doctor of Philosophy degree in the Department of Chemistry and Biochemistry by:

Amanda K. Cook	Chairperson
Shannon W. Boettcher	Advisor
Mark C. Lonergan	Core Member
Catherine J. Page	Core Member
Benjamin J. McMorran	Institutional Representative

and

Krista Chronister	Vice Provost for Graduate Studies

Original approval signatures are on file with the University of Oregon Division of Graduate Studies.

Degree awarded June 2023

DISSERTATION ABSTRACT

Grace A. Lindquist

Doctor of Philosophy

Department of Chemistry and Biochemistry

June 2023

Title: Advancing Anion-Exchange-Membrane Water Electrolyzer Devices: Catalyst Layer Interactions, Degradation Pathways, and Operational Development

Water electrolyzers (WEs) are a key technology for a sustainable economy. When powered by renewable electricity, WEs produce green hydrogen, which can be used for energy, fertilizer, and industrial applications and thus displace fossil fuels. Pure-water anion-exchange-membrane (AEM) WEs offer the advantages of commercialized WE systems (high current density, low cross over, output gas compression, etc.) while enabling the use of less-expensive components and catalysts. However, current systems lack competitive performance and durability needed for commercialization, largely limited by the poor stability of anion-exchange polymers used in the membrane and catalyst layers. Further, while non-platinum-group-metal oxygen-evolution catalysts show excellent performance and durability in alkaline electrolyte, this has not transferred directly to pure-water AEMWEs.

The following dissertation is a comprehensive analysis of the fundamental processes that dictate pure-water AEMWE performance and stability. Chapter I introduces AEMWEs in the context of industry-scale devices. Chapter II reports AEMWE cell performance comprising entirely of commercially available materials, detailing the key preparation, and operation techniques. In Chapter III, the structural stability and ionomer

interactions of non-platinum-group-metal (non-PGM) anode catalysts are characterized. The results show catalyst electrical conductivity is key to obtaining high-performing systems and that many non-PGM catalysts restructure during operation, resulting in lower lifetimes. Chapter IV investigates ionomer degradation during device operation, revealing anode ionomer oxidation is the dominant degradation mechanism for all AEM-based electrolyzers tested. Improved device stability using oxidation-resistant catalyst layer binders is shown and new design strategies for advanced ionomer and catalyst layer development are provided. Chapter V provides a summary of the findings in Chapters III and IV and describes the future outlook for advanced catalyst layer development. Lastly, Chapter VI introduces advanced applications for AEMWE systems, detailing technical barriers and possible research approaches to developing AEM electrolyzers for impure-water splitting.

These results significantly improve upon past understanding of pure water AEMWE devices by revealing the fundamental catalyst layer processes resulting in AEMWE device failure under relevant conditions, demonstrating a viable non-PGM catalyst for AEMWE operation, and illustrating underlying design rules for engineering anode catalyst/ionomer layers with higher performance and durability. This dissertation contains previously published and un-published co-authored materials.

CURRICULUM VITAE

NAME OF AUTHOR: Grace A. Lindquist

GRADUATE AND UNDERGRADUATE SCHOOLS ATTENDED:

University of Oregon, Eugene, Oregon
College of Saint Benedict and Saint John's University, St. Joseph, Minnesota

DEGREES AWARDED:

Doctor of Philosophy, Chemistry, University of Oregon
Bachelor of Arts, Chemistry, 2018, College of Saint Benedict and Saint John's University

AREAS OF SPECIAL INTEREST:

Electrochemistry: Membrane Electrolyzer Devices; Water Oxidation Catalysis
Materials Chemistry: Membrane Electrolyzer Devices

PROFESSIONAL EXPERIENCE:

Graduate Employee, University of Oregon, September 2018-June 2023

Research and Development Intern, Nel Hydrogen, January-March 2020

GRANTS, AWARDS, AND HONORS:

Travel Grant, ECS Energy Technology Division, 2023

Featured Scientist, ACS Energy Letters, 2021

Graduate Student Award, ECS Energy Technology Division, 2021

John Keana Graduate Fellowship, University of Oregon, 2021

Graduate Student Award, Renewable Energy Science Foundation, 2020

Dean's First-Year Merit Award, University of Oregon, 2018

PUBLICATIONS:

Lindquist, G. A.; Thompson, W. L.; Gaitor, J. C.; Brogden, V.; Noonan, K. J. T.; and Boettcher, S. W. Oxidative instability of ionomers in hydroxide-exchange-membrane electrolyzers. *Submitted, Energy and Environmental Science.*

Lindquist, G. A. and Boettcher, S. W. Overcoming Limitations for Pure-Water Anion-Exchange-Membrane Electrolysis. *Accepted, Electrochem. Soc. Interface*, 2023.

Marin, D. H.; Perryman, J. T.; Hubert, M. A.; **Lindquist, G. A.**; Chen, H.; Aleman, A.; Kamat, G.; Niemann, V.; Stevens, M. B.; Boettcher, S. W.; Nielander, A. C.; and Jaramillo, T. F. Advancing Prospects for Sustainable Hydrogen with Seawater-Resilient Electrolyzers. *Joule.* 2023, *7*, 1-17.

Krivina, R. A; Zlatar, M.; Stovall, T. N.; **Lindquist, G. A.**; Escalera-Lopez, D.; Cook, A. K.; Hutchinson, J. E.; Cherrevko, S.; and Boettcher, S. W. Oxygen Evolution Electrocatalysis in Acids: Atomic Tuning of the Stability Number for Submonolayer IrOx on Conductive Oxides from Molecular Precursors. *ACS Catal.* 2023, *13,* 2, 902-915.

Krivina, R. A.† and **Lindquist, G. A.**†; Beaudoin, S. R.; Stovall, T. N.; Thompson, W. L.; Twight, L. P.; Marsh, D.; Grxyb, J.; Fabrizio, K,; Hutchinson, J. E.; and Boettcher, S. W. Anode Catalysts in Anion-Exchange-Membrane Electrolysis without Supporting Electrolyte: Conductivity, Dynamics, and Ionomer Degradation. *Adv. Mater.* 2022, *34,* (35), 2203033. †Denotes equal contribution.

Glenn, J. R.; **Lindquist, G. A.**; Roberts, G. M.; Boettcher, S. W.; Ayers, K. A. Standard Operating Procedure for Post Operation Component Disassembly and Observation of Benchtop Water Electrolyzer Testing. *Front. Energy Res.* 2022. 10.

Krivina, R. A.; **Lindquist, G. A.**; Yang, M. C.; Hendon, C. H. Motz, A. R.; Capuano, C.; Ayers, K. E.; Hutchinson, J. E.; and Boettcher, S. W. Ionomer Degradation in Anion-Exchange-Membrane Water Electrolyzers due to Local pH Change Induced by Supporting Electrolytes. *ACS Appl. Mater. Interfaces.* 2022, *14* (16), 18261-18274.

Lindquist, G. A.; Oener, S. Z.; Krivina, R. A.; Motz, A.; Keane, A.; Capuano, C.; Ayers, K.; Boettcher, S. W. Performance and Durability of Pure-Water-Fed Anion Exchange Membrane Electrolyzers Using Baseline Materials and Operation. *ACS Appl. Mater. Interfaces.* 2021, *13* (44), 51917-51924.

Xu, Q.; Oener, S. Z.; **Lindquist, G. A.**; Jiang, H.; Boettcher, S. W. Integrated Reference Electrodes in Anion-Exchange-Membrane Electrolyzers: Impact of

Stainless-Steel Gas-Diffusion Layers and Internal Mechanical Pressure. *ACS Energy Lett.* 2021, *6* (2), 305-312.

Oener, S. Z.; Twight, L. P.; **Lindquist, G. A.**; Boettcher, S. W. Thin Cation-Exchange Layers Enable High-Current-density Bipolar Membrane Electrolyzers via Improved Water Transport. *ACS Energy Lett.* 2021, *6* (1), 1-8.

Sherbow, T. J.; Kuhl, G. M.; **Lindquist, G. A.**; Levine, J. D.; Pluth, M. D.; Johnson, D. W.; Fontenot, S. A. Hydrosulfied-Selective ChemFETs for Aqueous H_2S/HS^- Measurement. *Sens. Bio-Sens. Res.* 2021, *31*, 100394.

Lindquist, G. A.; Xu, Q.; Oener, S. Z.; Boettcher, S. W. Membrane Electrolyzers for Impure-Water Splitting. *Joule* 2020, *4* (12), 2549-2561.

Gordon, B.; **Lindquist, G. A.**; Crawford, M.; Wren, S.; Moore, F.; Scatena, L.; Richmond, G. Diol It Up: The Influence of NaCl on Methylglyoxal Surface Adsorption and Hydration State at the Air-water Interface. *J. Chem. Phys.* 2020, *153* (16), 164705.

ACKNOWLEDGMENTS

technology. Your mentorship and wealth of knowledge started the trajectory of my academic career and built the foundation for my success. Thanks to Dr. Jess Fehrs, Dr. Raina Krivina, and Dr. Tawney Knecht, for your friendship during and beyond our time in lab together, and Dr. Raina Krivina for our partnership in and out of lab.

Thank you to the female scientists who were part of my journey. I am privileged to have too many to name here. I was taught science by women and worked through my chemistry education with women. Because of this I never questioned my right to be here.

I must also acknowledge the CSB/SJU chemistry department, especially my undergraduate research advisor Dr. Alicia Peterson. Thank you for giving me the freedom and encouragement to explore multiple facets at the intersection of science, environmental studies, and policy. Thank you to the 2014 FoCuS cohort (and honorary members from our chemistry community), especially Adrian Demeritte, without whom I likely would not have continued as a chemistry major. To Hannah, Casey, and Sam, I am forever grateful we found each other. Our friendship is a special bond that few experience in their lifetime. I am a better chemist and person because you are in my life.

Thank you to my dance teams Elite Dance Company, the Rebelle Burlesque troupe, and the community at Rebelle Movement dance studio. Thank you for providing me with a space to dance, grow, and escape the bubble of graduate school. Special thanks to Roshny Martuscelli and my Elite teammates for challenging me to think critically about my role in making the world a more loving, accepting place.

Thank you to my church community at Emmaus Lutheran, especially Pastor Rachel, Pastor Andrew, and the Kurr family, for providing me a supportive home in Christ that also aligns with my personal values.

Thank you to my family for supporting me from across the country, especially my parents and brother. I am grateful to the extended Lindquist relatives for raising me with thick skin and teaching me how to make myself heard over the loudest voices in the room. It proved invaluable. Lastly, thank you to my incredible partner Will Parker for your unwavering love and support through the successes and failures of graduate school. You are my home no matter where we are.

To the 2014 FoCuS cohort and our brilliant mentor Adrian Demeritte

TABLE OF CONTENTS

LIST OF FIGURES

Figure   Page

Figure   Page

19

LIST OF TABLES

LIST OF SCHEMES

CHAPTER I

INTRODUCTION: OVERVIEW OF LOW TEMPERATURE WATER SPLITTING TECHNOLOGY

This chapter contains co-authored work published in *ACS Applied Materials and Interfaces* in 2021, *Advanced Materials* in 2022, and co-authored work submitted for publication in *Energy and Environmental Science* in 2023. Reproduced with permission from [*ACS Appl. Mater. Interf.* **2021**, *13*, 44, 51917-51924] and [*Adv. Mater.* **2022,** *34,* 35, 2203033]. The work was organized and written primarily by myself with editorial assistance from Shannon W. Boettcher.

H_2 gas is used as a feedstock for vital industrial processes including ammonia-based fertilizer production, metal-ore refining, and chemical production. [1] It is also of significant interest for energy storage and transportation[2] and central in plans for reducing, and eventually eliminating, CO_2 emissions. [3-4] H_2 gas is often referred to as a "green" energy source, however, is only "green" if powered using renewably produced hydrogen, for example, through water electrolysis powered by wind or solar. Of the 70 Mt (megatons) of hydrogen used globally each year, only ~1% is produced through electrolysis. [5] The rest is essentially all produced from fossil fuels by coal gasification and natural-gas reforming and contributes more than 830 Mt of CO_2 emissions annually. [5]

Green H_2 production brings additional benefits to the renewable technology sector, including longer-duration and increased scale of energy storage compared to batteries, [6] and therefore it has seen substantial investment as political and environmental

factors drive a demand for increased renewable energy use. [1, 7-8] Renewable energy technology typically yields electrical power, which can then be stored or converted to energy carriers such as renewable/green H_2. Green H_2 also enables the otherwise-difficult decarbonization of manufacturing and industry sectors like chemical, metal, and fertilizer production. [9]

Both capital and operating costs must decrease to achieve the electrolyzer capacity required to meet global hydrogen demands. [10] The best technology for this scale up is not yet evident. Of the low-temperature ($> \sim 100$ °C) water-electrolysis technologies, alkaline water electrolysis (AWE) is the most mature. AWE operates in hot, liquid-alkaline electrolyte (~ 80 °C, ~ 5 M KOH) with two electrodes separated by a porous diaphragm. It provides high efficiency and uses earth-abundant non-platinum-group-metal (non-PGM) materials, but is affected in performance and capital expense due to gas crossover through the porous separator and shunt currents through the electrolyte flow paths. [11-12]

Proton-exchange-membrane (PEM) electrolysis is another established technology at megawatt scale[13] with gigawatt pilot projects deployed. [14-16] PEM electrolyzers use perfluorinated sulfonic acid polymers, like Nafion, a cation-exchange ionomer with high H^+ conductivity. [17-18] Membrane-based water electrolysis is often preferred over traditional alkaline liquid-electrolyte technology due to its ability to offer higher-purity H_2, directly compress the evolved H_2, operate at higher current density by minimizing iR losses, and operate efficiently intermittently and with varying load. [19] PEM electrolytes achieve $\sim 80\%$ voltage efficiency at 1 A cm^{-2} or higher[20] and steady-state degradation rates below 20 μV h^{-1}. [19] However, the locally acidic environment necessitates the use of

expensive platinum-group-metal (PGM) catalysts, in particular Ir, which limit device scale-up and deployment.[21] Substantial catalyst loading reductions are needed for PEM to achieve H_2 cost targets.[8]
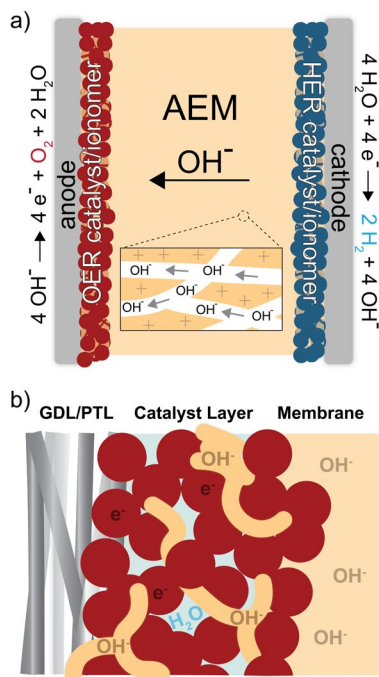
Figure 1.1. Ion transport and reactivity in AEM electrolyzers. Schematics of a) electrolyzer cell and b) anode catalyst layer. OH⁻ anions conduct through the ionomer, and electrons conduct through the catalyst. OER occurs at the ionomer/catalyst interface.

Anion-exchange-membrane (AEM) electrolysis is a developing technology that combines the benefits of AWE and PEM. AEM electrolyzers operate using an anion-selective membrane, which creates a locally alkaline environment ideally enabling operation in water with no supporting liquid electrolyte under differential pressure and the use of non-PGM catalysts and materials[12] enabling the use of inexpensive, earth-abundant catalyst and cell materials (Figure 1.1). However, the mobility of OH⁻ is half that of H^+, and therefore anion-exchange polymers must have twice the charge-carrying

capacity of PEM polymers to achieve comparable conductivity. These transport limitations combined with the poor stability of anion-exchange polymers has prevented AEM electrolyzers from reaching maturity and commercial penetration. [22]

The largest limitations of AEM systems have been membrane and ionomer conductivity and stability. Increasing the ionic conductivity of an AEM usually also increases its solubility and water uptake, [23-25] and thus ionic conductivity is often sacrificed to achieve the required mechanical durability for electrolyzer hardware. In addition to the ionomer (ion-exchange polymer) playing an essential role as the membrane, it is also used in the catalyst layer (Figure 1.1b). The catalyst layer is deposited on the membrane or electrode porous-transport layer (PTL) using an ink. The ink is comprised of the catalyst, solvent, and dissolved ionomer that acts as a catalyst binder and enables ion transport to the active catalyst surface. [26] When the ink is deposited, the solvent evaporates and creates a porous layer of ionomer, catalyst, and void space for liquid/gas transport to/from the catalyst. The interactions between materials in this region directly impact device performance and durability, [27-29] as the impedance of electric, ionic, and reactant/product transport to/from the reaction zone reduces performance. [11]

Commercial PEM electrolyzers operate in pure water at $1.7 - 2$ V at $1.5 - 2$ A cm^{-2} for thousands of hours, with optimized lab-scale devices achieving similar voltages at higher current densities. [30] Most reported AEM electrolyzers operate in carbonate- or hydroxide-based electrolyte that mask the stability issues of the ionomer in the alkaline oxidative environment. Understanding the factors that control performance and durability in the absence of supporting electrolyte is therefore an important immediate goal.

CHAPTER II

PERFORMANCE AND DURABILITY OF PURE-WATER-FED ANION EXCHANGE MEMBRANE ELECTROLYZERS USING BASELINE MATERAIALS AND OPERATION

This chapter contains co-authored work previously published in *ACS Applied Materials and Interfaces* in 2021. Reproduced with permission from [*ACS Appl. Mater. Interf.* **2021**, *13*, 44, 51917-51924]. Copyright 2021 American Chemical Society. The project was conceived by myself, Andrew Motz, Chris C. Capuano, Kathy Ayers, and Shannon W. Boettcher. The experiments were conducted by myself with support from Sebastian Z. Oener, Raina A. Krivina, and Alex Keane. The work was organized, written, and edited primarily by myself with editorial assistance from Sebastian Z. Oener, Chris C. Capuano, Kathy Ayers, and Shannon W. Boettcher.

Introduction

Many previous AEM electrolyzers running in dilute electrolyte or pure water have limited durability and at 2 V provide only a few hundred milliamps per square centimeter. [1-4] Recent work has shown more-competitive AEM performance in pure water, achieving cell potentials below 2 V at 1 A cm^{-2}. [5-7] These studies use custom-made membrane and ionomer materials [5-6] and/or specialized gas diffusion layers (GDLs). [7] Testing protocols have also involved operation in alkaline electrolyte prior to pure water testing. [5-6] Residual electrolyte may affect performance and introduces uncertainty regarding degradation mechanisms associated with the ionomer relative to performance loss due to

flushing supporting electrolyte (see additional discussion and data below in the context of the experiments reported here). Without widely available materials and defined testing protocols, it is difficult to reproduce performance and the field is not accessible to the broader research community.

A significant limitation facing AEM research is the lack of consistent, high-performing, stable baseline materials. Standard PEM systems use Nafion as the membrane and ionomer binder, a Pt black/Toray carbon-paper cathode, and IrO_2/Ti anode. [8] No such baseline materials exist for AEM systems and a wide variety of membranes, ionomers, catalysts, and GDLs are used. [1-3] This impediment is exemplified in the surge of earth-abundant oxygen and hydrogen evolution catalyst research reporting AEM electrolyzer polarization curves obtained under conditions that are not always well-defined and often irrelevant to practical applications, and/or with older membrane chemistries. The use of the AEM–GDL interface in new fields, such as for bipolar membranes, [9-11] could lead to similar problems. The complexity of membrane electrolyzers requires interdisciplinary efforts that leverage baseline materials and well-defined conditions to compare results across studies.

Although materials play a significant role in determining MEA performance and stability, preparation and assembly techniques, as well as electrochemical analysis procedure, are also crucial. Different coating techniques (e.g., airbrush versus hot-press, or coated membranes versus coated GDLs) result in different interactions between the catalyst, ionomer binder, and membrane at the triple-phase boundary. Therefore, large performance differences can be observed across MEAs of identical materials. [12] During electrolyzer operation, different electrolyte pretreatments have also been used, even if

testing in pure water, [5-6, 13] which can also affect measured electrolyzer performance and durability. Here, we detail the preparation and operation of an inexpensive small 1 cm^2 AEM electrolyzer operating with pure water below 2 V at 1 A cm^{-2} using commercially available materials. We use commercial stainless- steel GDLs (original designed as filter media) with a graded porosity, a property that has been previously shown in custom materials to be useful for optimizing membrane-electrolyzer performance. [14-16] We also use an inexpensive hand-held spray-coating gun, instead of a commercial spray-coater, making the approach more widely accessible. The quality of the interface was found to be key for durability. Through initial optimization, we show improved durability reported in pure water at 0.5 A cm^{-2} with the baseline material compared to other available systems and reveal insight into initial degradation pathways, highlighting evidence for ionomer oxidation at the anode. We also show the importance of sufficient pure-water purging of the system if electrolyte pretreatments are used. This baseline MEA configuration, along with baseline fabrication and testing procedures, can be used as a starting reference for further AEM materials development and studies of the underlying basic science phenomena in AEM electrolyzers.

Experimental Methods

Catalyst Dispersions and GDL Coating. Pt black (high surface area, Fuel Cell Store) and IrO$_2$ (Pajarito Powder) nanoparticles were used as the cathode and anode catalyst, respectively. Cathode and anode ink solutions were prepared identically. For every 100 mg of catalyst, 0.5 g of H$_2$O was added, followed by 1.7 g of 2-propanol. The PiperION (TP-85, 5% w/w in ethanol), Sustainion (XB-7 5% in ethanol), and Aemion

28

(AP1-HNN8-00-X) ionomer solutions were used with the corresponding membrane. The Aemion ionomer solid was dissolved in ethanol to yield a 5% w/w solution before ink preparation. Ionomer solution (200 mg of 5% solution in ethanol) was added to yield the final 10 wt % ($w_{ionomer}/w_{catalyst}$) ink. Inks were then bath-sonicated (Branson 1510R-MTH) at room temperature for a minimum of 1 h (Pt black) or 2 h (IrO_2) until fully dispersed.

Toray 090 carbon paper (Fuel Cell Store) and a stainless-steel mesh filter material (25AL3, Bekaert) were used as the cathode and anode GDLs, respectively. The GDL was taped to a hot plate set to 80 °C. Catalyst inks were sprayed onto the GDL materials using an airbrush (Testors, Aztek A2203, part of the "Amazing Airbrush" kit) and compressed N_2 at a pressure of 12 psi. A catalyst loading between 2.3 and 2.8 mg cm^{-2} was determined by mass difference. A thin layer (1−2 wt % $w_{ionomer}/w_{catalyst}$) of ionomer solution in ethanol was sprayed on top of the catalyst layer to improve contact with the membrane. As the quality of the catalyst ink layer has a significant effect on the overall MEA performance, particular attention and care should be paid to the GDL airbrush coating technique. Specific details describing the electrode preparation are included in the Supporting Information.

Membrane Conditioning. PiperION (TP-85 50 and 40 μm, W7Energy), Sustainion (X37-50, Dioxide Materials), and Aemion (AF1-HNN8-50-X, Ionomr) membranes were conditioned according to manufacturer instructions. The membranes were soaked in 0.5 M KOH (PiperION), 1 M KOH (Sustainion), or 3 M KOH (Aemion) for 48 h, replacing the solution with fresh KOH after 24 h. Membranes were stored in 0.5 M (PiperION) or 1 M (Aemion and Sustainion) KOH solution when not in use. The thickness of hydrated

membranes was determined by clamping each membrane between two glass slides and measuring the thickness using a Keyence VHX 7000 digital microscope.

MEA Assembly. The serpentine flow fields can apply an uneven pressure to the relatively flexible SS GDL, so a sintered Ti plate was used as a rigid back support on both the cathode and anode side (400 μm thickness, Baoji Yingao Metal Materials Inc.). Gasket material (0.005 in. PET/PETE clear film, McMaster-Carr) was laser cut to an active area of 1 cm^2. Gaskets were added until they were flush with the GDL surface. The number of gaskets was determined by adding/ removing a gasket until maximum performance was obtained. For this cell, this was determined to be seven total gaskets at the anode and six at the cathode. The Sustainion membrane required one additional gasket at each electrode to prevent the membrane from tearing. The conditioned membrane was dipped in a beaker of 18.2 MΩ cm water then rinsed with 18.2 MΩ cm water for 10 s before assembly. Materials were assembled in the stack and a torque wrench was used to tighten the screws to 5.6 N m.

Electrolyzer Operation. 18.2 MΩ cm water (or in certain experiments 1 M KOH) was flowed to the cathode and anode at 500 mL min^{-1}. N$_2$ was bubbled into the water tank. The anode water flow (carrying produced O$_2$) was recirculated in the system while the cathode water flow (carrying produced H$_2$) flowed into a chemical hood, degassed with N$_2$, then recirculated back into the water tank. Temperature was maintained at the specified value and was monitored with a thermocouple inserted into the cell hardware (Figure A.2). Once the cell temperature was stable, the MEA was conditioned by stepping the current from 100 mA cm^2 to 1 A cm^{-2}, holding for 2 min at each step. The cell was then held at 1 V to test for pinholes or other short-circuit pathways in the cell (the steady-

state electrolysis current decays to zero at <1.23 V, whereas shunt currents persist). The cell was brought back to 1 A cm^{-2} for 2 min to stabilize. The potential was then recorded, and the current was decreased in 100 mA cm^{-2} steps measuring the potential for 10 s at each step to collect the *JV* curve. The cell was held at 500 mA cm^{-2} for stability measurements. Linear sweep voltammetry (LSV) measurements were collected from 1.3−2 V at a scan rate of 20 mV s^{-1}. The full details of all relevant materials and parameters are given in Figure 2.1 and Appendix A.
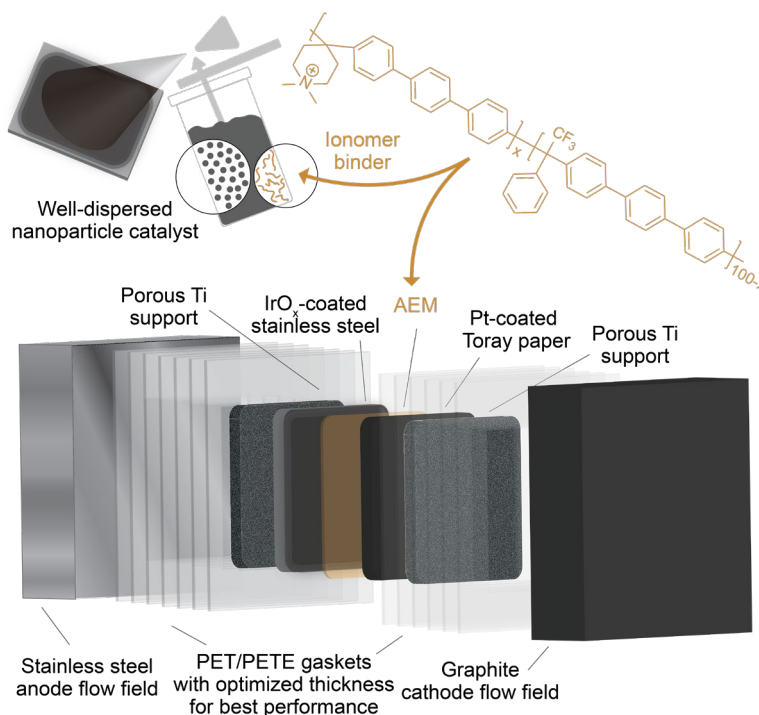
Figure 2.1. Schematic detailing the preparation and assembly of the 1 cm^2 MEA. The small cell size allows for rapid and economical studies of different parameters as well as degradation phenomena, even with a standard potentiostat station. The example here is using the PiperION membrane and ionomer, and the same process was used for the Aemion and Sustainion membranes/ionomers.

Additional Analysis. After operation, the electrolyzer membrane electrode assembly (MEA) was disassembled with the anode and cathode GDLs peeled off the

31
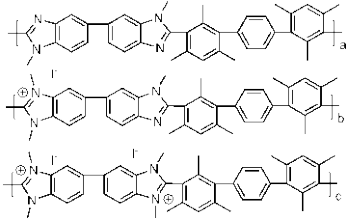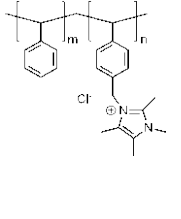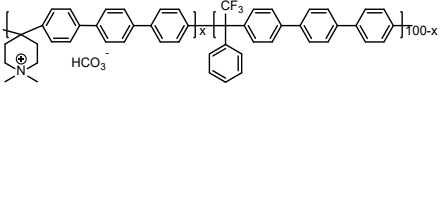
membrane. The anode GDL with remaining IrO$_x$ and PiperION ionomer was dried at room temperature for 48 h and analyzed with X-ray photoelectron spectroscopy (XPS) on an ESCALAB 250 (ThermoScientific) using an Al Kα monochromated (20 eV pass energy, 500 μm spot size) source. The samples were charge neutralized using an in-lens electron source. Spectra were analyzed using ThermoScientific Avantage 4.88 software. The C 1s signal at 284.8 eV was used to calibrate the binding energy scale. The spectra were then compared to the spectra of a pristine PiperION thin film spin-coated from the 5 wt % ionomer solution onto an Au-coated glass slide.

Results and Discussion

The performance of Aemion, Sustainion, and PiperION AEM electrolyzers are shown in Figure 2.2. All tests were operated at the same temperature (55 ± 1 °C). It should be noted that each membrane/ionomer system requires optimized ionomer loading for best performance, which may be different for each system. Here ionomer content was not optimized to any specific membrane, but rather 10 wt % ionomer was chosen to maintain continuity across all membranes. The temperature selected was the highest temperature the Aemion membrane was able to withstand, based on the reported maximum operating temperature of the Aemion membrane. For further validation, the Aemion membrane was operated at 69 ± 1 °C and a rapid performance degradation was observed (Figure A.4). At 100 mA cm^{-2}, membrane resistance and mass transport effects do not substantially contribute to voltage losses and all membranes show nearly identical performance. As current density increases, Aemion and Sustainion continue performing similarly, whereas PiperION out-performs both. The lower hydroxide conductivity of

Aemion[17-19] is likely contributing to its higher voltage performance, specifically, we

hypothesize, at the catalyst interface. Lower hydroxide-ion conductivity is particularly

detrimental at the reactive electrode interfaces, [20] where it may lead to larger voltage

losses than expected from simple ionic membrane series resistance arguments. It should

be noted the hydroxide exchange process was found to have a strong impact on Aemion

performance (Figure A.5). Each membrane arrives with different counterions (Table

2.1)[17-19] that are exchanged for OH^- before electrolyzer operation. Weakly hydrated ions

interact more strongly with the charged end-groups of the AEM[21] and thus require higher

concentrations of hydroxide for ion exchange and can be incompletely exchanged. MEA

Table 2.1. Membrane properties

Membrane	Aemion	Sustainion	PiperION
Ion exchange capacity (meq g^{-1})	2.1-2.5	1.1	2.02-2.37
Reported OH$^-$ conductivity (mS cm^{-1})	>80, no specified temperature	>130* at 70 °C	>135 at 70 °C
Reported % water uptake	33-37%	80%	50%
Dry thickness (μm)**	50	50	50
Wet thickness*** (in KOH, μm)	73	72	62
Chemical structure (including manufacturer-provided counter ion)			

*Reported conductivity is calculated from area-specific resistance (ASR) in 1 M KOH at 60 °C. While Sustainion has a lower IEC, the higher water uptake has been reported to result in a lower ASR leading to the comparable OH$^-$ conductivity value. ** The membranes studied here were all selected because they are commercially available and thus easily accessible. The common thickness for each membrane was 50 um, so this thickness was chosen to keep this parameter constant across all experiments. ***See Figure A.3 for measurement images.

performance is also dependent on the applied hardware pressure;[22] the increased resistance observed with Sustainion might be in part due to the additional gasket material required for Sustainion operation resulting in a higher resistance because of nonideal or nonuniform cell compression.
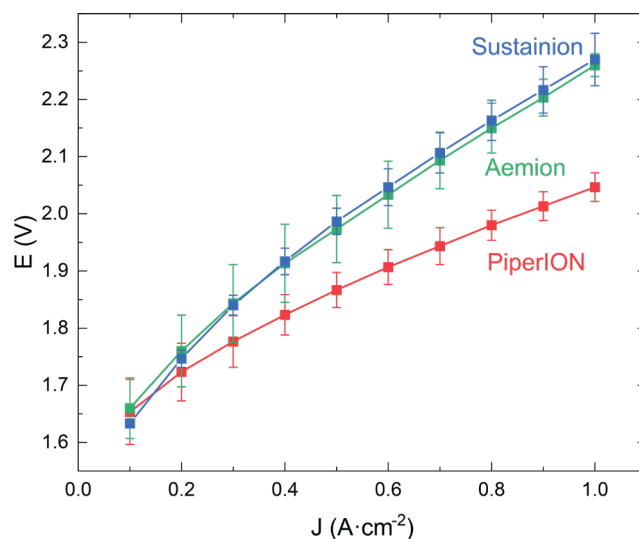
Figure 2.2. Performance comparison of electrolyzers from three commercially available AEMs. All experiments were run with pure water at a cell temperature of 55 ± 1 °C. All membranes are 50 μm thick. Each curve is the average of three individual MEA's tested. Error bars are the standard deviation obtained from three separately fabricated devices.

The temperature dependence of the PiperION membrane was further investigated (Figure 2.3). Although some AEMs are not stable at elevated temperatures,[23] the PiperION membrane operated well at all temperatures tested, and has been reported operating up to 90 °C.[7] The voltage decreases with increasing temperature due to increasing membrane/ionomer OH$^-$ conductivity and improved reaction kinetics.

Various cell conditioning methods were then compared for the PiperION system. Cell conditioning is a well-established practice for PEM electrolyzers and fuel cells,[24-25]

during which the cell is operated and performance gradually improves. [26] Although the

detailed processes that cause this improvement are not fully understood, it is
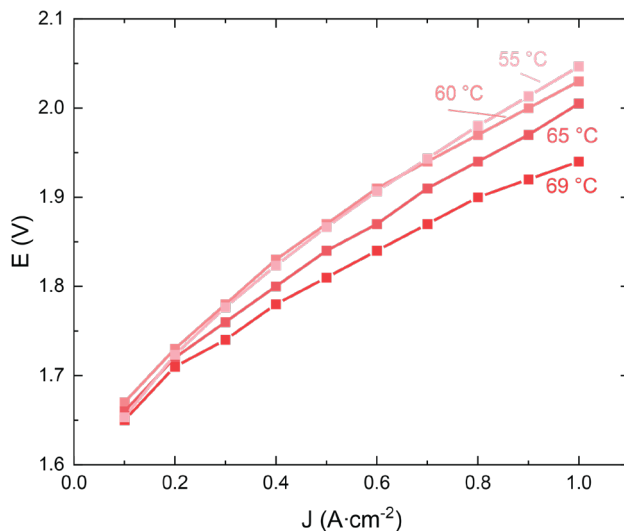
Figure 2.3. Temperature dependence of an electrolyzer operated in pure water with the 50 μm thick PiperION MEA.

hypothesized that cell conditioning further activates catalyst surfaces, more fully hydrates

the membrane and ionomer, and better establishes ion pathways through the membrane

and ionomer. [25, 27-28] In this system, the cell is conditioned in pure water with no soluble

supporting electrolyte by applying current from 100 mA cm^{-2} to 1 A cm^{-2} in 100 mA

steps holding for 2 min at each step. After conditioning, the cell was stepped from 1 A

cm^{-2} to 100 mA cm^{-2} in 100 mA steps holding for 20 s at each step. There is a notable

difference in the time required for the voltage to reach a steady state, as observed in

Figure 2.4a, b. The polarization curves obtained during and after cell conditioning (from

Figure 2.4a, b) were compared by plotting the voltage at 2 min and 20 s, respectively

(Figure 2.4c). There is a significant difference in the low-current-density performance

before and after this initial conditioning period. This highlights the importance of sufficient cell conditioning prior to data collection.

Another commonly used process for pure-water AEM electrolyzer operation is to condition the cell in alkaline electrolyte, purge the cell with pure water, then measure the performance. [5-6] We compared this method to that used here. After conditioning and collecting a polarization curve using the current-step method, an LSV was collected at 20 mV s^{-1} from 1.3 to 2 V. As can be seen, these results agree well, showing that after
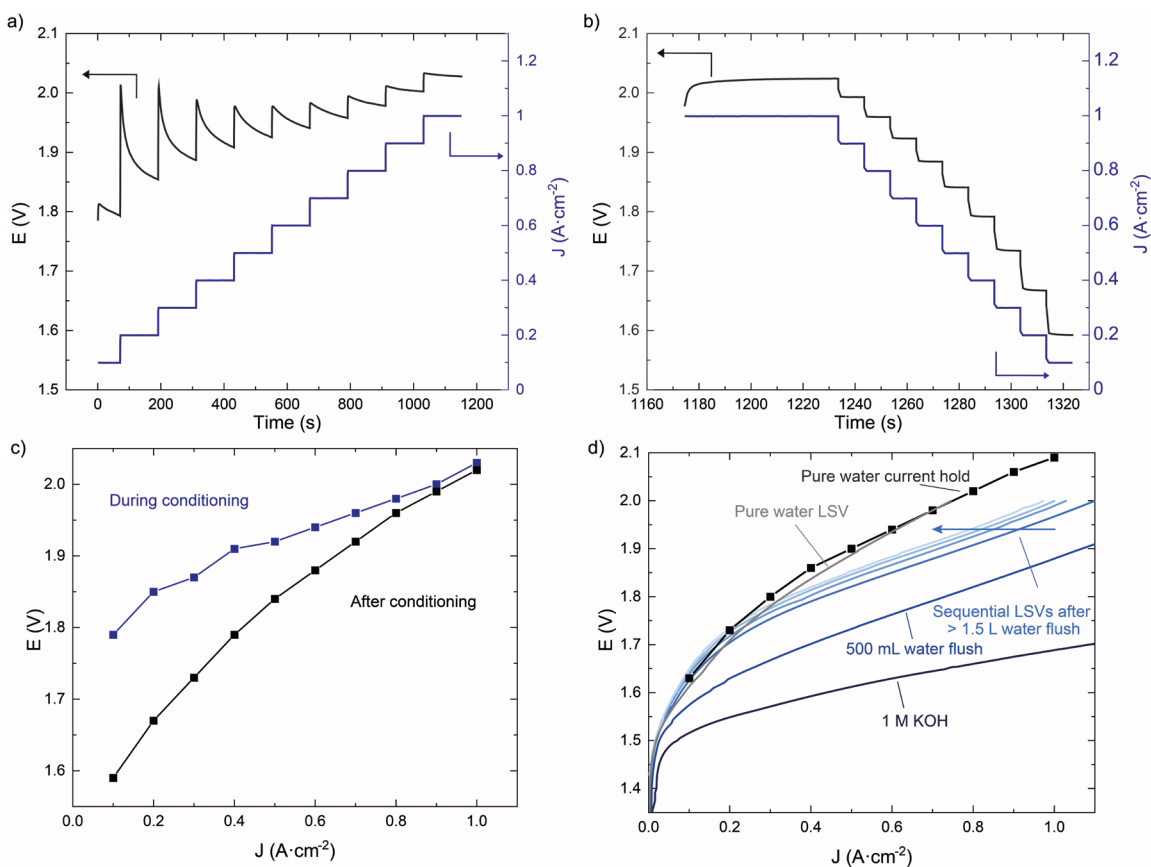
Figure 2.4. Effect of cell conditioning on polarization curves. Voltage changes over time when stepping current (a) at cell start-up and (b) after completing cell break-in. (c) Comparison of polarization curves collected during and after electrolyzer conditioning. (d) Comparison of polarization curves at various points when conditioning in 1 M KOH. All data were collected at 55 ± 1 °C with either a (a–c) 50 μm or (d) 40 μm thick membrane.

sufficient conditioning there is no significant difference in electrochemical technique used to collect the polarization curve. Next, 1 M KOH was flowed to both the cathode and anode and an LSV was collected. The full polarization curve in 1.0 M KOH up to 2 V resulting in $\sim 4\,\mathrm{A\,cm^{-2}}$ of current is included in Figure A.6. Then, pure water was returned to the cell, and an LSV was collected after 500 mL of water was purged through the system (following the procedure used by Li et al.).[5] The performance obtained using this method is significantly better than that obtained by conditioning in pure water. After collecting this LSV, the conductivity of the effluent electrolyte was measured over time. The effluent conductivity was still decreasing, even after >1 L of pure water was flowed through the cell (Figure A.7); therefore, this enhanced performance is attributed to residual KOH that was not sufficiently purged. After pure water was flowed for an additional 3 min (an additional 1.5 L of water) and the conductivity of the effluent was stable, four sequential polarization curves were collected (Figure 2.4b). To stabilize the polarization curves, we needed >2.5 L of pure water to flow through the small 1 cm^2 electrolyzer, yet the voltage was still lower than the recorded pure-water baseline (without KOH flow for pretreatment). This result shows that performance enhancements from conditioning in hydroxide-containing electrolyte might not be completely attributed to residual OH$^-$ in the system.

The residual performance increase after extensive pure water purging might be due to more-complete exchange of OH$^-$, for example, because of removal of residual carbonate species in the ionomer or membrane that increases the ionic conductivity of the ionomer in the catalyst layer.[29]

The lower swelling conditions of the conductive electrolyte might also create a more favorable environment for the catalyst−ionomer interaction during conditioning. We note that all pure water entering the electrolyzer was purged with N_2, whereas the KOH solution was not purged. Although this effect is complex and requires further investigation, the results clearly show the importance of ensuring data are being collected in true pure- water conditions if using a conductive electrolyte for conditioning and that previously reported high-performance "pure-water" experiments are likely influenced by residual KOH. [5]
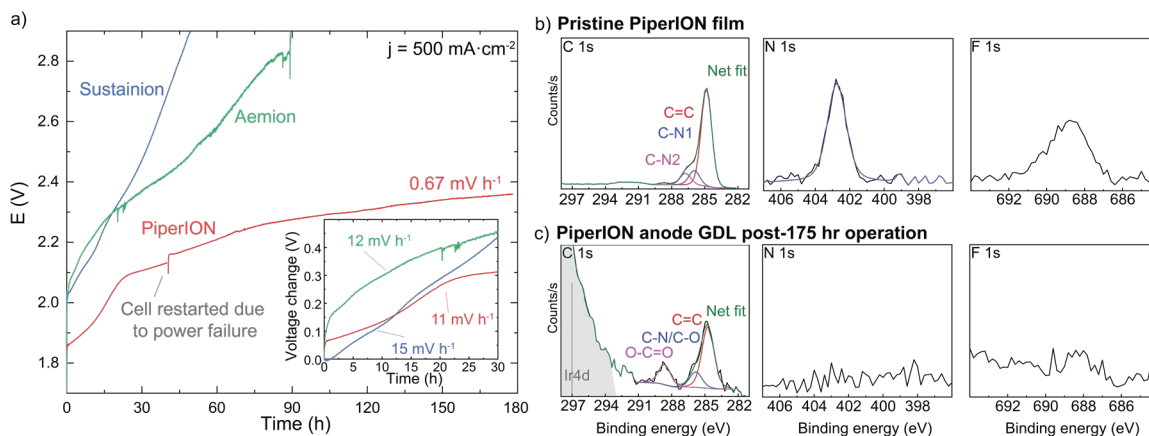
Figure 2.5. Durability testing of commercial AEM MEAs. (a) Stability comparison of the three commercial AEMs when operating at 500 mA cm^{-2} at 55 °C in the electrolyzer. Experiments were ended when the total cell voltage exceeded 2.9 V. All membranes display a similar degradation rate for the first ∼20 h (inset). b) XPS of a pristine PiperION film and (c) PiperION anode GDL surface after 175 h of operation showing substantial evidence of oxidized carbon and loss of N and F.

The stability of each membrane was evaluated over 175 h of operation at 0.5 A cm^{-2} (Figure 2.5). Over the first ∼20 h, all membranes show similar fast degradation rate of 11−15 mV h^{-1} (Figure 2.5 inset), indicating a similar degradation mechanism. After this initial "break-in" the PiperION system stabilizes. This MEA was continuously operated for over 175 h with a degradation rate of 0.67 mV h^{-1} over the last 20 h. The

Aemion and Sustainion systems were shut down when the cell voltage exceeded 2.9 V. Although it is possible that these systems stabilize in a similar manner to PiperION, the system voltage is too high for energy-efficient operation.

Membrane and ionomer degradation are complex processes that are still not fully understood, and there are potentially multiple different degradation pathways contributing. [30] The stability tests were purposefully conducted at conditions that can be easily reproduced by other groups. To begin understanding the source of degradation of the PiperION system, after conditioning and operation in pure water, we then flowed 1 M KOH to the anode and cathode and observed the change in voltage (Figure A.8). After introducing electrolyte, the degradation rate increased from 24 to 87 mV h^{-1}. Further, black particulates were observed in the cathode stream, indicating mechanical failure of the cathode. We hypothesize this is either attributed to the sudden increase in electrolyte conductivity shocking the cathode ionomer or a degradation mechanism influenced by the increasing hydroxide concentration or K$^+$ counterions, leading to breakdown and catalyst detachment. Such effects would not affect the durability during continuous pure water operation and therefore are probably not contributing to the observed degradation discussed previously. After, pure water was purged through the system for 10 min and then the voltage was recorded again in the pure-water conditions (red line until 0.5 h in Figure A.8). The total voltage rapidly exceeds the previous values obtained during the initial pure water operation (black trace), indicating further anode ionomer degradation after that which had already occurred during the initial pure water operation (black trace). We then flowed KOH to the anode only (red trace after 0.5 h in Figure A.8), and the degradation rate decreased from 96 to 40 mV h^{-1} (Figure A.8), suggesting that the

39

increased conductivity with the KOH compensates for the loss in conductivity from the degrading ionomer.

To further investigate this degradation, we disassembled the PiperION MEA after 175 h of steady-state operation in pure water and collected XPS on the anode GDL surface, which remained coated with catalyst and ionomer after disassembly (Figure 2.5c). Additional C peaks associated with oxidized species along with a loss of F and N signal compared to a pristine PiperION film were found (Figure 2.5b), demonstrating the ionomer in this region is undergoing significant oxidative damage. More research is essential to understanding the impact of oxidizing electrode potentials on the specific ionomers, among other effects such as CO_2 poisoning (and CO^{2-} formation).
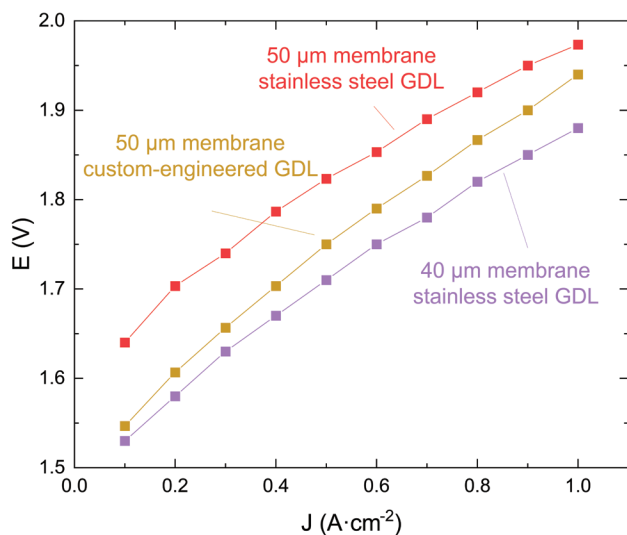
Figure 2.6. Improvements to baseline performance using enhanced materials. All cells were operated at 69 ± 1 °C. All cathode materials remained unchanged. The anode catalyst is IrO_2 on the designated GDL material.

The MEA described here is a starting baseline for further AEM materials development. Examples of improvements are shown in Figure 2.6 using custom GDL and thinner membrane materials. The 40 μm thick membrane shows ~100 mV improvement

across all current densities. Proprietary Ti-based GDLs engineered to improve mass-transport and decrease system resistance for acidic PEM electrolyzers were obtained from Nel Hydrogen. When replacing the commercial stainless- steel GDLs with this material, a similar improvement of 90 mV is observed at 100 mA cm^{-2}, but only 30 mV at 1 A cm^{-2}, indicating that resistive losses, likely in the catalyst/ionomer layers, are more important at high current densities. A lower resistance was observed with the 40 μm thick membrane as indicated by the decreased slope. The improved performance might also be due to improved water management at the electrode interfaces creating and maintaining a better ionomer/catalyst interface.[9]

Conclusion

We described the materials and preparation technique for baseline AEM pure-water electrolyzers with state-of-the-art performance and durability, although substantial improvements are still needed for commercial relevant performance. The baseline AEM system performs below 2 V at 1 A cm^{-2} and was tested for >175 h reaching a final degradation rate below 1 mV h^{-1} in pure water at 0.5 A cm^{-2}. We further demonstrated the importance of proper cell conditioning before data collection to ensure true pure-water performance is reported. All materials are commercially available and the cell size is small, making this performance an accessible baseline to the research community for further development. Operation using improved GDLs and a thinner membrane are shown as examples for future improvements. These examples highlight that improving OH$^-$ conductivity, mass transport, and long-term ionomer stability are key issues for developing commercially relevant pure-water AEM electrolyzers.

CHAPTER III

ANODE CATALYSTS IN ANION-EXCHANGE-MEMBRANE ELECTROLYSIS WITHOUT SUPPORTING ELECTROLYTE: CONDUCTIVITY, DYNAMICS, AND IONOMER DEGRADATION

Raina A. Krivina,† Grace A. Lindquist,† Sarah R. Beaudoin, Timothy Nathan Stovall, Willow L. Thompson, Liam P. Twight, Douglas Marsh, Joseph Grzyb, Kevin Fabrizio, James E. Hutchison, and Shannon W. Boettcher

†These authors contributed equally to this work

This chapter contains co-authored work previously published in *Advanced Materials* in 2022. Reproduced with permission from [*Adv. Mater.* **2022,** *34,* 35, 2203033]. Copyright 2022 Wiley-VCH. Raina A. Krivina, myself, and Shannon W. Boettcher designed the study, analyzed the data, and wrote the manuscript. Raina A. Krivina collected and analyzed all XPS with the support of T. Nathan Stovall. Raina A. Krivina and myself collected and analyzed three-electrode electrochemical measurements with the support of T. Nathan Stovall and Liam Twight. I performed and analyzed all electrolyzer MEA and conductivity measurements with the support of Sarah R. Beaudoin and Willow L. Thompson. Doug Marsh and Joseph Grzyb collected ICP-MS samples. Liam Twight conducted ICP-MS analysis. Kevin Fabrizio conducted gas adsorption experiments for catalyst surface area analysis. James E. Hutchinson provided intellectual

advisement. The work was written, organized, and edited by myself and Raina A. Krivina with editorial assistance from Shannon W. Boettcher.

Introduction

Most AEMWE testing is conducted with expensive IrO_2 oxygen evolution reaction (OER) catalyst because it is stable and active. [1-3] In alkaline electrolyte, however, Ni–Fe oxyhydroxides have the lowest overpotential and highest per-cation turn-over frequency in three-electrode studies. [4-6] The performance and durability of Ni–Fe oxyhydroxides has generally been poor in pure-water membrane-electrode-assembly (MEA) configurations, however, which we have attributed to difficulties in oxidizing the bulk of the catalyst to its active state without soluble electrolyte. [3] Recently, non-PGM catalysts have shown more-promising performance and durability in MEA configurations, but appear to require either supporting electrolyte[7-9] or complex electrode and/or catalyst design and preparation, [10] for example, with the Ni–Fe catalyst supported on a high-sur-face-area Ni foam, that may not be easily translated to commercial-scale devices. [11-15] These studies are often further complicated by membrane and ionomer instability that causes degradation independent of catalyst identity. Very few studies have investigated the catalyst-level phenomenon that modulates apparent durability, especially in industry-relevant MEA conditions. Recent developments in AEM ionomer and MEA preparation and assembly have improved AEMWE durability, [1-2, 12] making it possible to better isolate the role of metal-oxide catalysts in system degradation.

Here, we study five Ni-, Co-, and Fe-oxide-based nanoparticle anode catalysts and compare them to commercial nanoparticle IrO_2 in pure-water AEMWEs to understand the

fundamental factors controlling the performance and durability of non-PGM materials in industry-relevant designs. Using operando analysis and post-operation materials characterization, particularly by X-ray photoelectron spectroscopy (XPS) of the catalyst layer, we observe multiple processes contributing simultaneously to degradation. We show differences in structure dynamics of the anode catalysts driven via operation and how catalyst restructuring processes affect the device performance. We find that the introduction of soluble Fe species during device operation accelerates degradation. Finally, we demonstrate a device using a Co_3O_4 anode with comparable performance and durability to IrO_2, proving a viable route for non-PGM operation at scales where IrO_2 may not be viable due to scarcity.

Results and Discussion

AEMWE Performance and Durability.

AEMWE devices were constructed for each catalyst following published procedures[1] (see Experimental Section). Catalysts were dispersed in an ink of isopropyl alcohol, water, and ionomer and sprayed onto gas-diffusion-layer (GDL) substrates. Commercial nanopowders (IrO_2, Co_3O_4, NiO, $NiCoO_2$, $NiFe_2O_4$, and $Ni_{0.5}Co_{0.5}Fe_2O_4$) were used as anode catalysts (Table 3.1) and Pt black as the cathode catalyst.

Anode catalysts were sprayed onto a stainless-steel woven mesh and cathode catalysts on Toray-090 carbon paper. The loading for all catalysts was between 2.2 and 2.7 mg cm^{-2} with 10% by weight ionomer content. A thin layer (2–5 wt% relative to catalyst loading) of ionomer was sprayed on top of the catalyst layer. The MEAs were constructed using a 40 µm thick PiperION TP-85 membrane and compressed with a

torque on the assembly bolts of 5.6 N m. Water (at 60 °C) was pumped to the anode and

cathode at 125 mL min^{-1} until the hardware temperature equilibrated to 57 °C. The cell

was conditioned prior to data collection as described in the Experimental Section. Figure

B.1 shows a photo of the electrolyzer system and a schematic of the MEA components.

Table 3.1. Anode catalyst properties.

Catalyst	Diameter [nm]	Surface Area [m^2 g^{-1}]	σ [mS cm^{-1}]
IrO$_2$	5-10	14.1 ± 0.1	metallic*
Co$_3$O$_4$	30-50	28.0 ± 0.1	30 ± 6
NiO	15-35	32.4 ± 0.1	4 ± 3
NiCoO$_2$	20	19.5 ± 0.1	0.9 ± 0.4
Ni$_{0.5}$Co$_{0.5}$Fe$_2$O$_4$	40	57.7 ± 0.3	0.004 ± 0.005
NiFe$_2$O$_4$	20	69.6 ± 0.5	0.02 ± 0.01

*measurement indistinguishable from contact resistance

First, the performance and durability of each catalyst was assessed during pure-

water electrolyzer operation. IrO$_2$ out-performed all other catalysts by ~100 mV at 10 mA

cm^{-2} (Figure 3.1a). At such a low current density, Ohmic and mass-transport losses

should be minimal, and performance is largely dominated by the OER overpotential. As

current density increases, the performance more closely compares to the next-best

catalysts, Co$_3$O$_4$ and NiO, which are within 50 mV of IrO$_2$ at 1 A cm^{-2}. All tested mixed-

metal catalysts displayed worse performance. To investigate the origin of this trend, gal-

vanostatic electrochemical impedance spectroscopy (GEIS) was conducted at 50 mA cm^{-}

^{2} immediately after cell conditioning (Figure 3.1b). The data were fit to a Randle's circuit

with constant phase elements (Figure 3.1b inset). All cells show comparable high-

frequency series-resistance, and thus the performance discrepancies are not attributed to

differences in materials/cell-assembly conditions, for example, contact between the catalyst layer and membrane or in the ink-dispersion quality. The trend in low-frequency resistance, assigned to charge-transfer phenomena, agrees with the voltage trend observed at 50 mA cm^{-2}, as expected. IrO_2 and Co_3O_4 also showed the best durability over 20 h, stabilizing to a degradation rate of 2.6 and 1.8 mV h^{-1}, respectively (Figure 3.1c). While NiO showed similar performance, an initial rapid degradation was observed before the electrolyzer stabilized to a degradation rate of 6.4 mV h^{-1} at a ~200 mV higher voltage than IrO_2 and Co_3O_4. Fe-containing catalysts showed exceptionally high degradation rates, with $NiFe_2O_4$ surpassing 5 V after only ~4 h. Although Ni–Fe-oxide-based catalysts substantially outperform IrO_2 in alkaline three-electrode-cell tests, [4, 6] in a pure-water-fed MEA with an alkaline catalyst/ionomer environment, the trend in performance appears reversed.

We tested the same inks used to coat GDLs (catalyst inks with 10 wt% ionomer) on quartz-crystal electrodes in 1.0 m KOH (Figure 3.1d) to identify differences between MEA and soluble electrolyte environments for catalysis. IrO_2 and Co_3O_4 still outperform the Ni–Fe-oxide catalysts. In our previous studies, we used less-crystalline Ni–Fe-oxide thin films that converted to the $M^{3+/4+}$ oxyhydroxide state rapidly during operation, leading to dramatically increased activity. [4, 6] The Ni–Fe nanopowdered oxide catalysts used for the MEA configuration might not easily convert to the more-active oxyhydroxide phase due to low electronic conductivity and, in the MEA, lack of soluble electrolyte that can penetrate the layered structure. Thus, the activity trend observed in prior thin-film studies cannot be directly translated to an ionomer environment in an MEA configuration.
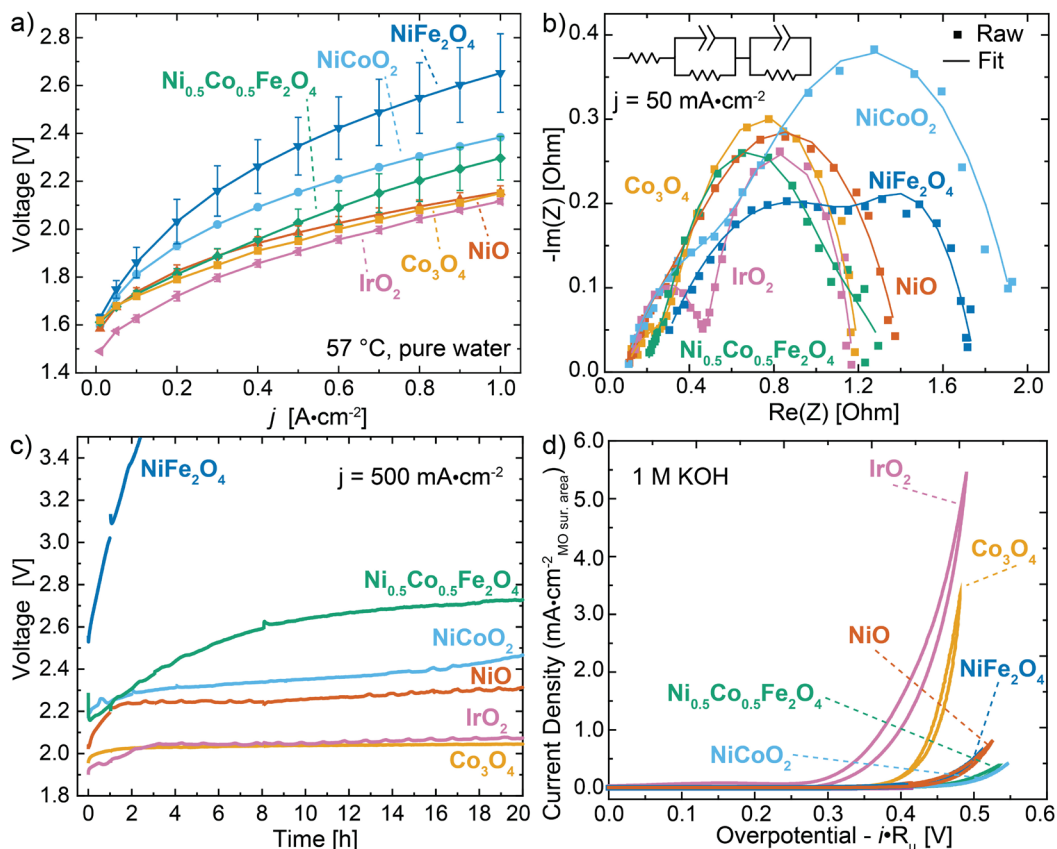
Figure 3.1. Electrochemical performance. a) Polarization curves of anode catalysts tested. All experiments were conducted in pure water at 57 °C. A stainless-steel woven substrate with the indicated catalyst was used as the anode GDL and Pt black catalyst on Toray carbon paper was used as the cathode GDL. Data with *iR* correction is included in Figure B3. Sample size $n = 3$; data presented as mean ± one standard deviation. b) GEIS (at 50 mA cm–2) for each catalyst tested in the pure-water MEA for a single representative device. The inset shows the equivalent circuit used for data fitting. c) Durability testing for each catalyst held at 500 mA cm–2 for 20 h at 57 °C for a single representative device. Duplicate MEAs are included in Figure B.4. d) Cyclic voltammetry for catalysts embedded in anion-exchange ionomer (10 wt%) tested in 1.0 m KOH on Au/Ti quartz-crystal-microbalance electrodes. The current density is calculated using the BET surface areas of the nanopowders. The overpotential was corrected for *R*u (3.0–3.6 Ω). The first CV cycle for one representative electrode is shown for clarity; replicate measurements with additional cycling are shown in Figures B.5 and B.6.

The conductivity of the anode layer has significant impact on AEMWE performance. [16] The electrical conductivity of each catalyst was measured by pressing each catalyst powder between two stainless-steel disks under 23000 psi and collecting a

polarization curve. Catalyst performance at 1 A cm^{-2} follows electrical conductivity (Figure 3.2), indicating that the worst-performing catalysts suffer from limited available active sites due to a poor electron transport through the catalyst layer. A similar experiment was conducted with several Co-based anode catalysts measuring electronic conductivity in a catalyst/ionomer layer as opposed to pressed powders and a similar trend was observed (Figure B.10 and Appendix B Methods). The ionomer environment, in combination with low-conductivity catalyst, may impede the conversion of the Ni–Fe-oxide catalysts into the more active oxyhydroxide form, which is more conductive and would ensure better electrical conductivity between the catalyst particles and the GDL.
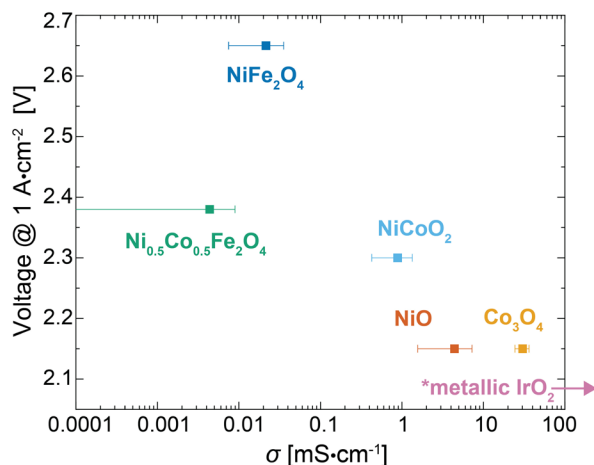
Figure 3.2. Electrical conductivity of non-PGM catalysts. Conductivity was measured by compressing the powders into a pellet (23000 psi) and measuring electrical resistance while under compression from the slope of a polarization curve. The resistance measured for the IrO$_2$ pellets was comparable to the contact/wire resistance, and thus IrO$_2$ is simply labeled as metallic (Figure B9). Sample size $n = 3$; data presented as mean ± one standard deviation.

Several important points are evident from these data: i) IrO$_2$ and Co$_3$O$_4$, the most electronically conductive of the catalysts tested, have superior performance in the pure-water-fed system, ii) the least-conductive, Fe-based catalysts, which have superior

alkaline OER kinetics after restructuring to oxyhydroxides, [4, 6] perform the worst, and iii)

mixed-metal and Fe-containing catalysts show significantly worse stability than single-

metal, non-Fe-based catalysts.

Many processes could be contributing to these observed performance and

durability trends. The ionomer in the catalyst layer might be degrading, for example,

undergoing oxidation via direct contact with the catalyst surface and thus OER inter-

mediates. The extent of this degradation would likely vary based on catalyst properties,

such as electronic conductivity and sur-face chemistry. The catalysts are also likely

restructuring during oxidation, affecting the catalyst/ionomer interface or leaching metals

causing the loss of active sites and voids in the catalyst layer or at the catalyst/ionomer

interface. Dynamic metal sites, for example, soluble Fe species dissolved from the GDL

or catalyst layer, might leach into the system where they could redeposit to block catalyst

active sites, block OH^- transport to the anode, be transported further into the MEA and

decrease bulk membrane OH^- conductivity, or cross fully to the cathode where they could

deposit or block ion transport. Each of these possible degradation mechanisms was

investigated.

Ionomer Degradation by the Catalyst Surface

To investigate damage occurring to the ionomer in the anode catalyst layer, the

compressed AEMWE cells were disassembled and the anode GDLs were analyzed with

XPS. Upon disassembly, the solid membrane was pulled away from the GDL exposing

the leftover catalyst powder embedded in the ionomer directly in contact with the

catalyst. These post-operation GDLs were soaked in 3.0 M NaCl to ion-exchange OH^- for

Cl$^-$ to avoid further degradation post-operation from OH$^-$ whose nucleophilicity increases with drying.

Previous studies have shown that the ionomer binder directly in contact with the catalyst layer oxidizes under operating potentials at the anode with IrO$_2$. [1, 17] However, the mechanism by which this oxidation occurs is poorly understood. [1, 18-19] Oxidation could be occurring directly at the catalyst/ionomer surface or chemically through reactivity with OER intermediates or other reactive oxygen species formed, for example, through radical reactivity. [20-21] These degradation phenomena may or may not depend on catalyst type. Others have suggested that degradation rates correlate with ionomer/catalyst interaction strength, [22] and the adsorption energies of ionomer functional groups to the catalyst surface are expected to vary for different oxide catalysts. If degradation is occurring by chemical reactivity with OER intermediates, degradation may depend on catalyst activity and OER mechanism. Furthermore, AEM ionomers will oxidize at sufficiently high voltage regardless of catalyst/electrode surface, [17] thus degradation may only depend on device operating voltage.

The extent of the ionomer oxidation by the six catalysts was assessed by XPS. The chemical structure of the ionomer and membrane used is in Figure 3.3a. The C 1s, N 1s, and F 1s spectra were collected on the pristine catalyst/ionomer ink and port-mortem GDLs after 20 h of operating at 500 mA cm^{-2} (Figure 3.3b). The changes to the shape and interact with the surrounding ionomer differently. During operation with Co$_3$O$_4$ at the anode, the XP spectra of the ionomer do not change substantially. The N 1s peak that
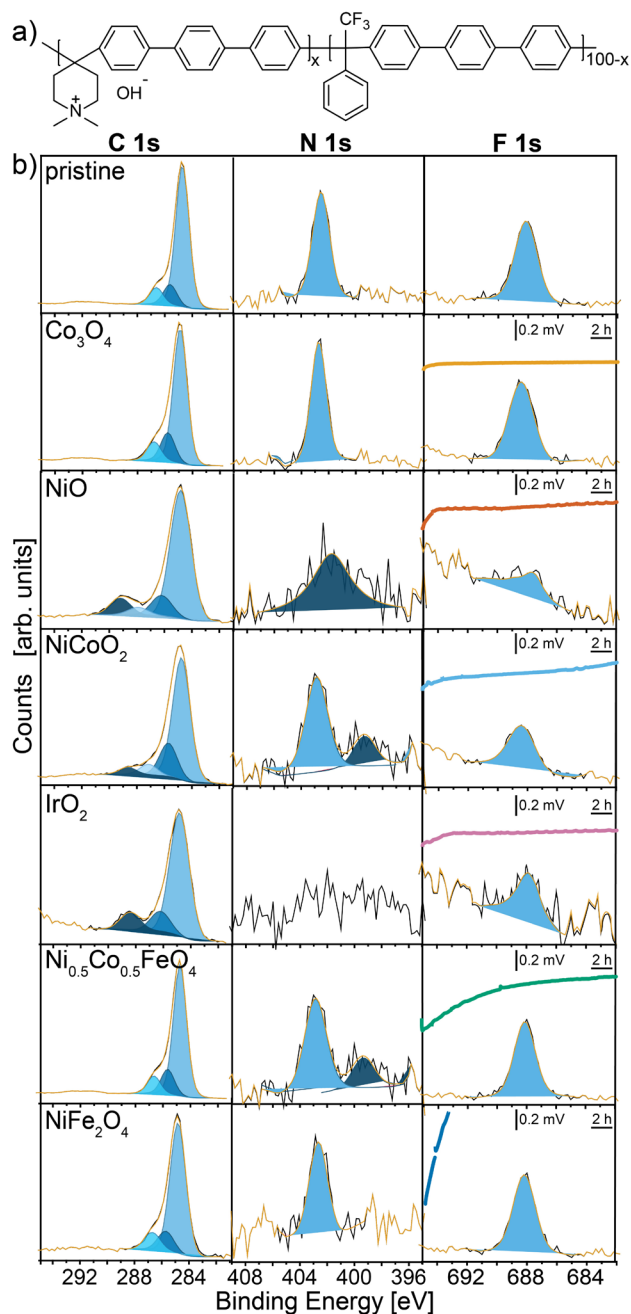
Figure 3.3. Catalyst-dependent ionomer degradation. a) Chemical structure of the membrane/ionomer used in this study (PiperION by Versogen, PAP-TP-85). b) XP spectra of C 1s, N 1s, and F 1s peaks collected on the pristine anode catalyst-coated GDLs and the post-mortem GDLs after 20 h of operating at 500 mA cm^{-2} in pure water for a representative device with each catalyst type. Durability data from Figure 3.1c is overlaid on the F 1s spectra for reference.

represents the charge-carrying groups in PiperION retains its position and shape. The XP

spectra of the ionomer interacting with IrO_2, on the other hand, undergo significant

chemical changes. A new high-binding-energy peak emerges at 288.4 eV after 20 h of

operation and the N 1s peak vanishes. The F 1s peak also diminishes.

As 20 h is a short durability test, one Co_3O_4 device was further operated for 250 h

(Figure 3.4). The performance is similar to what has been previously observed for IrO_2

with both MEA's stabilizing to degradation rates <1 mV h^{-1} after 150 h. [1] The C 1s region

shows significant changes, comparable to that of IrO_2 after a long-term operation. [1] We

also analyzed a separate MEA operated for 57 h (Figure B.11), which showed slightly

less oxidative damage.

The variability in ionomer oxidation rates between Co_3O_4 and IrO_2 at short time

scales may be explained by the difference in the catalysts' electronic conductivity.

Catalyst surfaces are known to facilitate ionomer degradation, either through the polymer

interactions with OER intermediates or by direct oxidation through functional groups

adsorbing onto the catalyst surface. [21-23] A more electrically conductive catalyst could

oxidize the bulk of the ionomer faster due to lower Ohmic voltage losses through the

percolative electronic transport pathways in the catalyst, while less-conductive catalysts

might only be able to oxidize the ionomer closer to the GDL where electronic Ohmic

losses are small and high oxidizing potentials remain available.

The next two most-stable catalysts, NiO and $NiCoO_2$, also facilitate ionomer

degradation: new high-energy peaks appear in the C 1s spectra; N 1s shifts in energy and

diminishes; F 1s also decreases in intensity (Figure 3.3b). This could be attributed to

ionomer degradation due to the higher operating voltage, but the XPS of the two worst-

performing catalysts, NiFe$_2$O$_4$ and Ni$_{0.5}$Co$_{0.5}$Fe$_2$O$_4$, showed less changes to the ionomer

structure than for NiO and NiCoO$_2$ despite operating at a higher cell voltage

(Figure 3.3b). Changes are only observed in the N 1s peaks suggesting ionomer

dissolution or changes to the chemical structure of the charge-carrying groups. However,

these changes are small compared to what is observed with the better performing

catalysts like IrO$_2$ or NiO. The XPS analysis of the GDLs is performed on multiple spots

to obtain an averaged picture of the ionomer structure. The NiFe$_2$O$_4$ GDL showed minor

changes to the carbon peak in some of the analyzed spots, but most of the spectra showed

no change.
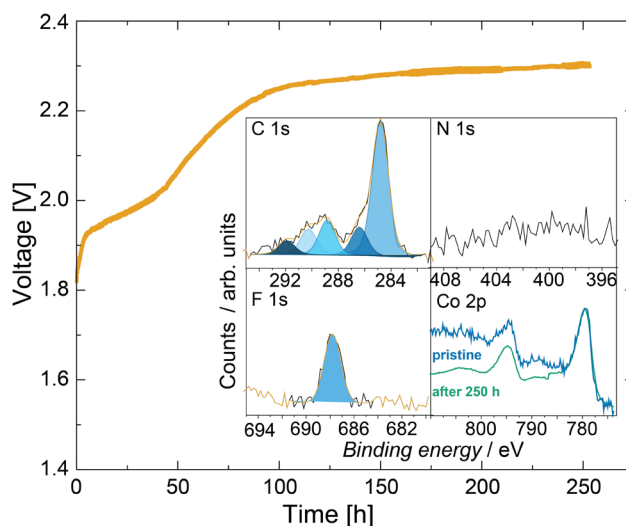
Figure 3.4. Extended durability testing of an AEMWE with a Co$_3$O$_4$ anode catalyst. The cell was operated for 250 h at 500 mA cm^{-2} in pure water at 57 °C. A Pt-black catalyst on Toray carbon paper was used as the cathode. The inset shows XP spectra of the GDL surface after 250 h of operation illustrating severe oxidative damage. Sample size $n = 1$; a control MEA operated for 57 h is included in Figure B11.

These trends may also be explained by the differences in catalyst conductivity.

For catalysts with poor electrical conductivity, only the sites near the electronically

conductive GDL are active, and therefore are also the only region available for ionomer

oxidation. XPS is surface-sensitive and will not detect degraded polymer in direct contact with the GDL if it is covered by a layer of an undegraded ionomer. It is difficult to determine the thickness of catalyst layer being analyzed during XPS. Thus, it might appear that a catalyst does not cause ionomer degradation after the 20 h run when degradation is prevalent directly next to the GDL, but not on ionomer closer to the membrane.

Ionomer oxidation, however, may not be the primary degradation pathway for the Fe-based catalysts. To test this, the $NiFe_2O_4$ catalyst was operated at a constant voltage rather than current. Even when held at 1.8 V, lower than the operating voltage of the best-performing catalyst, the activity of the system degraded rapidly, passing only a few mA of current by the end of the 20 h operation (Figure B.12). The C 1s and N 1s spectra of the ionomer in contact with the catalyst show small changes compared to the pristine material (inset in Figure B.12). These data suggested to us that changes in the catalyst structure and interface with the ionomer must also be considered.

Catalyst Restructuring and Leaching

Non-PGM OER catalysts are known to structurally evolve under operating conditions. [4-5] Co, Ni, and Fe oxides, for example, oxidize during OER typically converting to more-active and electrically conductive layered oxyhydroxides. [6] These catalysts also have dynamic Fe sites that dissolve and re-deposit that are responsible for the superior OER activity. [24-25] For Ni–Fe and Co–Fe oxyhydroxide catalysts, leaching of the metals has been reported. [24] Fe was measured to dissolve at higher rates than Ni or Co in Fe/Ni and Fe/Co oxides/oxyhydroxides, with Ni dissolution being the slowest. [24] These catalysts may also uptake additional ions present in trace amounts in electrolyte.

54
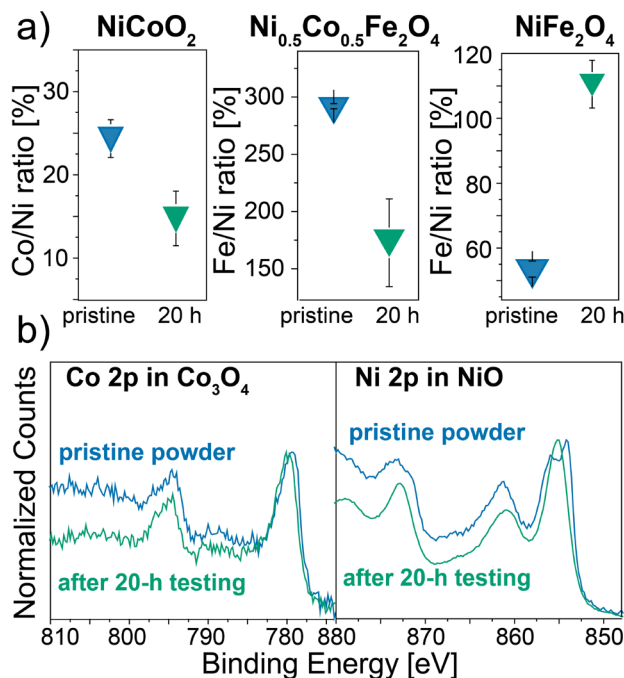
Figure 3.5. Comparison of non-PGM catalyst structure pre- and post-operation. a) The change in metal ratios of mixed-metal catalysts determined by XPS. Sample size $n = 3$; data presented as mean ± one standard deviation. b) XPS spectra of Co 2p in Co_3O_4 and Ni 2p in NiO. All catalysts were operated for 20 h at 500 mA cm^{-2}.

To assess restructuring and leaching in the mixed-metal non-PGM catalyst powders during electrolysis, we measured the metal ratios before and after operation (Figure 3.5a). The ratios determined by XPS are reflective of the surface composition and do not correspond to the overall composition of the nano-powders. For $NiCoO_2$, the initial surface ratio of Co/Ni found by XPS was 0.24 ± 0.02. This ratio decreased to 0.15 ± 0.03 after operation, suggesting that the catalyst is restructuring and/or leaching, forming a Ni-rich surface. The Fe/Ni ratio in $NiFe_2O_4$ increased from the initial 0.54 ± 0.02 to 1.1 ± 0.1 indicating the formation of an Fe-rich top layer. This is likely due to Fe leaching, followed by redeposition on the surface of the catalyst (soluble Fe species are anionic in base, thus prevented from crossing to the cathode by the Ohmic drop across the membrane). The Fe/Ni ratio in $Ni_{0.5}Co_{0.5}Fe_2O_4$, however, showed the opposite trend,

55

decreasing from 2.9 ± 0.1 to 1.8 ± 0.1, but this change was accompanied by a decrease in the Co/Ni ratio (1.0 ± 0.1 to 0.52 ± 0.04) suggesting the formation of a Ni-rich surface. Such composition on the surface is likely the result of Ni restructuring and covering Co and Fe. Co is known to be stable during OER[25-26] and thus Co leaching is unlikely (discussed more below).

For the monometallic oxides (NiO and Co_3O_4), we studied changes in the shape and energy of the metal XPS peaks (Figure 3.5b). The Co 2p peak remained unchanged after 20 h of electrolysis. The shape of the peak is consistent with Co_3O_4.[27] Co_3O_4 is known to form a sub-nanometer amorphous shell during OER, otherwise maintaining crystallinity,[28-29] and a small extent of oxidation may be occurring that is not detected by XPS. The Ni 2p peak shifted to higher binding energy and changed its shape consistent with the transition from NiO to NiOOH.[27] $Ni(OH)_2$ significantly restructures under OER conditions compared to $Co(OH)_2$ which tends to maintain its initial morphology.[26, 30] The change in oxidation state and structure might be accompanied by $Ni^{2+/3+}$ leaching/redeposition. The changes to the catalyst structure likely explain the observed degradation behavior. Catalyst/ionomer interactions influence electrolyzer performance and durability.[23, 31-32] Structural evolution and cation leaching/redeposition likely disrupts the catalyst/ionomer interfaces. For example, as NiO dynamically restructures to form more disordered NiOOH, the physical proximity of the ionomer and catalyst likely decreases, increasing iR and/or decreasing ionic conductivity, leading to higher voltages without observing significant ionomer oxidation by XPS. Leaching of the metal cations and their consequent redeposition on the electrode surface could further disrupt the

catalyst/ionomer network. The lack of restructuring and leaching/redeposition under OER conditions likely contributes to the better durability of Co_3O_4.

The Role of Dynamic Fe Species

Leached ions also can participate in chemical reactions with the ionomer leading to chemical changes (e.g., Fenton-type oxidation reactions). [33-34] Fe is particularly dynamic, and thus the role of soluble Fe ions was further investigated.

To probe the role of soluble Fe species, we intentionally added soluble Fe to the water feed. An MEA with a Co_3O_4 anode was operated for ≈10 h to stabilize, then 1 ppm
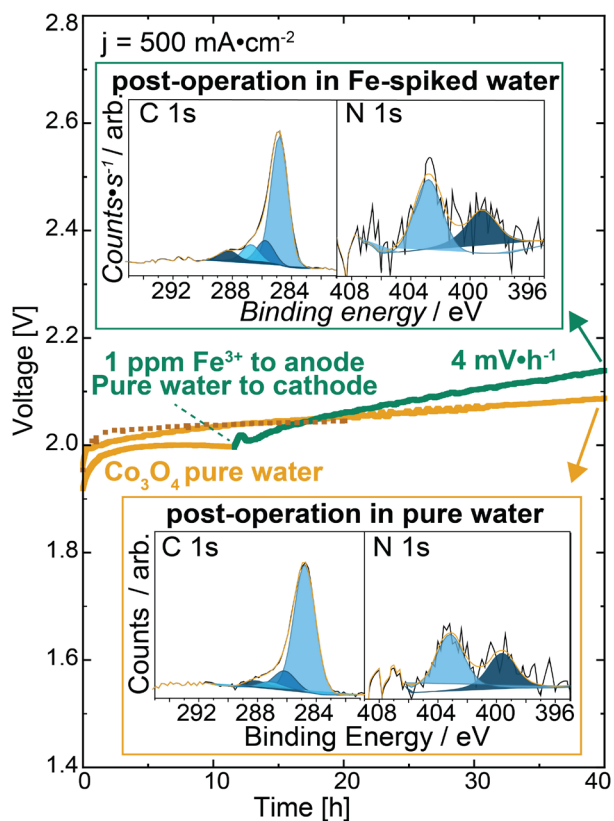
Figure 3.6. Effect of soluble Fe on AEM durability. A device with a Co_3O_4 anode catalyst was operated in pure water until stabilizing (gold), after which the anode inlet was moved to a solution of 1 ppm Fe^{3+} (green trace). The 20 h Co_3O_4 run is shown in darker gold dashed line for reference. Inset: XP spectra of the anode GDL post-Fe spike (top) and pure water (bottom) operation.

Fe^{3+} was flowed to the anode while pure water was maintained at the cathode from a separate pump and water reservoir (Figure 3.6). The Fe increased the degradation rate to ≈ 4 mV h^{-1}. The run was carried out for 40 h, during which the degradation continued at this constant rate. XPS shows significant changes to the C 1s and N 1s spectra. The performance of Co_3O_4 tested for 40 h in the absence of Fe (Figure 3.6, gold) did not degrade as rapidly. However, the XPS analysis of the ionomer at the anode after the 40 h Fe-free run shows nearly identical changes to the C 1s and N 1s peaks (Figure 3.6 inset). As discussed above, Co_3O_4 alone oxidizes the ionomer but at a slower rate compared to IrO_2 (Figure 3.4). One might attribute this new degradation to soluble Fe species crossing the AEM to the cathode where it could block active sites on Pt or otherwise facilitate cathodic degradation, but Fe was not detected on the cathode GDL post-operation by XPS (Figure B.13). Thus, it appears the introduction of Fe is accelerating the degradation in the anode. Soluble Fe ions likely deposit on or adsorb to the anode catalyst surface disrupting the ionic conductivity of the catalyst/ionomer network. To investigate the role of soluble metal ions, the Co_3O_4 and $Ni_{0.5}Co_{0.5}Fe_2O_4$ anode systems were operated in pure water and the anode effluent water was analyzed with inductively coupled plasma mass spectrometry (ICP-MS). The Fe, Ni, and Co concentrations measured for both systems were less than 5 ppb and no significant dissolution was observed (Figure B.14). It is likely the catalyst surfaces, particularly those with Ni and Fe, are dynamic at the local interface – dissolving to form voids and redepositing in unwanted locations – and that metal ions are not washed out into the system in the absence of soluble electrolyte to facilitate formation of stable dissolution products.

Conclusion

We have discovered critical catalyst processes that affect the performance and stability of AEMWE devices and are key for scalable H_2 production (summarized in Figure 3.7). The experiments indicate that conductive IrO_2 provides more active sites to oxidize ionomer, as opposed to mixed Ni/Fe/Co catalysts that show a lower extent of oxidation by XPS, likely due to much lower electrical conductivity. IrO_2 is sufficiently conductive, so any Ir sites in contact with the ionomer network are active, leading to rapid ionomer degradation throughout the catalyst layer. Co_3O_4, while less electrically conductive, appears conductive enough to maintain sufficient activity throughout the catalyst layer. Improved performance is likely possible by further improving the electrical properties. The OER on Co_3O_4 likely converts the particle surface to CoOOH, but the depth of conversion is sufficiently thin as to not disrupt the catalyst/ionomer interface. The ionomer still oxidatively degrades throughout the catalyst layer but at a slower rate than for IrO_2. XPS shows NiO converts to nominally NiOOH, and our evidence suggests that changes to ionomer/catalyst interface associated with this transition contribute to faster degradation. The low electronic conductivity of $NiCoO_2$, $Ni_{0.5}Co_{0.5}Fe_2O_4$, and $NiFe_2O_4$ confines OER to the region in direct contact with the stainless-steel GDL. As the ionomer oxidizes, ionic conductivity to this region decreases. Ionically accessible catalyst sites are now further from the GDL, but low electronic conductivity limits reactivity of these sites creating a resistive layer and cell voltage increases. This ionomer degradation would not necessarily be observed by XPS as it is a surface-sensitive technique, and the degradation does not extend into the bulk of the catalyst layer.

$NiCoO_2$ and $Ni_{0.5}Co_{0.5}Fe_2O_4$ show a Ni-rich surface after operation and $NiFe_2O_4$
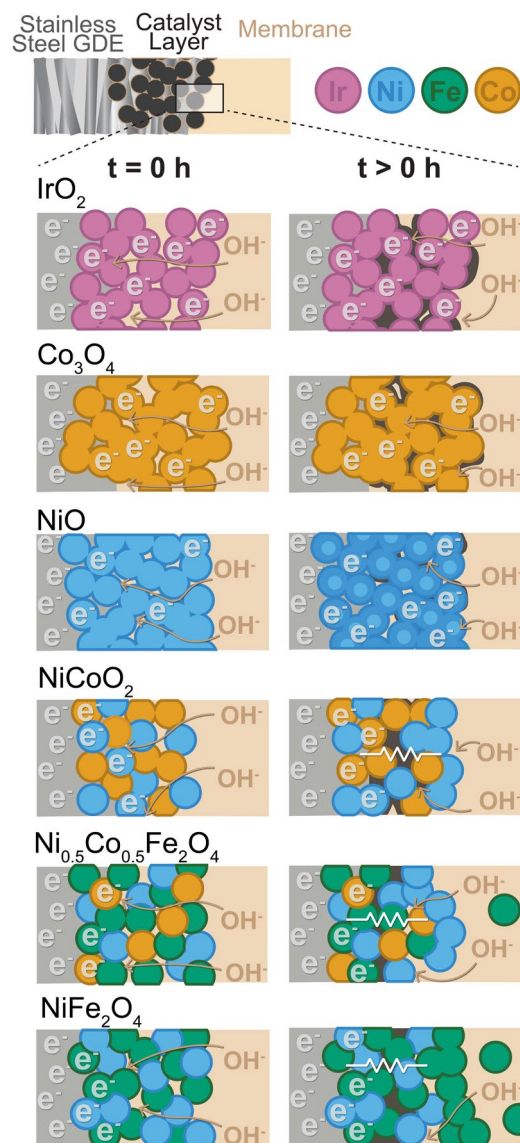
Figure 3.7. Summary of possible anode degradation processes. Left: the catalyst starting state; Right: after extended operation. Pristine ionomer is shown in tan; degraded ionomer regions are dark brown. IrO_2 (pink) degrades the ionomer throughout the catalyst layer but has sufficient electronic conductivity to still access ionically conductive regions. Co_3O_4 (gold) also degrades the ionomer but at a slower rate and has sufficient electrical conductivity to maintain some activity throughout the catalyst layer. NiO (light blue) converts to the electrically conductive NiOOH phase (dark blue), increasing electronic conductivity but disrupting the catalyst/ionomer interaction. $NiCoO2$ (blue and gold), $Ni_{0.5}Co_{0.5}Fe_2O_4$ (blue, gold, and green), and $NiFe_2O_4$ (blue and green) have low electronic conductivity. Ionomer degradation decreases ionic pathways to the catalyst creating a resistive zone. $NiCoO2$ and $Ni_{0.5}Co_{0.5}Fe_2O_4$ show a Nirich surface after operation and $NiFe_2O_4$shows an Fe-rich surface after operation, both likely due to dissolution/redeposition.

shows an Fe-rich surface after operation. Changes to the ionomer/catalyst interface associated with this rearrangement likely result in changes to surface contact and charge-transfer resistance. For $NiCoO_2$, as CoO_x is known to be stable during operation, [25-26] we hypothesize Ni ions are leaching/redepositing from the catalyst, possibly due to a lower local-pH environment created by the reduced OH^- conductivity to the region. The Fe-rich surface for $NiFe_2O_4$ is likely due to dominant Fe leaching/redeposition. For $Ni_{0.5}Co_{0.5}Fe_2O_4$ both Ni and Fe are likely leaching. Leached ions can create voids in the ionomer network disrupting the ionic connectivity and physical coupling between ionomer and catalysts. Ions that redeposit on the catalyst likely change ionomer/catalyst inter-actions, reducing ionic conductivity and/or blocking active sites. In solution, those ions may also accelerate existing, or introduce additional, ionomer degradation mechanisms. Multiple degradation modes are likely occurring simultaneously with the Ni–Fe oxides contributing to their rapid failure during device operation.

Understanding the behavior of non-PGM catalysts in industry relevant pure-water-fed AEMWE devices is critical to inform materials design for advanced electrolyzer technology. Here, we isolate anode catalyst processes from overall device performance and report the first chemical insight into catalyst characteristics and processes driving system degradation. Analyzing the performance and stability of five non-PGM anode catalysts in comparison with a baseline IrO_2 catalyst in a pure-water-fed AEMWE, we reveal that high electronic conductivity of the catalyst results in a better voltage performance but faster ionomer oxidation. We also discover a variety of degradation processes occurring for each catalyst. The main sources of degradation stem from catalyst restructuring and ionomer oxidation under OER-relevant conditions – the

structural stability of IrO_2 and Co_3O_4, coupled with good electrical conductivity and OER activity, are the reasons for their superior durability. We have thus begun to isolate ionomer degradation from catalyst phenomena during operation in an MEA configuration and simultaneously provided fundamental insight into non-PGM catalyst operation in industry relevant configurations and conditions. Our approach also uses a simple, scalable GDL preparation method and commercially available catalyst to show Co_3O_4 is a viable option for developing non-PGM-based AEMWEs, which is important for AEMWEs to grow into a competitive future technology.

Experimental Methods

Catalyst Dispersions and GDL Coating: Pt black (high surface area, Fuel Cell Store) nanoparticles were used as the cathode catalyst for all trials. Co_3O_4 (99.5%, 30–50 nm), NiO (99.5%, 15–35 nm), $NiCoO_2$ (99.9%, 20 nm), $NiFe_2O_4$ (99.99%, 20 nm), $Ni_{0.5}Co_{0.5}Fe_2O_4$ (99.995%, 40 nm) (US Research Nanomaterials), and IrO_2 (core/shell Ir/IrOx, Fuel Cell Store) nanoparticles were used at the anode. Cathode and anode electrodes were prepared identically by spray-coating using a published method.[1] Catalyst inks were prepared by mixing the catalyst powder (100 mg), water (0.5 g), isopropyl alcohol (1.7 g), and 5 wt% TP-85 (Versogen) ionomer (200 mg). Catalyst inks were sonicated for 1 h to disperse before spray coating using an airbrush (Testors, Aztek A2203). Pt black was sprayed onto carbon paper (Toray 090, Fuel Cell Store) and anode catalysts were sprayed onto a woven stainless-steel mesh (25AL3, Bekaert). A catalyst loading between 2.2 and 2.7 mg cm^{-2} was determined by mass difference. A thin layer of ionomer (2–5 wt%) was then sprayed on top of the electrode.

This resulting percentage was the lowest mass/thinnest ionomer layer that could be applied with uniform thickness.

Membrane Conditioning: PAP-TP-85 membranes (40 μm, Versogen) were conditioned according to manufacturer instructions. The membranes were soaked in 0.5 m KOH for 24 h, replacing the solution with fresh KOH after 1 h. Membranes were stored in 0.5 m KOH when not in use.

MEA Assembly and Hardware Operation: GDLs were cut to 1 cm^2 and assembled in the electrolyzer according to published procedures.[1] A water tank filled with 18.2 MΩ cm provided water to the cathode and anode at 125 mL min^{-1}.[1] The anode water flow was recirculated in the system while the cathode water flow was degassed in a chemical hood then recirculated back into the water tank. The temperature of the water source was set to 60 °C. The temperature in the electrolyzer cell at this temperature equilibrated to 57 ± 1 °C and was monitored with a thermocouple inserted into the anode and cathode cell hardware plates. The temperature difference between anode and cathode was maintained to less than ± 1 °C.

Applied Current Testing Conditions: All electrochemical testing was conducted using a potentiostat (BioLogic VSP-300) equipped with a 10 A/5 V booster cable. All tests were conducted under chronopotentiometric conditions unless otherwise indicated. The MEA was conditioned by stepping the current from 100 mA cm^{-2} to 1 A cm^{-2} in 100 mA intervals, holding for 2 min at each step. Impedance spectra were then collected from 500 kHz to 200 mHz at 50 mA cm^{-2}. Then, the cell was held at 1 V to observe the steady-state electrolysis current decay to zero, confirming there were no pinholes or shunt pathways present. The cell was brought back to 1 A cm^{-2} for 2 min to stabilize. The

potential was then recorded, and the current was decreased in 100 mA cm^{-2} steps until

reaching 100 mA cm^{-2}, further decreased to 50 mA cm^{-2}, and lastly 10 mA

cm^{-2}, measuring the potential for 10 s at each step to collect the J–V curve. The cell was

held at 500 mA cm^{-2} for stability measurements. During 20 h stability testing, impedance

data, as described above, were collected after 1, 3, 8, and 20 h. For any testing longer

than 20 h, impedance was collected only at the start and end of durability testing. After

analysis, the cells were disassembled, and the ionomer and membrane were converted to

the Cl$^-$ counter anion form by submerging the MEA in 3 m NaCl solution for at least 30

min (to prevent OH$^-$ attack induced by drying the ionomer). The materials were then

rinsed thoroughly with 18.2 MΩ cm water for 30 s and dried in air.

Applied Voltage Testing Conditions: To test the performance of NiFe$_2$O$_4$ at a lower

voltage, the cell was tested under galvanostatic conditions. For this, the MEA was

conditioned by stepping the voltage from 1.7 to 1.9 V in 50 mV steps. Impedance spectra

were collected over the same frequency range at 1.6 V. The cell was then stepped down

from 1.9 to 1.6 V in 50 mV steps held at 10 s to record the J–V curve. Durability testing

was conducted at 1.8 V. Impedance data of the same conditions were collected at the

same time points as the chronopotentiometric testing for consistency. The MEA was

disassembled and converted to Cl$^-$ counter ion as described above.

Fe Spike Test: An MEA with a Co$_3$O$_4$ anode was prepared and conditioned

according to the above procedure, but water was flowed to the anode and cathode with

separate water pumps. Each was flowed at 75 mL min^{-1}, which was the highest flow rate

possible before high back pressure caused the water line to detach from the pump.

Durability testing was operated at 500 mA cm^{-2}. When the degradation rate stabilized to

below 1 mV h–1, the inlet line for the anode pump was moved to a 1 ppm Fe^{3+} solution composed of 0.19×10^{-3} M $Fe(NO_3)_3 \cdot 9H_2O$ (ACS reagent grade ≥98%, Sigma). The solution was held at the same temperature as the water tank to maintain a constant hardware temperature. Current was held at 500 mA cm^{-2} during this time and durability testing was continued for an additional 28 h. The MEA was disassembled and converted to Cl^- counter ion as described above.

Catalyst Conductivity Measurements: The catalyst powders (~200 mg) were pressed between two stainless steel disks inset in a plastic holder (Figure B.7). An aluminum bar was placed above and below the disks to make electric contact, which were connected to a potentiostat using copper wire. Plastic sheets were placed above and below the aluminum to prevent short-circuit through the metal press. The powders were compressed to 23000 psi. The thickness of the powder was determined by measuring the distance between the top and bottom of the steel disks using a digital micrometer and subtracting the thickness of the disks with no catalyst powder. Polarization curves were collected from −1 to 1 V at 1 V s^{-1} (Figure B.8). The contact resistance was measured by the same method with no catalyst between the two disks. For the blank and IrO_2 measurements, the range was adjusted to −0.02 to 0.02 V at 10 mV s^{-1} to prevent current overload (Figure B.9). The measurement for IrO_2 matched that of the contact resistance, and thus a value was not reported for this catalyst. For all other catalysts, the resistance was obtained from a linear fit of the obtained current–voltage curve. The lead resistance was subtracted before calculating conductivity according to $\sigma = l/(RA)$, where σ is electrical conductivity in S cm^{-1}, l is the thickness of the catalyst powder in cm, R is the measured resistance in Ω, and A is the disk surface area in cm^2.

Catalyst Surface Area Measurements: N_2 adsorption/desorption isotherms were measured using a Micromeritics ASAP 2020 surface area analyzer at 77 K. Specific surface areas (S_{BET}) of the samples were calculated using the Brunauer–Emmett–Teller (BET) method, and pore widths and pore volumes (V_p) were calculated using the Barrett–Joyner–Halenda adsorption curves. Samples were suspended in isopropyl alcohol and dried at room temperature under vacuum for 12 h. Samples were then activated at 393 K (Co_3O_4, $NiCoO_2$, $Ni_{0.5}Co_{0.5}Fe_2O_4$, $NiFe_2O_4$, and IrO_2) or 423 K (NiO) for at least 24 h to remove the solvent and trapped gas. Activation was considered complete when the outgassing rate fell below 2.5 µtorr min^{-1}. The sample mass was calculated by the difference in mass between the empty sample tube and the loaded sample tube post-activation. The sample tube was massed before and after analysis to ensure the sample mass was unchanged during analysis.

Testing on Quartz-Crystal-Microbalance (QCM) Electrodes in KOH: The catalyst inks were prepared identically as for device testing and were spin-coated onto 5 MHz Au/Ti quartz crystals (Fil-Tech) at 3000 rpm and dried at 80 °C to obtain the loading of ≈ 22 µg$_{MO}$ cm^{-2} (normalized to exclude the mass of the ionomer). The cyclic voltammetry (CV) plots were collected using a potentiostat (BioLogic, SP-200) in 1.0 m KOH with the working electrodes connected to the QCM controller (Stanford Research Systems QCM200). Potentials in three-electrode modes were measured versus a 1 M KOH Hg/HgO reference electrode (CH Instruments). The reference electrode was calibrated before the electrochemical measurements using a reversible hydrogen electrode (HydroFlex).

During the three-electrode QCM experiments, the electrolytes were either bubbled with high-purity N_2 (Figure 3.1d) or conducted in open air (Figure B.6). All three-electrode electrochemical data were corrected for uncompensated series resistance (R_u), which was determined by equating R_u to the minimum total impedance in the frequency regime between 10 and 50 kHz, where the capacitive and inductive impedances are negligible, and the phase angle was near zero.

XPS Analysis of Pristine and Post-Mortem GDLs: XPS measurements were performed on an ESCALAB 250 (ThermoScientific) using Al Kα monochromated (20 eV pass energy, 500 µm spot size) and non-monochromated Mg Kα (400 W, 75 eV pass energy) flood sources. The use of the Mg source is critical in discerning Fe in the samples as typical Al sources exhibit overlap of the Fe 2p peaks with Ni and Co Auger LMM features. The samples were charge-neutralized via an in-lens electron source. Spectra were analyzed with ThermoScientific Avantage 5.99 software. The binding energies were calibrated to the C 1s signal at 284.8 eV.

The catalyst powders that do not contain Fe were analyzed as sprayed inks on stainless-steel GDLs prior and after the AEMWE operation with the ionomer ion-exchanged to Cl^- form. To avoid signal contribution from the Fe-rich stainless-steel, the metal ratios in the Fe-containing catalysts were analyzed separately from GDLs. To obtain the metal ratios in pristine catalysts, the powders were analyzed on a piece of carbon tape. To assess the changes to the metal ratios after electrolysis, the GDLs were sonicated in ethanol to remove the catalyst layer. The loose powder was collected, dried, and analyzed on a piece of carbon tape. The C 1s, N 1s, and F 1s spectra for Fe-containing catalysts were obtained with the inks on GDLs similarly to the other catalysts.

CHAPTER IV

OXIDATIVE INSTABILITY OF IONOMERS IN HYDROXIDE-EXCHANGE-MEMBRANE ELECTROLYZERS

Grace A. Lindquist, Jamie C. Gaitor, Willow L. Thompson,

Valerie Brogden, Kevin J. T. Noonan, and Shannon W. Boettcher*

This chapter contains co-authored work submitted for publication in *Energy and Environmental Science* in 2023. Myself and Shannon W. Boettcher designed the study. I collected and analyzed all electrolyzer, SEM, and XPS data, with electrolyzer support from Willow L. Thompson and SEM support from Valerie Brogden. The PNB ionomer system was designed by Jamie C. Gaitor and Kevin J. T. Noonan, with synthesis and characterization conducted by Jamie C. Gaitor. The work was written, organized, and edited by myself with a section written by Jamie C. Gaitor and editorial assistance from Shannon W. Boettcher.

Introduction

Anion-exchange ionomers have historically limited the performance and durability of HEM electrolyzer devices. [1-6] Common cation-exchange ionomers are perfluorinated-sulfonic-acid-(PFSA)-type materials with high chemical stability. [7] Most anion-exchange ionomers are hydrocarbons (e.g. polybenzimidazoles, polyethers, polyphenylenes, etc.) which are more susceptible to chemical degradation by nucleophilic OH^- in the strong alkaline conditions. While substantial polymer development in the past

decade has improved electrolyte-free HEM electrolyzer performance, [8-14] further improvements are needed. Most efforts at improving the stability of HEM polymers have focused on alkaline chemical stability, including adding protecting groups near electrophilic sites, [15-17] partial fluorination, [18] and tuning side-chain length[19] or cation identity. [20-21] Ex-situ chemical stability, however, is not necessarily reflective of device conditions nor indicative of how a polymer will perform in a membrane-electrode assembly (MEA), in particular during operation with electrolyte-free (nominally pure) water feed. In the MEA, the polymer may degrade by other chemical and electrochemical means besides OH^- attack. At the anode the ionomer is held at a strongly oxidizing potential and exposed to possible oxidizing species/intermediates produced during the oxygen-evolution reaction (OER). The oxidative and radical stability of anion exchange polymers has been investigated to various extents, [22-26] but few studies are conducted under device-relevant operating configurations and conditions.

Here we report a comprehensive ionomer failure analysis of HEM electrolyzer MEAs operating with electrolyte-free water and uncover common oxidative processes that must be solved for commercialization. Using integrated reference electrodes and impedance analysis on the full MEA electrolyzer, post-mortem surface analysis, and cross-sectional electron-microscopy and chemical imaging, we find ionomer oxidation as a dominant degradation mechanism across all ionomer chemistries studied in locally alkaline conditions, even those with all sp^3 carbon and PFSAs. We further investigate the effect of various additives and alternative feed modes on the extent of oxidation, showing pure-water operation degrading > 0.5 mV/h over 100 h using an oxidatively stable anode-

catalyst layer. Lastly, we introduce catalyst-layer design strategies for next generation HEM electrolyzer devices.

Results and Discussion

Degradation of TP-85 anion exchange ionomer

HEM electrolyzers with an active area of 1 cm^2 were prepared and assembled as described in the methods section and elsewhere (Figure C.11a). [9, 27] IrO$_x$ on platinized Ti and Pt black on Toray carbon-paper were used as the anode and cathode porous-transport electrodes (PTEs) respectively. Both electrodes were prepared with PiperION-A5 ionomer dispersions and devices were assembled with a 40-um-thick PiperION TP-85 membrane. For this study, the membrane and cathode remained constant for all experiments and only the anode PTE, including anode ionomer, was varied.
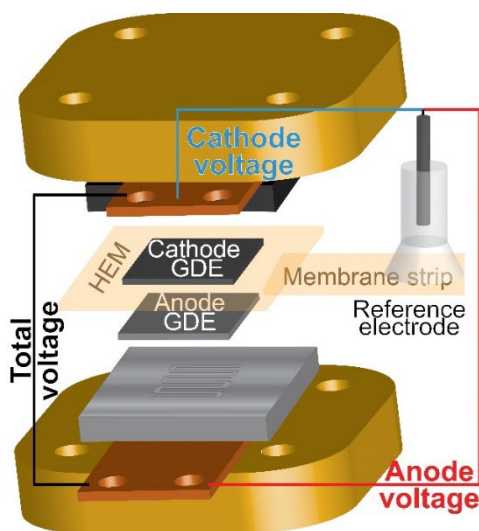
Figure 4.1. Schematic of the reference electrode integrated in the electrolyzer MEA and hardware. A reference electrode is placed on a strip of membrane attached to the HEM in the MEA. The voltage is measured from the cathode end plate or anode end plate versus the reference. Precision gasketing and a high conductivity HEM and reference strip are used to minimize mis-alignment reference-potential errors. [28-29]

Understanding electrolyzer device degradation during operation is challenging and usually limited to information gained from two-electrode studies. To better understand the contribution of individual components to the total cell voltage, a reference electrode was integrated into the MEA. [30] A strip of membrane is attached to the edge of the membrane in the MEA and extended outside the cell hardware, where a reference electrode is attached to the membrane strip and used to measure the anode and cathode components to the total cell voltage (Figure 4.1). A high conductivity HEM and reference strip are used to minimize reference electrode potential errors from non-symmetric current distributions. [28-29]

HEM electrolyzers were operated with electrolyte-free (nominally pure) water. The initial performance was 2.1 V at 1 A cm^{-2} (Figure 4.2a). The polarization curve is recorded following a ~20 min break-in period, during which some degradation may occur contributing to the high voltage performance relative to PEM benchmark systems. During operation at 1 A cm^{-2}, the total cell voltage decreases for a short period before rapidly degrading at 22 mV/h from 1 – 10 h then stabilizing to 4 mV/h from 10 – 20 h (Figure 4.2b). The reference electrode reveals this voltage degradation occurs at the anode. The cathode degradation was constant throughout the run at ~1 mV/h, which may be due to non-optimal water management that could be solved with better ionomer and cathode electrode design, but is not the focus of this work.

The Nyquist plot of the full cell shows two semi-circles (Figure 4.3c). During operation, the low frequency resistances of both semicircles increase with time. If these two processes were assumed to be the anode and cathode, this would suggest an increase

in both OER and HER charge-transfer resistance. However, the anode and cathode Nyquist plots using the reference electrode show two semicircles for the anode, and one at the cathode (Figure 4.2d). The second RC component at the anode may be due to a variety of processes, including ionomer oxidation reactions, a slow corrosion or dissolution mechanism, or water-dissociation reactions from OER occurring in lower pH regions in the catalyst layer. Impedance analysis of electrochemical devices is complicated[31] and more work is needed to assign mechanisms to each semicircle at the (degrading) anode. Previous measurements found OER faradaic efficiency of ~98 % for the same MEA system.[9] After operation at 1 A cm^{-2}, both charge-transfer resistances at the anode increased significantly while the cathode increased only slightly, consistent with the conclusion that cell degradation is an anodic process. Simulated Nyquist data using values obtained from the reference electrode measurements agree with the raw total-cell impedance collected without the integrated reference electrode (Figure C.13). When the operating current is lowered to 200 mA cm^{-2} the total-cell voltage-degradation rate decreases to 7 mV/h from 0 – 10 h, and 3 mV/h from 10 – 20 h (Figure 4.2b). This voltage degradation is at the anode; the average cathode degradation rate was 50 μV/h. Interestingly, at 200 mA cm^{-2} the initial large decrease in voltage was not observed. A decrease in voltage can still indicate cell degradation, for example membrane thinning which decreases cell resistance, and is not necessarily cell performance improving.[6] The ionomer loading in the PTE is 20 wt% relative to catalyst mass, which was chosen to ensure sufficient ionomer sample signal for XPS and resolution for SEM cross-section analysis (discussed later). A high ionomer loading can contribute additional iR or mass-transport losses to the cell voltage. This initial voltage decrease is not observed when the

ionomer content is decreased to 10 wt% (Figure C.14), and thus we interpret the initial

voltage decrease at 1 A cm^{-2} as various coupled catalyst layer reorganization and

degradation processes, which initially decreases catalyst-layer resistance and appears as

an improvement in cell voltage.

X-ray photoelectron spectroscopy (XPS) analysis of the PTE surface was

conducted to understand the anode-degradation mechanism (Figure 4.3). The pristine
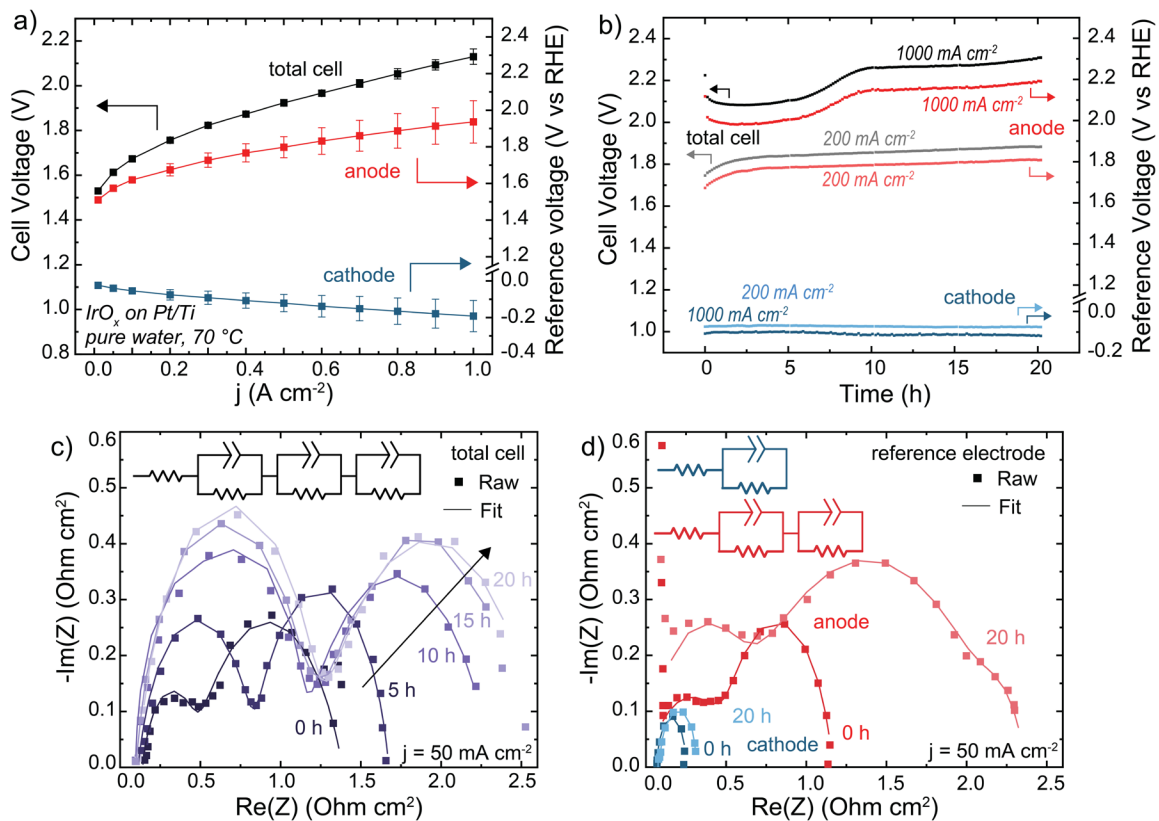
Figure 4.2. Performance and stability of a HEM electrolyzer. Cells were operated with an IrO$_x$/TP-85 catalyst layer on Pt/Ti anode, TP-85 membrane, and Pt-black/TP-85 cathode. a) Polarization curve showing anode and cathode contribution to total cell voltage. Reported data is the average of three polarization curves and the error bars are one standard deviation. b) Cell durability at 200 mA cm^{-2} (gray total cell, light red anode and light blue cathode) and 1 A cm^{-2} (black total cell, dark red anode and dark blue cathode). c) Nyquist plots of total cell impedance collected at 50 mA cm^{-2} as a function of time during the 1 A cm^{-2} test. d) Nyquist plots of the anode and cathode impedance measured at 50 mA cm^{-2} before and after 20 h operation at 1 A cm^{-2}. Nyquist plots were fit to the inset equivalent circuit. Degradation is primarily evident in the anode impedance.

anode PTE shows the expected spectra for the undamaged ionomer. No Ir XPS peak is observed (Figure C.15), as the PTE surface is sprayed with a top layer of ionomer and XPS only penetrates a few nm into the surface of the material. After operating at 1 A cm^{-2} for 20 h, the C 1s spectra from the cathode catalyst layer remains unchanged, while the anode C 1s spectra shows a new higher-binding-energy peak between 288 and 289 eV, consistent with carbonyl and/or ester group formation,[9, 23, 27, 32] and a loss of C-N content. This is accompanied by a loss of N 1s and F 1s peaks (Figure C.16), demonstrating both polymer backbone and cation groups have degraded and dissolved, at least from the surface layer analyzed. The surface of the anode PTE operated at 200 mA cm^{-2} for 20 h shows no obvious signal from ionomer oxidation, consistent with the more stable operating voltage and slower oxidation kinetics at lower anode potentials.
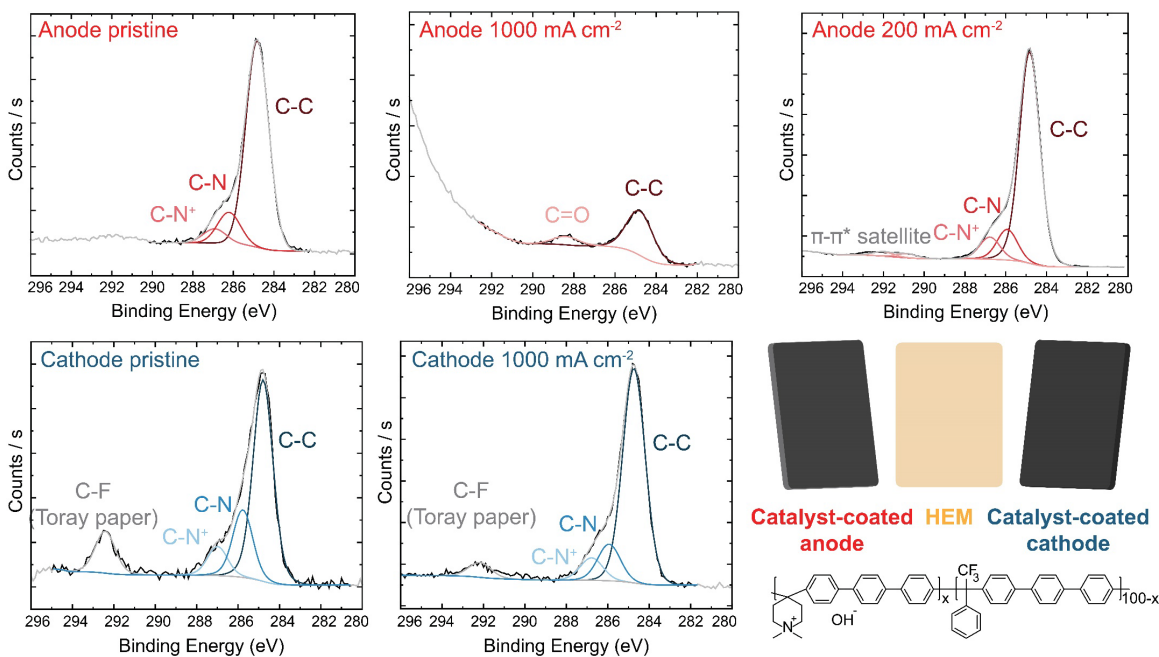
Figure 4.3. XPS analysis of IrO$_x$/TP-85 anode and Pt-black/TP-85 cathode. C 1s spectra of a) anode and b) cathode PTE. Inset shows the chemical structure of the TP-85 ionomer. Ionomer degradation is only observed on the anode PTE operating at high current.

We note that XPS signal from carbonate or bicarbonate may also appear in the binding-energy range where oxidized carbon species were found. All electrodes are quenched in 3 M NaCl before drying and thus any carbonate from operation should be exchanged to Cl⁻ before analysis. We have previously shown this procedure is sufficient to exchange carbonate to chloride after testing of ionomer films in supporting carbonate electrolyte. [23] To confirm this assumption here, an MEA was prepared, and pure water was flowed through the device at 70 °C without applied current. The PTE was ion exchanged and dried following the same procedure as the operated samples. XPS analysis shows only pristine polymer with no higher-binding-energy carbon peak (Figure C.17), indicating complete exchange of any absorbed carbonate. Therefore, growth of the high-binding-energy peak in the C region, combined with a loss of N and F signal, demonstrates severe ionomer oxidation in the anode catalyst layer. This oxidation is likely leading to reduced ionic transport to the catalyst, decreased electrochemical active area due to detachment of catalyst particles, and thus the increase in the anode charge-transfer resistance measured by impedance.

PTEs were then cross-sectioned using a plasma-focused-ion-beam (PFIB) and imaged with a SEM. The pristine PTE has ionomer uniformly dispersed throughout the catalyst layer (Figure 4.4a). After operation, no ionomer is observed, and only large aggregates of IrO_x remain (Figure 4.4b). The cross section of the control MEA with only water flow shows no ionomer degradation or loss from the catalyst layer (Figure C.18). The observed ionomer loss is thus a coupled chemical/electrochemical/mechanical process, and not purely detachment due to poor catalyst layer adhesion.

For HEM electrolyzers multiple degradation mitigation strategies have been pursued. These generally fall into three categories; improved ionomer design, introducing stable catalyst layer additives, and operation with supporting electrolyte – each of which is explored and discussed in the next section.
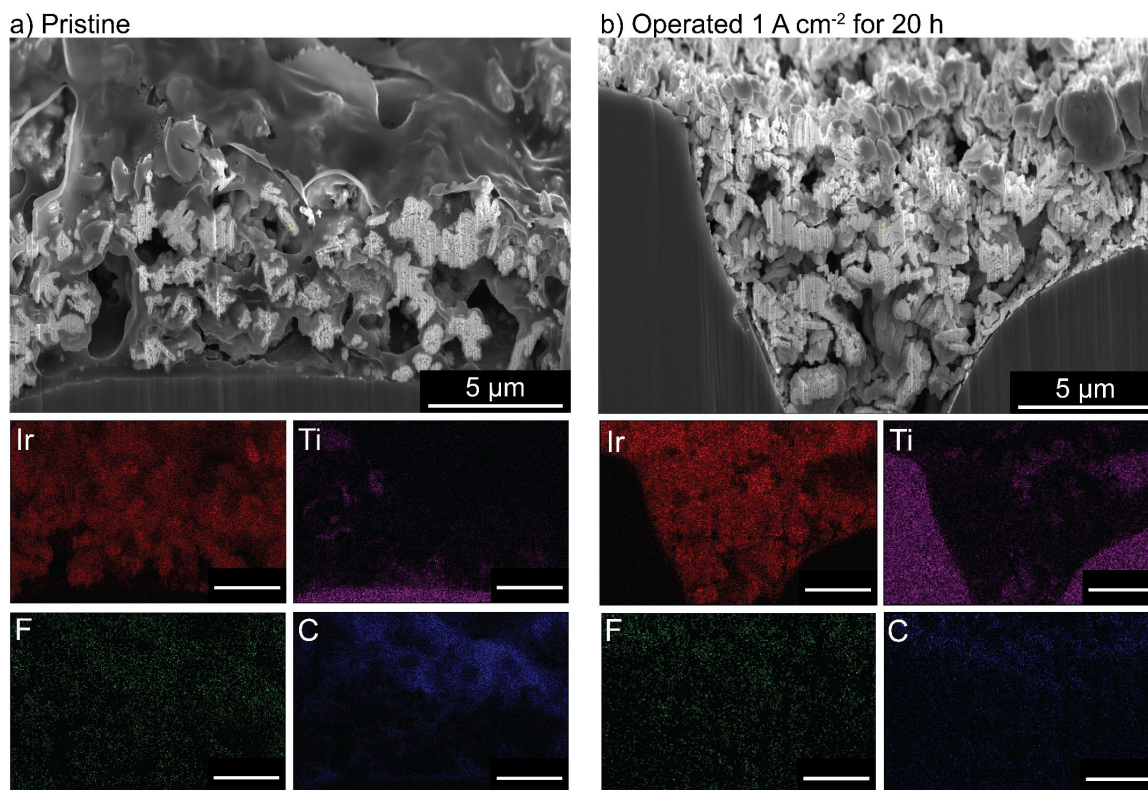
Figure 4.4. Cross-sectional imaging and EDX of an IrO$_x$/TP-85 anode PTE a) before and b) after 20 h operation at 1 A cm^{-2}. All scale bars are 5 μm. No ionomer is observed in the catalyst layer after operation.

All-sp^3 Norbornene-backbone ionomers

Many polymer design strategies have been pursued to improve alkaline ionomer durability. The polynorbornene (PNB) backbone is of particular interest. The aromatic regions of HEM backbones are likely weak sites for oxidation, [22-23, 26] therefore a fully sp^3-hybridized backbone should be more resistant to oxidative damage. These and related

polymers have shown promising performance and durability in HEM fuel cells[33-34] and electrolyzers. [35-37]

Anode PTEs were prepared using Co_3O_4 catalyst and the PNB ionomer on a woven stainless-steel substrate. MEAs were prepared with the same TP-85 membrane and Pt-black/TP-85 cathode PTE as previously. The PNB ionomers show nearly identical polarization performance as the equivalent TP-85 electrode (Figure 4.5a inset). When operating at 500 mA cm^{-2} the PNB ionomer appears more stable, with a more-linear voltage degradation as opposed to the rapid onset and stabilization behavior observed for the TP-85 (Figure 4.5a, light red and light orange). However, substantial oxidation is still observed by XPS in conjugation with a loss of ammonium cation and growth of uncharged nitrogen species (Figure 4.5b). At 1 A cm^{-2}, both electrodes show similar voltage degradation (Figure 4.5a, dark red and dark orange) and structural oxidation by XPS (Figure 4.5b). The extent of oxidation appears less compared to the IrO$_x$ OER catalysts, which we have found previously to be due to the lower electrical conductivity of Co_3O_4 that limits the reaction zone to near the PTL and thus less is observed on the top (opposite side) of the deconstructed post-mortem catalyst layer. [9] Different catalysts are also expected to differently interact chemically/electrostatically with ionomer which may lead to different adsorption and oxidation behavior. In any case, the results here show the PNB ionomer oxidation is comparable to the TP-85 under the same operating conditions, despite having all single bonds.

Other reports of PNB-based ionomers have shown stable voltage performance up to 1 A cm^{-2} during electrolyte-free water-electrolysis operation. [35-37] Other polymer characteristics can impact the extent of oxidation independent of polymer structure. Here,
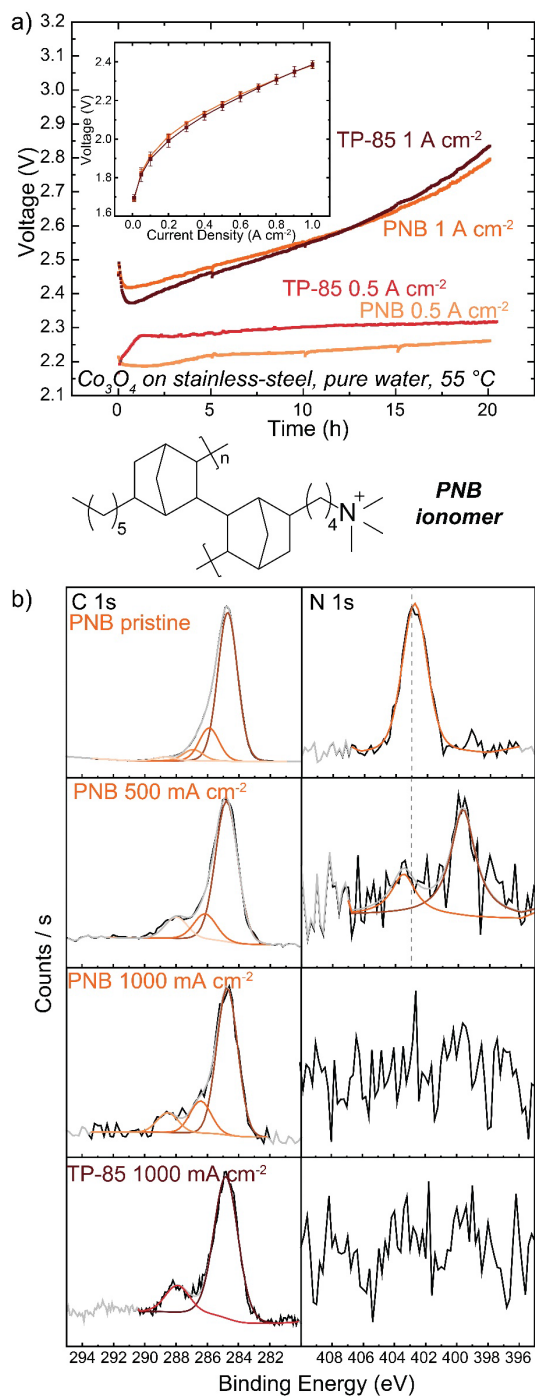
Figure 4.5. PNB ionomer performance and durability. Cells were operated with a Co₃O₄/PNB or Co₃O₄/TP-85 catalyst on stainless-steel anode, TP-85 membrane, and Pt-black/TP-85 cathode. a) Cell durability at 500 mA cm⁻² (light red TP-85 and light orange PNB) and 1 A cm⁻² (dark red TP-85 and dark orange PNB). Inset shows polarization performance (dark red TP-85 and dark orange PNB). b) XPS comparison of pristine and operated anode PTEs. Both systems show similar voltage degradation and anode ionomer oxidation, despite differences in ionomer chemistry.

the ion-exchange capacity of the ionomer was tuned to result in the same voltage polarization performance as the TP-85 system, but the two polymers possess different water uptake and OH⁻ conductivity properties (Table C.1). Ionomer water uptake can affect device stability, and a low water uptake material at the anode was shown to improve stability despite the performance losses from low ionic conductivity. [36] Water uptake will also affect how chemical OH⁻ and radical oxygen species access and interact with the ionomer, and thus ionomers with lower water uptake may not degrade as rapidly. The most-stable electrodes appear to be prepared with ground ionomer resin particles as opposed to the conventional dissolved/dispersed ionomer solution in ink as used here. Such electrodes often include PTFE additives. This observation presents an interesting question as to the effect of catalyst layer geometry and morphology on ionomer degradation and the role of non-ion-conducting additives as stabilizers in the catalyst layer.

Degradation in electrodes with stabilizing additives

Despite Nafion being a cation-conducting polymer, some HEM studies have pursued it as a binder to improve system lifetimes (because PEM electrolyzers show far superior stability). A Nafion anode PTE was prepared with IrO_x catalyst on platinized Ti and operated with a TP-85 membrane and Pt-black/TP-85 cathode PTE. The performance and durability were compared to a conventional PEM baseline with a Nafion membrane and Pt-black/Nafion cathode. The PEM electrolyzer reached 2 V at 2.5 A cm^{-2} (Figure 4.6a). The PEM cells were operated at 1 A cm^{-2} and 2.5 A cm^{-2} to compare equivalent current and voltage conditions to the performance of the TP-85 HEM and ionomer system. Both PEM systems showed degradation rates below 1 mV/h (Figure 4.6b). There
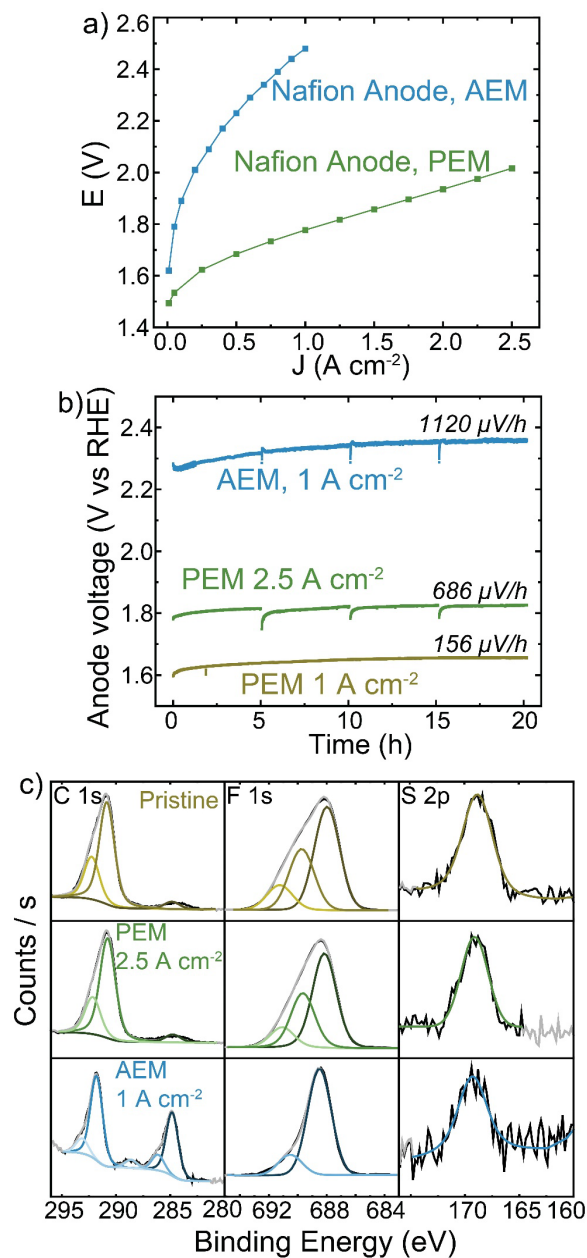
Figure 4.6. Nafion PTE operation in different membrane-pH environments. All cells were operated with a Nafion/IrO$_x$ catalyst on Pt/Ti anode, TP-85 or Nafion membrane, and Pt-black/TP-85 or Pt-black/Nafion cathode (matching the membrane). a) polarization comparison of Nafion PTE operating in a PEM MEA (green) and HEM MEA (blue). b) Nafion anode durability when operating in a PEM MEA at 1 A cm^{-2} (yellow) and 2.5 A cm^{-2} (green) and HEM MEA at 1 A cm^{-2} (blue). c) XPS of Nafion PTEs before operation (yellow), after operation with a PEM MEA at 2.5 A cm^{-2} (green) and after operation with a HEM MEA at 1 A cm^{-2} (blue). Degradation at the Nafion anode PTE is only observed when operating with a HEM.

was some initial voltage degradation, which is common for the startup of PEM systems as cell break-in/conditioning is longer, often many hours, during which ion transport channels are established. Further, most PEM electrolyzers use catalyst-coated membranes, while the PEM devices prepared here were catalyst-coated PTEs for direct comparison to the HEM electrolyzers. The initial degradation may be attributed to interfacial optimization between the catalyst layer and membrane. The degradation rate stabilizes to near-expected PEM rates. The degradation rate of the Nafion PTE operated with a HEM was an order of magnitude larger than that of the PEM at the equivalent operating current. XPS analysis of the surface of the PEM-operated Nafion anodes shows no obvious oxidation of the pristine material (Figure 4.6c, yellow and green). However, the surface of the HEM-operated Nafion shows the growth of C-C and oxidized carbon species, a decrease in the higher C-F contribution, and a loss of higher binding energy F, consistent with a loss of CF_3 content in the polymer. The sulfonate group is still resolvable, but with higher signal noise level than the PEM system. This suggests a side chain scission or loss mechanism, which is believed to be a dominant degradation pathway for Nafion polymer. [7, 38]

When operated with a HEM, the Nafion anode could create a bipolar interface between the anode and membrane, with proton transport through the anode and hydroxide transport from the cathode through the HEM recombining to form water at the anode/membrane interface. However, studies using mixed cation-ionomer/alkaline-membrane devices suggest the membrane pH environment will dictate the pH at the electrode/membrane interface more than ion transport in the ionomer of the catalyst layer. [39-40] The XPS degradation studies here support the existence of a high pH environment at

the catalyst layer/HEM interface. SEM cross-section analysis did not yield conclusive results regarding bulk catalyst-layer degradation, as the Nafion content was only 5% and no significant difference in ionomer environment is observed between the pristine Nafion PTE and the electrode operated with a HEM (Figure C.19).

Nafion is known to be stable across a wide pH range and as a membrane is chemically stable in many acid and alkaline electrochemical device applications. However, as a binder in a HEM catalyst layer it experiences high-surface-area contact with the strongly oxidizing anode catalyst and is exposed to a high concentration of radical oxygen species from intermediates. Combined with the high-pH environment, even Nafion suffers thus oxidative damage.

One mechanistic explanation for this broad instability is that the ionomer near the catalyst is polarized in the strong double-layer electric field, leading to increased susceptibility to nucleophilic attack by OH⁻, whereas in acidic systems no equivalent strong nucleophile exists. Alkaline oxidative environments are common in organic cleaning solutions used in semiconductor processing, for example RCA2. [41]

PTFE is also used as a non-conductive stabilizing additive. Anode electrodes were prepared with IrO_x catalyst on platinized Ti and either TP-85, PTFE, or a 50:50 wt% mixture of the two in the catalyst ink. The mass of total binder and ionomer relative to catalyst in the ink was kept constant for all electrodes. The reference electrode technique was used to determine changes to the cathode and anode as components of the total-cell voltage. Interestingly, the replacement of half the mass of ionomer with PTFE did not affect cell performance (Figure 4.7a). When only PTFE is present in the anode catalyst layer the voltage performance is very poor, as there is little-to-no ionic conductivity in the
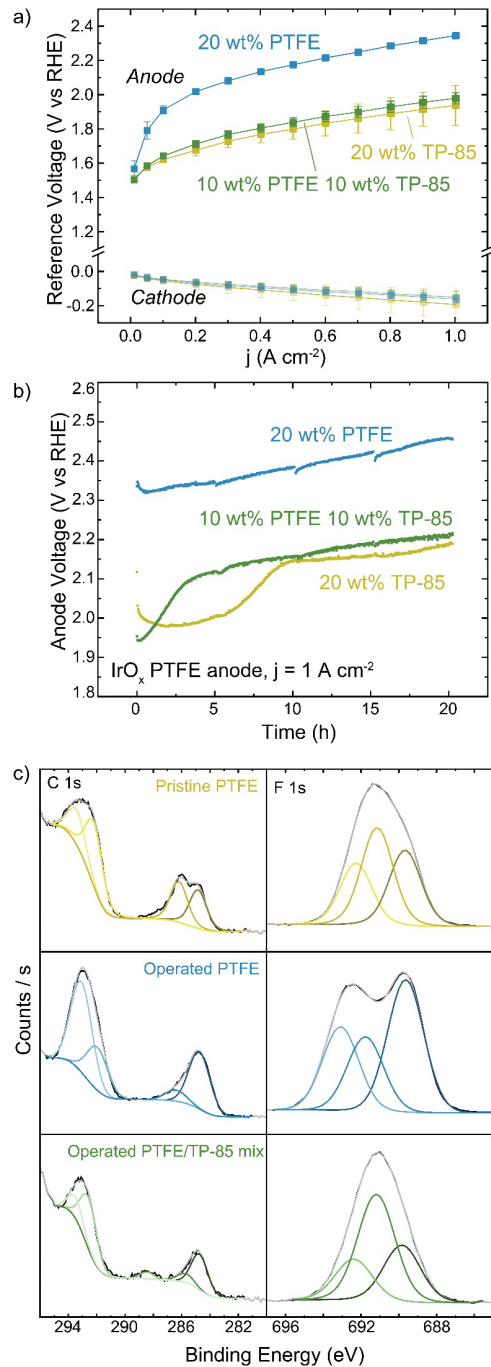
Figure 4.7. Effect of PTFE on electrolyzer performance. Cells were operated with an IrO$_x$ catalyst on Pt/Ti anode with the indicated ionomer and/or binder, TP-85 membrane, and Pt-black/TP-85 cathode. a) polarization curves of the anode and cathode potentials. Data shown is the average of three replicate measurements and error bars are one standard deviation. b) anode voltage during durability testing at 1 A cm^{-2} and c) XPS of the pristine PTFE anode (yellow), operated PTFE anode (blue), and operated mixed PTFE/TP-85 anode (green). No oxidation is observed for the PTFE-only system.

anode catalyst layer and thus only OER catalyst in direct contact with the HEM is active. The voltage-degradation profiles are quite different for the three electrodes (Figure 4.7b). Both electrodes containing TP-85 ionomer show a rapid degradation onset before stabilizing. The degradation profile of the electrode that contains a PTFE/TP-85 mixture matches that of the electrode operated with 10% TP-85 (the equivalent mass of just TP-85 in the electrode) and reaches a steady-state degradation rate of 5.4 mV/h for the last 10 h, comparable to the TP-85 system. The rapid degradation onset is not observed for the PTFE-only system. The steady-state degradation rate is 7 mV/h over the entire run.

XPS of the mixed-polymer PTE shows C-F contribution from the PTFE and oxidized carbon (Figure 4.7). XPS of the PTFE-only system shows no oxidized carbon by XPS (Figure 4.7c). Interestingly, the operated PTFE shows a change in F 1s region. This suggests a defluorination degradation mechanism, however, this is not consistent with the lack of changes in the C-F content in the C 1s region. The change in the F 1s region is thus attributed to a polymer/sample inhomogeneity or sample-charging artifact.

Cross-sectioning of the pristine mixed PTFE/TP-85 electrode shows the distribution of binder was not homogenous through the catalyst layer (Figure 4.8). The polymers are indistinguishable by EDX, as they only contain C and F content, but they show distinctly different texture/morphology. Some regions show the binder has a smooth texture, the same as what is observed for the TP-85-only catalyst layers and is thus assigned to the TP-85 ionomer (Figure 4.8b). Other regions show a porous binder environment (Figure 4.8a), which is assigned as PTFE binder. After operation, the mixed PTFE/TP-85 electrode shows regions of the porous-textured binder (Figure 4.8c) and

large catalyst aggregations with no binder (Figure 4.8d), which were likely regions where

TP-85 has degraded and been flushed from the system.
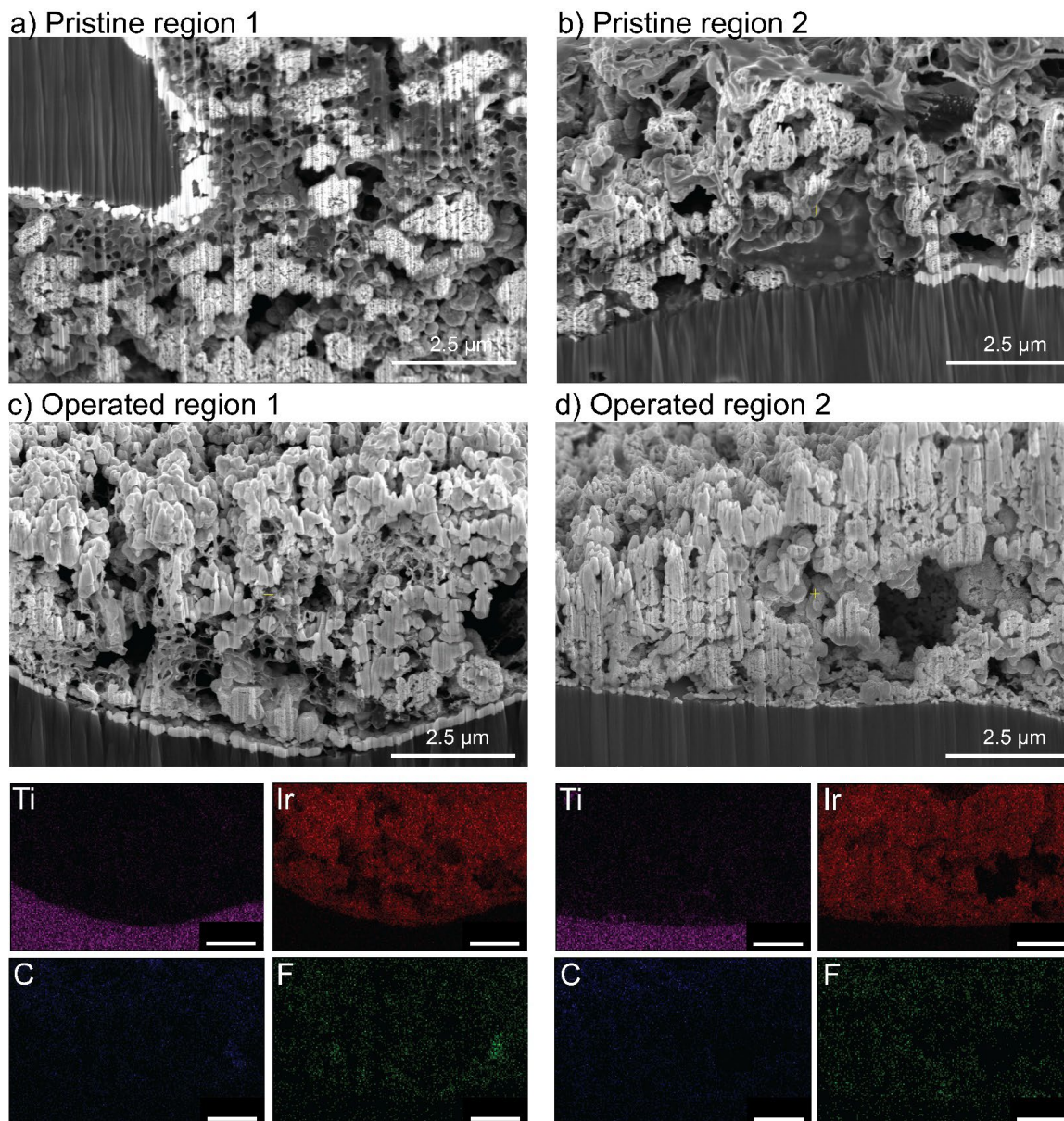
Figure 4.8. Cross-sectional analysis of IrO$_x$/mixed binder anode PTE. SEM images of different regions of the pristine catalyst layer (a and b) and SEM with EDX maps of two operated regions (c and d). Only PTFE binder is observed in the catalyst layer after operation.

Despite different degrees of oxidative damage, all systems show similar voltage degradation from 10 - 20 h. All three electrolyzers were operated with a TP-85 membrane that is susceptible to oxidation at the anode PTE surface. The similar steady-state degradation rate after 10 h may be due to catalyst oxidizing the membrane surface, increasing ionic resistance between membrane and catalyst layer. The PTFE-only system shows a slightly higher steady-state degradation rate, which is likely due to catalyst detachment or non-uniformities in the catalyst layer. PTFE contains no ionic components and does not interact strongly in the ink solution with the solvent or catalyst, creating a poor catalyst dispersion. The quality of the ink and catalyst layer deposited can impact device performance independent of the properties of the individual components. [27] Further, PTFE on its own is a poor catalyst binder, and the catalyst was observed to detach from the electrode during MEA preparation. SEM imaging shows the distribution of PTFE in the pristine catalyst layer was also non-uniform with large agglomerates of PTFE. The PTFE electrode charged too rapidly under the electron beam to obtain usable images. The PTFE catalyst layer after operation shows large areas of the bare exposed Ti support and no large PTFE agglomerates, suggesting some PTFE washed away during operation.

As PTFE is the only polymer to show no oxidative damage during pure-water operation in the current study, longer-duration testing was conducted. When operating with Co_3O_4 catalyst at 500 mA cm^{-2}, the cell operated for 100 h with a degradation rate of 0.3 mV/h (Figure 4.9a). No changes to polymer structure were observed by XPS after operation (Figure 4.9b). While cell voltage was high for commercial applications, advanced electrode designs that use stable binders or additives, but maintain ionic

conductivity in the catalyst layer, may be a viable solution for pure-water HEM operation.
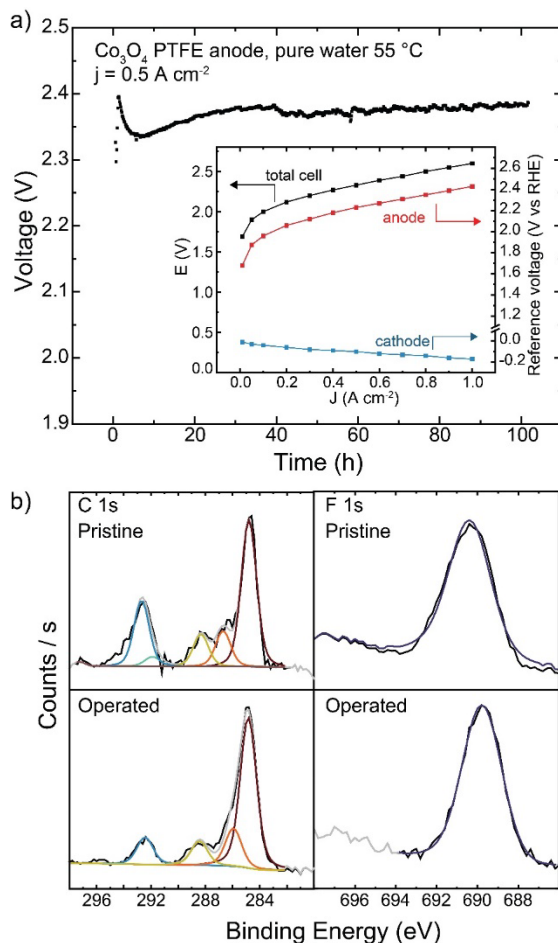
Figure 4.9. Long-term operation of a PTFE-containing anode. a) HEM electrolyzer operation with a Co_3O_4/PTFE-coated stainless-steel anode PTE, TP-85 membrane, and Pt-black TP-85 cathode for 100 h. Inset shows cathode and anode contributions to total cell voltage. b) XPS of the anode catalyst layer before and after 100 h operation.

Effect of supporting hydroxide electrolyte

  HEM electrolyzers have improved performance and stability when operating in KOH electrolyte. [35, 42] A Co_3O_4 TP-85 anode on a Ni-alloy substrate (to prevent corrosion in KOH on the PTE) was operated in 0.1 M KOH and also in electrolyte-free water (Figure 4.10). When fed with KOH, the catalyst layer is saturated with electrolyte and all

catalyst sites are exposed to OH⁻, as opposed to pure water where only catalyst sites in contact with the ionomer are active. The addition of electrolyte is expected to increase catalyst electrochemically active surface area, increase ionic conductivity of the catalyst layer, and decrease transport losses. This is reflected in the polarization data, as improvements in 0.1 M KOH are observed in the kinetic, ohmic, and mass-transport regions of the polarization curve (Figure 4.10a). The cells were then operated at 1 A cm^{-2} for 20 h (Figure 4.10b), and a smaller degradation rate < 1 mV/h was found, compared to the rapid degradation of the pure water cell at 17 mV/h. A third cell was then operated with 0.1 M KOH at 3 A cm^{-2} so the starting operating voltage was ~ 2 V where ionomer oxidation is known to occur in the electrolyte-free water system. The voltage was also more stable at a higher operating current, with a cell degradation of 2.4 mV/h. The anodes operated in 0.1 M KOH also show no obvious evidence of oxidized carbon, even after operating at voltages comparable to the electrolyte-free-water devices (Figure 4.10c). Only the electrolyte-free cell shows a growth of oxidized carbon in conjunction with a loss of N and F signal.

In electrolyte-free water, the weakest, most-easily oxidized polymer sites degrade first. This leads to an increase in cell voltage, which may induce a larger driving force at the remaining catalyst/ionomer interface for oxidation, driving cascading degradation until substantial ionomer is oxidized. In KOH, the degradation of ionically conductive polymer is compensated by the presence of supporting OH⁻. Local oxidation may lead to some catalyst detachment and loss of binder but does not appear to dramatically increase cell voltage and therefore does not increase the driving potential for oxidation.
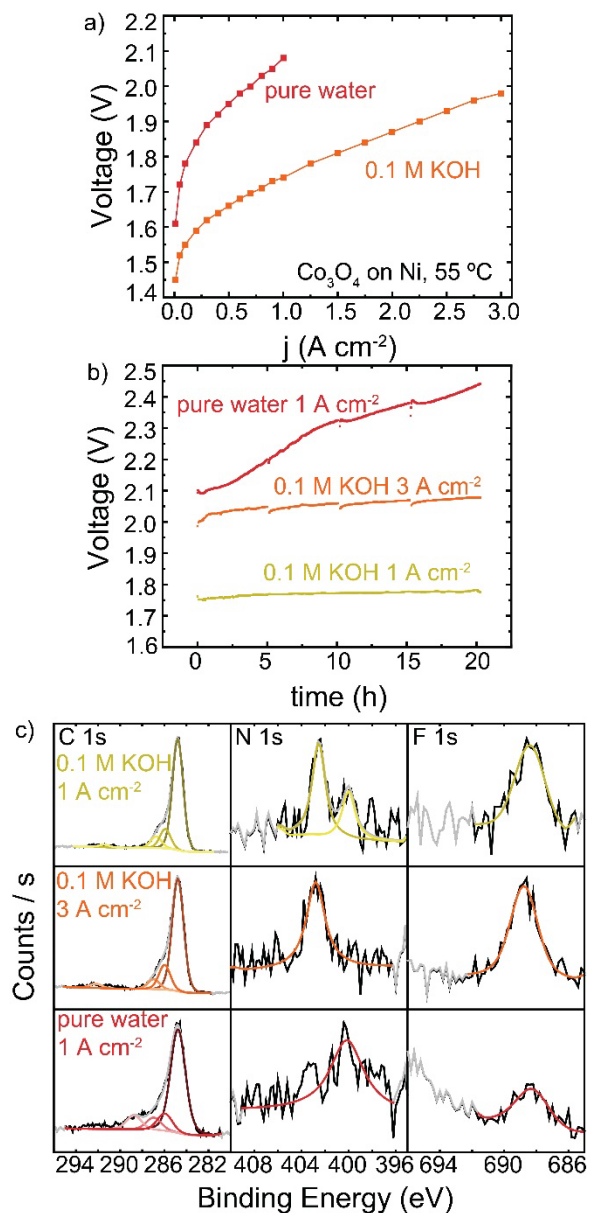
Figure 4.10. HEM electrolyzer operation in 0.1 M KOH versus pure-water feed. All cells were operated with a Co_3O_4/TP-85-coated Ni PTE, TP-85 membrane, and Pt-black/TP-85 cathode. a) polarization curves of electrolyte-free water (red), and 0.1 M KOH (orange) water feed, b) durability of electrolyte-free water (red) and 0.1 M KOH (yellow) feed at 1 A cm^{-2} and 0.1 M KOH 0.1 M KOH at 3 A cm^{-2} (orange; for operation at a comparable starting voltage to the electrolyte-free water system). Even under high voltages/currents, the presence of 0.1 M KOH dramatically suppresses oxidation, perhaps due to differences in double-layer structure.

The potential distribution and structure of the electrical double layer at the

catalyst surface may be quite different in electrolyte-free water versus in supporting

electrolyte. In alkaline conditions, metal-oxide surfaces are likely negatively charged (due to deprotonation) leading to absorption of cationic or polymer backbone groups from the ionomer, as has been invoked earlier for other reasons. [17, 20, 43-48] Without supporting electrolytes, ionomer therefore must play a fundamental role in the formation of the double layer requiring it to be in close vicinity to the polarized catalyst. The presence of mobile, soluble ions in supporting electrolyte likely leads to displacement of ionomer from direct involvement in the double layer, and this may be responsible for substantially reducing the degradation rate compared to pure water. Alternative strategies to exclude ionomer from the double-layer region therefore might be expected to also reduce oxidation rates.

While these results show operation in supporting electrolyte suppresses ionomer oxidation improving cell stability, the durability testing here was relatively short. The ionomer and membrane may continue degrading at longer operating time, particularly over months or years, leading to slow catalyst detachment or membrane thinning as is observed on a shorter time-scales in the pure water tests.

Conclusion

We compared HEM electrolyzer operation with chemically varied ionomers, catalyst layer additives, and feed modes to understand the extent of ionomer oxidation and its impact on cell performance. Anode ionomer oxidation is the dominant degradation mechanism for all HEM-based devices operating in nominally pure water. All hydrocarbon-based anion-exchange ionomers oxidize rapidly, losing both backbone and cationic side-chain groups. Nafion oxidizes in a HEM electrolyzer but not PEM

electrolyzer, indicating the high rate of degradation can be in part attributed to the combination of the strongly oxidizing environment and high pH. No oxidative damage was observed when using PTFE, showing the promise of stable additives in improving HEM electrolyzer operation.

This work illustrates the significant challenge facing pure-water HEM electrolysis, as no organic ion-conducting material was found to be stable under electrolyte-free operating conditions. While PTFE showed stable operation, the high ion-transport resistance in the catalyst layer results in low voltage efficiencies and is therefore not a promising route to commercialization on its own. For nominally-pure-water operation, next-generation HEM cells must look beyond solely ionomer innovations to advanced catalyst layers. Improved catalyst-layer interfacial design should minimize ionomer contact, and therefore degradation, but maintain OH$^-$ conductivity. These could enable competitive performance and lifetimes for commercialized pure-water HEM electrolyzer devices at dramatically lower materials costs than current membrane technologies.

Experimental Methods

Polynorbornene ionomer synthesis materials. All chemicals were purchased from commercially available sources and were used as received. Tri-tert-butylphosphine palladium (II) methyl chloride was synthesized with modifications to an existing literature procedure. [49] 5-hexylbicyclo[2.2.1]hept-2-ene (NB-5-Hex) and 5-(4-bromobutyl)bicyclo[2.2.1]hept-2-ene (NB-5-BuBr) were prepared according to prior work. [50] All polymerizations were performed in anhydrous, degassed CH$_2$Cl$_2$ under N$_2$.

Initiation of the Pd catalyst to form the active complex was accomplished using tetrakis(pentafluorophenyl)boron lithium ethyl etherate.

NMR Analysis. All NMR spectra were recorded on a 500 MHz Bruker Avance 3 Spectrometer or a 500 MHz Bruker Neo Spectrometer with Prodigy Cryoprobe. The ^{1}H NMR spectra were referenced to residual $CHCl_3$ (7.26 ppm).

Gel-Permeation Chromatography (GPC). Measurements were performed on a Waters Instrument equipped with a 2690 autosampler, a Waters 2414 refractive index (RI) detector, and two SDV columns (Porosity 1000 and 100000 Å; Polymer Standard Services). The eluent tetrahydrofuran (THF) was doped with 10 mM lithium bis(trifluoromethanesulfonyl)imide (flow rate of 1 mL/min, 40 °C). A nine-point calibration based on polystyrene standards (Polystyrene, ReadyCal Kit, Polymer Standard Services) was applied for determination of molecular weight.
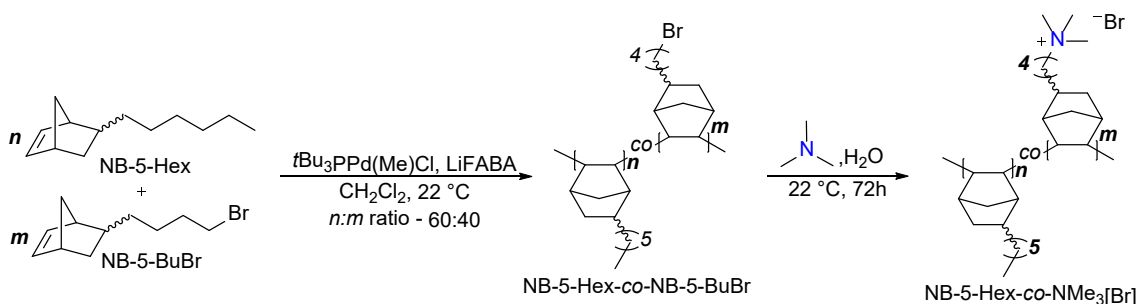
Scheme 4.1. General synthesis of 60:40 NB-5-Hex-co-NMe$_3$ HEM.

Statistical copolymerization procedure for 60:40 NB-5-Hex-co-NB-5-BuBr copolymer. In a N$_2$ glovebox, tetrakis(pentafluorophenyl)boron lithium ethyl etherate (0.0264 mmol), tri-tert-butylphosphine palladium (II) methyl chloride (0.0264 mmol), and dry CH_2Cl_2 (6.6 mL) were added to an oven-dried Schlenk flask equipped with a stir bar. 5-n-hexyl-2-norbornene (7.92 mmol) and 5-(4-bromobutyl)-2-norbornene (5.28

mmol) were added to a separate vessel and dissolved in dry CH_2Cl_2 (59.1 mL). Both solutions were brought to a benchtop stir plate, and the Pd catalyst reaction mixture was stirred for 15 min at 22 °C to ensure formation of the active cationic Pd catalyst. The solution of 5-*n*-hexyl-2-norbornene and 5-(4-bromobutyl)-2-norbornene in CH_2Cl_2 was then injected into the activated catalyst solution. The polymerization reaction was stirred, and a 0.05 mL aliquot was removed at various timepoints for crude analysis by ^1H NMR spectroscopy to ensure complete consumption of the two monomers (disappearance of the vinyl protons). Polymers were precipitated into a large excess of methanol, which yielded an off-white stringy polymer that was filtered and dried *in vacuo* for 17 h at 22 °C (2.51 g, 96% yield). ^1H NMR (500 MHz, $CDCl_3$) δ ppm: 3.4 (br s, 2H), 2.6 – 0.96 (br, all other protons except for hexyl norbornene $-CH_3$), 0.88 (br s, 4.5 H) (Figure C.2).

Functional group incorporation. Incorporation of NB-5-BuBr in the NB-5-Hex-co-NB-5-BuBr copolymers was determined as in our prior report. [50] The ratios of the -CH_2Br signal from the bromobutyl chain and the -CH_3 signal from the hexyl chain were compared to determine the relative ratio of the two monomers. The integration for the methylene signal was set to two (corresponding to one repeat unit of BrBuNB) and the value for the hexyl signal was divided by three to determine the relative ratio of hNB units. A sample calculation is shown in Figure C.2. In the ^1H NMR spectrum for the 60:40 copolymer, a 2:4.5 ratio should be observed for the -CH_2Br signal on the NB-5-BuBr the terminal methyl group from the hexyl chain of the NB-5-Hex, so the reported assignments for the terminal methyl group are set to 4.5.

Solution casting of 60:40 NB-5-Hex-co-NB-5-BuBr copolymers. 150 mg of polymer was dissolved in 3 mL of $CHCl_3$. Upon complete dissolution, the solution was

filtered through a 0.22 μm syringe filter onto a stainless-steel dish (diameter – 5 cm). The CHCl$_3$ evaporated over an hour to afford a clear freestanding film, which was removed from the dish by immersion in deionized water. The polymer was then dried *in vacuo* to remove water and any other residual solvents.

Synthesis of 60:40 NB-5-Hex-co-NMe$_3$ Polymer. The dried NB-5-Hex-co-NB-5-BuBr polymer film was immersed in an aqueous solution of 25% (w/v) trimethylamine for 48 h at room temperature. The solution was then replaced with fresh aqueous trimethylamine and the films were immersed for an additional 24 h. The films were removed and immersed in 3 × 100 mL portions of deionized water for 1 h each. The films were then dried *in vacuo* to afford the trimethylammonium-functionalized polymers. Accurate ^{1}H integrals were difficult to obtain due to overlapping solvent and signal broadness. Spectral data: ^{1}H NMR (CDCl$_3$:CD$_3$OD 1:1) δ ppm: 3.0 (br s, 9H, NMe$_3$ -CH$_3$), 2.5 – 0.76 (br, all other protons except for hexyl norbornene -CH$_3$), 0.56 (br s, 6H) (Figure C.2).

Catalyst Dispersions. Materials were prepared as previously reported.[9, 27] Pt-black (high surface area, Fuel Cell Store) was used as the cathode catalyst for all studies. IrO$_x$ (core-shell Ir/IrO$_x$, Fuel Cell Store) or Co$_3$O$_4$ (99.5%, 30-50nm, US Nano) nanoparticles were used as the anode catalyst. For HEM devices, cathode and anode ink solutions were prepared identically. For every 100 mg of catalyst, 0.5 g of 18.2 MΩ cm H$_2$O was added, followed by 1.7 g of 2-propanol. The PiperION-A5 ionomer suspension (TP-85, 5% w/w, Versogen) was added (200 mg) to yield the final 10 wt. % ($w_{ionomer}/w_{catalyst}$) ink. For PEM studies, inks were prepared similarly but with 100 mg of D520 Nafion dispersion (alcohol-based 1000 EW at 5 wt%, Fuel Cell Store) as the

ionomer to yield the final 5 wt. % ($w_{ionomer}/w_{catalyst}$) ink. Inks were then bath-sonicated

(Branson 1510R-MTH) with 5 °C water recirculating to maintain a room temperature

bath. Inks were sonicated for a minimum of 1 h (Pt and Co_3O_4) or 2 h (IrO_x) until fully

dispersed.

Electrode Preparation. Toray carbon paper (090, Fuel Cell Store) was used as the

cathode electrode material for all studies. The anode was either a stainless-steel mesh

filter material (25AL3, Bekaert), platinized Ti (Nel Hydrogen), or Ni-alloy (Hastelloy X,

UNS 06002, Technetics Inc.). In all cases the support was taped to a hot plate set to 80 °C

and catalyst inks were air-brush coated onto the substrate (Testors, Aztek A2203, part of

the Amazing Airbrush kit). A catalyst loading between 3 and 3.5 mg cm^{-2} was used to

ensure a sufficiently thick catalyst layer for cross-sectional analysis. Loading was

determined by mass difference. A thin layer (~5 wt. % $w_{ionomer}/w_{catalyst}$) of ionomer

suspension was sprayed on top of the catalyst layer.

Membrane Conditioning. PiperION TP-85 (40 μm, Versogen) membranes were

conditioned according to manufacturer instructions. The membranes were soaked in 0.5

M KOH for 48 h, replacing the solution with fresh KOH after 24 h. Membranes were

stored in 0.5 M KOH solution when not in use. For PEM experiments, Nafion (212, Fuel

Cell Store) was hydrated in 18.2 MΩ cm water and stored in water when not in use.

MEA Assembly. MEAs were assembled in an adapted PEM fuel-cell hardware

(Fuel Cell Technologies, 5 cm^2 hardware) with stainless-steel (pure water feed) or Ni

(KOH feed) anode flow fields and a graphite cathode flow field. Gasket material (0.005"

and 0.002" PET/PETE clear film, McMaster-Carr) was laser cut to an active area of 1

cm^2. Sintered platinized Ti frits (Baoji Yinggao Metal Materials Co., Ltd.) were used as

spacers between the flow fields and PTEs to maintain uniform compression across the MEA (Figure C.9a). The conditioned membrane was submerged in a beaker of 18.2 MΩ cm water then rinsed with 18.2 MΩ cm water for 10 s before assembly. Materials were assembled in the stack and tightened to 5.6 Nm.

Assembly With an Integrated Reference Electrode. For some experiments, the cells were operated with an integrated reference electrode. Cells with an integrated reference electrode were constructed as previously reported.[30] An extended description of the reference-electrode technique is included in the supporting information (Figure C.3-12). Upon assembly, a strip of membrane is laid next to the anode porous transport electrode (PTE) and extended outside the cell hardware. The HEM is laid on top of the PTE and overlaps with the strip. The cathode PTE is placed on top, and the cell is assembled as usual. After assembly, a O-ring joint to straight-glass adapter is clamped to the membrane strip and filled with 0.1 M KOH (Figure C.12). A reference electrode (Hg/HgO, CH Instruments Inc.) is inserted in solution and the glassware is sealed with parafilm. The strip is kept hydrated with an intravenous bag dripping 18.2 MΩ cm water on the strip every 7 min (Figure C.12).

Electrolyzer Operation. A water supply reservoir was filled with 18.2 MΩ cm water. This water is nominally pure (but not necessarily 18.2 MΩ cm), and is referred to as "electrolyte-free" water feed in this context. Water was flowed to either the anode or both cathode and anode at 125 mL min^{-1}. The anode water flow was recirculated in the system, while the cathode water was flowed into a chemical hood, degassed in a plastic jug, then recirculated back into the water tank. Cell temperature was monitored with a thermocouple inserted into the cell hardware. Cells were conditioned by stepping the

current from 100 mA cm^2 to 1 A cm^{-2}, holding for 60 s at each step up to 700 mA cm^{-2}, then 90 s from 800 mA cm^{-2} to 1 A cm^{-2}. The cell was then held at 1 V to test for pinholes or other short-circuit pathways in the cell (the steady sate electrolysis current decays to zero at < 1.23 V, while shunt currents persist). When operating with KOH this step was bypassed, as ions can be transported across the membrane below 1.23 V when operating with supporting electrolyte. The cell was brought back to 1 A cm^{-2} for 2 min to stabilize. The potential was then recorded, and the current was decreased in 100 mA cm^{-2} steps measuring the potential for 10 s at each step to collect the polarization (*J-V*) curve. When operating with the reference electrode, water flow to the cathode was closed and the cell was held at 100 mA cm^{-2} for 1 min to accumulate H$_2$ on the Pt catalyst. The cell OCV was then measured for 1 min and the reference electrode voltage versus the cathode (now poised at RHE) was used to calibrate the reference voltage for each run. The cell was held at constant current for stability testing. Galvanostatic electrochemical impedance spectroscopy (GEIS) was collected at 50 mA cm^{-2} and 500 mA cm^{-2} after collecting the *J-V* curve every 5 h of the stability run.

Post-Operation Sample Preservation. After operation, cells were disassembled according to standard methods. [51] MEAs were quenched in 3 M NaCl solution overnight to exchange OH$^-$ for Cl$^-$ ions. The MEA components were then submerged in a beaker of 18.2 MΩ cm water and rinsed vigorously for 30 s before air drying at room temperature overnight.

XPS Analysis. Catalyst layers were analyzed with X-ray photoelectron spectroscopy (XPS) on an ESCALAB 250 (ThermoScientific) using an Al Kα monochromated (20 eV pass energy, 500 μm spot size) source. The samples were charge-

neutralized using an in-lens electron source. The stage was electrically floated to reduce sample charging. Spectra were analyzed using ThermoScientific Avantage 4.88 software. The C 1s signal at 284.8 eV was used to calibrate the binding energy scale.

SEM Cross-Sectioning and Imaging. PTEs were cross-sectioned and imaged using a plasma focused-ion-beam (PFIB) scanning-electron microscope (SEM) (Helios Hydra Multi-Ion Species Plasma FIB, Thermo Fischer). The ion beam was operated at a 30 kV accelerating voltage. The beam was focused at 0.1 nA, as the current was sufficiently low to not damage the polymer in the catalyst layer. Current was then increased to 1 or 2.5 μA without imaging and a section of PTE was blind cut. The edge was then polished at 15 nA, again without active imaging to not damage the catalyst layer. Electron imaging and energy dispersive spectroscopy (EDS) was collected at a 10 kV accelerating voltage and 0.8 or 1.6 nA electron beam current.

CHAPTER V

CATALYST AND IONOMER SUMMARY AND OUTLOOK

Grace A. Lindquist and Shannon W. Boettcher

This chapter contains co-authored work accepted for publication in *Electrochemical Society Interface* in 2023. The work was written and organized by myself with editorial assistance from Shannon W. Boettcher.

Degradation of anion exchange polymers

For AEM electrolyzers and fuel cells, the stability-limiting component is the anion exchange polymer.[1] This polymer is used as a membrane and mixed in the catalyst layer to transport hydroxide to the high-surface-are catalyst and improve contact between the catalyst layer and membrane. Most polymer development has focused on improving polymer alkaline stability and prevention of OH^{-} nucleophilic attack.[2-3] The oxygen electrode in fuel cells, however, operates at much less-oxidizing potential than in electrolyzers, meaning the ionomers in electrolyzers must have much better oxidative stability. Polymer degradation experiments also often use model *ex-situ* studies, such as soaking materials in KOH solution or three-electrode studies mimicking oxidative environments.[3-4]

When operating in an AEM electrolyzer with pure-water feed we find the ionomer in the anode catalyst layer sees substantial oxidative damage. When testing different anion exchange polymers, we observe a similar degradation rate for the initial ~20 h of

operation, nearly independent of polymer chemistry across a wide range of materials. [5] XPS shows an increase in oxidized carbon content and a loss of cation groups. Kim and coworkers isolated phenyl oxidation to phenol in model studies, [6] and supporting computational work from Hendon and coworkers suggests the aromatic regions of the polymer are the weak sites for oxidation. [7] However, even fully-sp^3-hybridized polymers were found to oxidize. The exact degradation mechanism is complicated, but likely includes both electrochemical reactivity by direct oxidation, perhaps coupled with OH^- attack, of the polymer and chemical reactivity with oxygen radical species and other reactive OER intermediates. PTFE does not oxidize, showing promise for advanced electrode designs using stabilizing additives. Ionomers were not found to oxidize in KOH, suggesting a difference in double layer structure at the catalyst interface.

Earth-abundant oxygen-evolving anode catalysts

The activity of earth-abundant (particularly Ni, Fe, and Co-based) catalysts for OER has been extensively studied in alkaline conditions. [8-10] For all mixed-metal oxyhydroxides, and the oxides/sulfides/phosphides etc. that serve as pre-catalysts to the oxyhydroxides, [11-13] Fe is essential for high activity. [14-15] Fe-containing Ni oxyhydroxides are the most active catalyst in alkaline media, [16] with turnover frequencies 10-fold higher than IrO_x. [17] Co oxides/oxyhydroxides have a lower activity but are more structurally stable under OER conditions. The active catalysts phases in both cases are typically molecular-scale metal oxo-/hydroxo species that under OER conditions oxidize from a nominally layered double hydroxide to an oxyhydroxide structure. The transition metal

oxidation, i.e. formally Ni^{2+} to Ni^{3+}, is generally accompanied by a large increase in electrical conductivity, which contributes to the high performance. [10]

   While structure-composition-performance relationships have been identified in three-electrode studies with supporting electrolyte, it is unclear how these translate to AEM devices fed with pure water. Despite their high OER activity, Ni-Fe-based catalysts tend to show poor activity and stability in a pure-water membrane-electrode assembly (MEA) environment. [18] We found that $NiFe_2O_4$ nanoparticles failed rapidly during electrolyzer testing, but Co_3O_4 nanopowders performed the best out of all non-PGM catalysts tested and showed comparable performance and stability to high-surface area commercial IrO_x. [19] XPS analysis showed that the least-stable catalysts undergo significant surface transformations during operation. The electrolyzer operating voltages trended with the dry powder electrical conductivity, indicating the catalysts were limited by electronic conductivity and not fully restructuring to the conductive oxyhydroxide phase during operation. This observation is likely due to the use of an anion exchange ionomer to supply OH^- ions rather than a supporting electrolyte. The hydroxide is confined to near the ionomer cationic backbone and not able to transport through the layered sheets, inhibiting the transformation.

   We attribute the better performance of Co_3O_4 to its high electrical conductivity and resistance to structural rearrangement during operation. Notably, others have shown Ni-Fe oxide catalysts perform well in AEM devices when fed with KOH[20-21] or in pure water when using a thin layer of NiFe catalyst on a conductive supporting substrate, likely to compensate for the poor electronic conductivity of the material when not fully converted to the oxyhydroxide form. [22-23]

Perspective and outlook

AEM electrolysis is positioned to play a key role in the predicted exponential growth of green hydrogen technology with essential R&D advancements in the coming years. We revealed key design parameters essential to commercialization. First, stable alkaline OER catalysts with high electronic conductivity and minimal surface reconstruction during operation must be designed. Alkaline catalyst layers must also be applied to the MEA with scalable, industrially relevant techniques. Second, ionomer oxidation mitigation strategies must be developed. This approach could also target creative catalyst layer design, such as phase-separation control to protect oxidation-prone organic components or catalyst engineering to direct selectivity for hydroxide over polymer oxidation. If competitive efficiency and durability can be achieved in pure water, AEM electrolysis has the potential to become the dominant electrolyzer technology of the future.

CHAPTER VI

FUTURE APPLICATIONS: MEMBRANE ELECTROLYZERS FOR IMPURE-WATER SPLITTING

Grace A. Lindquist, Qiucheng Xu, Sebastian Z. Oener, and Shannon W. Boettcher

This chapter contains co-authored work previously published in *Joule* in 2020. Reproduced with permission from [*Joule.* **2022,** *4,* 12, 2549-2561]. Copyright 2020 Cell Press. The work was written and organized by myself with some sections written by Qiucheng Xu. Editorial assistance was provided by Sebastian Z. Oener and Shannon W. Boettcher.

Introduction

With further research and development, AEM systems may be suited to operate in impure water. During AEM electrolyzer operation (Figure 6.1a), water can be fed only to the anode where it would diffuse as a neutral species across the AEM to the cathode due to a concentration gradient (the membrane must then be engineered to prevent cathode dehydration at the relevant current density). The membrane conducts OH^- generated at the cathode across the membrane to the anode where it is oxidized into water and oxygen. The flow of cationic impurities to the cathode from the impure water should be retarded by the membrane permselectivity (i.e., the selective conduction of anions over cations), which could reduce cathode-fouling rates. At the anode, water oxidation tends to be preferred over the oxidation of halogens, such as Cl^-, due to the locally basic conditions. [1]

The flow of OH⁻ from cathode to anode would also reduce the extent of anion exchange (as an example, Cl⁻ for OH⁻) in the AEM.
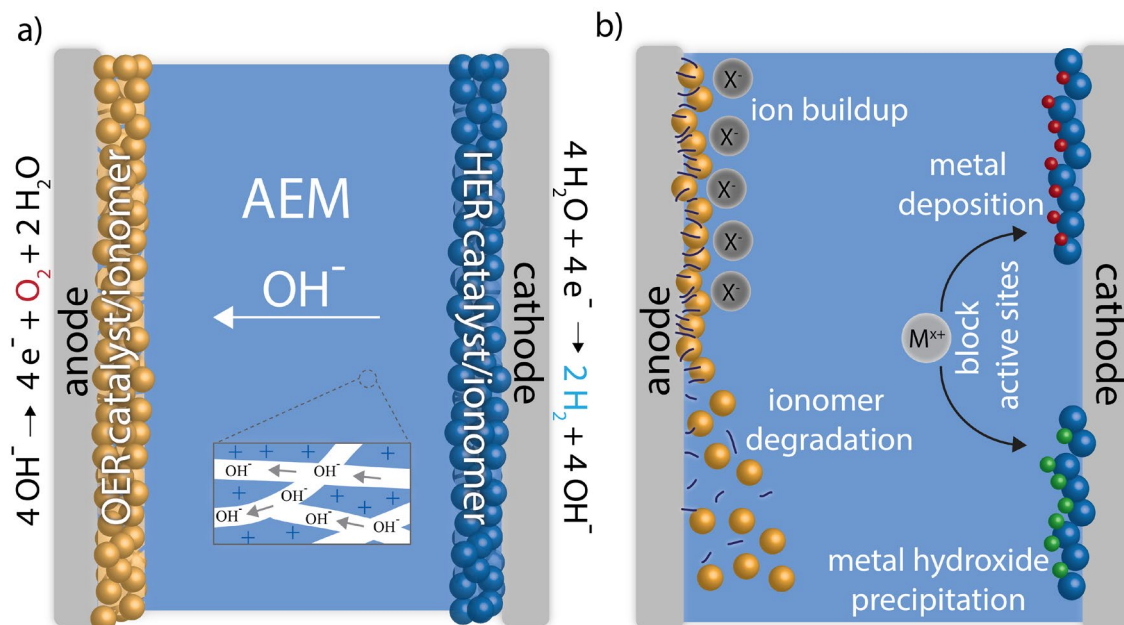
Figure 6.1. Schematic of an anion-exchange-membrane electrolyzer and possible degradation modes. (a) The device includes the alkaline exchange membrane (AEM) containing fixed quaternary ammonium groups that selectively conduct anions as well as anode and cathode catalyst layers supported on a conductive gas-diffusion layer. (b) Possible electrolyzer degradation mechanisms due to impurities.

To enable such new AEM electrolyzers, many technical barriers must be overcome. If the membrane permselectivity is low, cations will cross to the cathode where they can block active sites by either depositing on the surface or passivating and forming metal hydroxides (Figure 6.1b). Additionally, the preference for OER over Cl⁻ reactivity necessitates an alkaline environment, but the local pH conditions within the membrane electrode assembly (MEA) are not usually well defined or understood. Given the current state of electrolyzer technology, moving to an impure-water source would likely increase energy consumption (through lower efficiencies) and decrease durability,

the latter being of key importance for amortized capital costs. [2-3] Despite this, there has been much interest in using liquid-alkaline electrolysis systems (i.e., using a porous separator instead of a membrane) for the direct electrolysis of seawater. [3-5] While it is often argued that seawater electrolysis would reduce system costs by obviating water purification, the cost savings from not using pure water are negligible compared with the cost of electrolyzer operation, as Dresp et al. have discussed, and might only motivate such systems for niche applications, such as O_2 generation, for life support in underwater applications where space is at a premium. [5]

Understanding and mitigating degradation mechanisms caused by ionic and other contaminants is, however, important for increasing long-term durability and tolerance against subsystem failures, for example, of water-purification components. Minimizing water pretreatment, while maintaining high electrolyzer performance and lifetime, would also reduce operational costs. In this regard, moving to any water source less pure than ultrapure (typically 18.2 MΩ cm) water[3] is progress toward fault-tolerant electrolyzers. This includes a broad range of quality, including natural fresh-water sources, tap water, deionized water, gray water from municipal sources, brackish water, and seawater.

Minimal water pretreatment and maintenance, a long lifetime (ideally > 25 years), and efficient operation at high current densities (2 A cm^{-2} or higher) are all key for optimal electrolyzer scaling. These features minimize both operational costs (by maximizing kg H_2 kW^{-1} h^{-1}) and capital costs, which decrease for a fixed electrode area with increasing current density. An electrolyzer would ideally utilize only inexpensive, earth-abundant materials for the catalyst, bipolar plate, and gas-diffusion electrodes and use a low-cost membrane, for example, based on a hydrocarbon backbone instead of a

fluorocarbon one. [6] It would perform similar to, or better than, existing PEM systems with > 2 A cm^{-2} at < 1.8 V with a negligible voltage drift (for example, < 1 mV h^{-1} so that after 25 years the voltage would increase by only ~0.2 V) and enable high-purity hydrogen production at a cost of < \$2 per gasoline-gallon equivalent (gge) with appropriately inexpensive renewable electricity. [7]

Technical Barriers

OER Selectivity

The competition of halide reactions is one concern in dirty-water electrolysis. Research investigating OER selectivity has been focused on Cl$^-$ reactivity. Other halogens, such as Br$^-$ and F$^-$, are also present in relevant concentrations in seawater, brackish water, and tap water. [8-9] While F$^-$ oxidation occurs at > 3 V versus SHE and, thus, is not a concern, Br$^-$ oxidation could compete with OER. Oxidation reactions involving I$^-$ occur at potentials more-negative than OER at all pH and, thus, can also occur; however, I$^-$ is not present in significant concentrations for most water sources of interest and is commonly not discussed.

The selectivity trends for OER over the chloride- and bromide-oxidation reactions has been explained by thermodynamics (Figure 6.2). [10] Under acidic conditions, the chlorine-evolution reaction (CER, E^o = 1.36 V versus SHE) competes with OER (E^o = 1.23 V versus SHE) due to faster kinetics (CER is a 2e$^-$ process, OER is a 4e$^-$ process). Bromide evolution to form Br$_2$ (E^o = 1.08 V versus SHE) is thermodynamically and kinetically more favorable in acidic conditions. Seawater electrolysis, therefore, cannot be performed directly with a traditional PEM system due to Br$_2$ and Cl$_2$ co-generation, [11]

although selective catalysts for acid OER have been studied that appear to block Cl⁻ access to the catalyst surface. [12] In neutral-to-basic conditions, OER is argued to be thermodynamically preferred, as it occurs at a potential ~480 mV more negative than the competing 2e⁻ reaction to form ClO⁻. Therefore, by maintaining the solution pH at > 7.5 and using catalysts and/or currents where the OER overpotential is < 480 mV, OER is generally thought to be favored. [13]
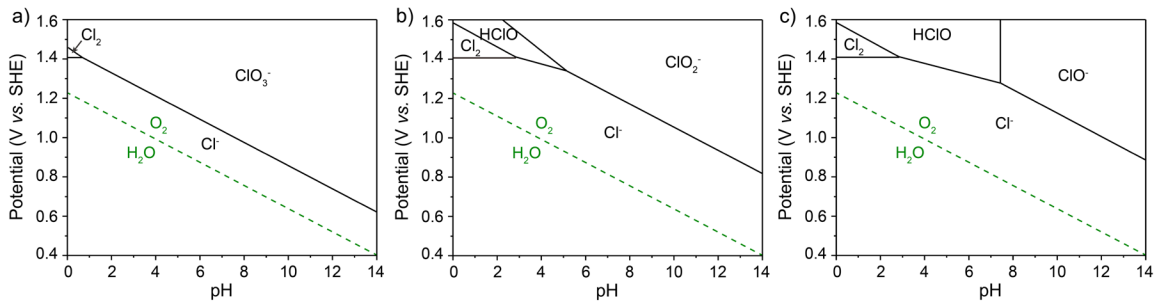
Figure 6.2. Pourbaix diagrams for chlorine showing different species. (a-c) (a) OCl⁻, (b) OCl₂⁻, and (c) OCl₃⁻ in 0.5 M Cl⁻ at 25 °C. (a) shows the species predicted by thermodynamics, while (b) and (c) show the Pourbaix diagrams obtained by ignoring the other oxidized Cl⁻ products.

A more complete assessment of the Cl⁻ oxidation products in an AEM electrolyzer might also consider the formation of, for example, OCl₂⁻ and OCl₃⁻. The Nernstian expressions (in V versus SHE, ignoring activity effects) for possible anode reactions are:

$$E_{O_2/OH^-} = 1.23 - 0.059 \cdot \text{pH} + 0.059 \log P_{O_2} \qquad (1)$$

$$E_{OCl^-/Cl^-} = 1.72 - 0.059 \cdot pH + 0.059 \log \left[OCl^-\right] \qquad (2)$$

$$E_{ClO_2^-/Cl^-} = 1.59 - 0.059 \cdot pH + 0.059 \log \left[ClO_2^-\right] \qquad (3)$$

$$E_{ClO_3^-/Cl^-} = 1.45 - 0.059 \cdot \text{pH} + 0.059 \log \left[ClO_3^-\right] \qquad (4)$$

$$E_{BrO_3^-/Br^-} = 1.42 - 0.059 \cdot \text{pH} + 0.059 \log \left[BrO_3^-\right] \qquad (5)$$

We note that $E^o_{ClO_3^-/Cl^-}$ and $E^o_{ClO_2^-/Cl^-}$ (in 1 M OH⁻) are only 0.22 V and 0.36 V more positive than $E^o_{O_2/OH^-}$.[21] Equations 2, 3, and 4 show that ClO_3^- is the dominant thermodynamic product under typical OER conditions at any pH, which can also be seen in the Pourbaix diagram in Figure 6.2a. However, the formation of ClO_3^- is a 6e⁻ process and is, thus, likely to be kinetically slow, consistent with the lack of ClO_3^- formation observed in mildly alkaline media. [14] The same argument might be made for BrO_3^-, where $E^o_{BrO_3^-/Br^-}$ is only 0.19 V more positive than OER, but is also a 6 e⁻ process. The formation of ClO_2^- (Figure 6.2c) is a 4 e⁻ process that could also compete with OER. Both chlorate reactions may go through a kinetic pathway involving OCl^- as an intermediate. It is likely that the oxidation products at the anode will be a mixture of OCl^-, ClO_2^-, and ClO_3^- (Figure 6.2c) with the speciation dependent on pH, current density, and mass transport. However, the competing kinetics of OER and CER appear not well understood, especially in impure-water conditions.

Several strategies have been reported for the design of OER-selective anode catalysts. These approaches have been discussed in detail elsewhere. [3-4, 11, 15] Ni-Fe oxyhydroxides, which are known to be the most-active alkaline-stable OER catalysts, [16-22] have been explored for OER selectivity. Dionigi et al. tested a Ni-Fe catalyst in 0.1 M KOH and a mixed 0.1 M KOH / 0.5 M NaCl electrolyte. They proposed that OER would be favored at overpotentials of less than 480 mV regardless of the presence of NaCl. Their system exhibited near-unity faradic efficiency for O_2 in both electrolytes. [13] The catalyst was then tested by Dresp et al. in an AEM electrolyzer operated at 1.6 V, below the pro- posed 480 mV overpotential limit, in a 0.1 M KOH / 0.5 M NaCl mixed electrolyte. A decrease in current density was observed upon the addition of NaCl, despite

the electrolyte conductivity increasing. This was attributed to Cl^- competing with OH^- transport. They reported operation up to 200 mA·cm^{-2} and > 100 h lifetimes, although current decreased throughout the run significantly in the presence of NaCl. [23]

Dresp et. al. further studied electrolyzer performance when NaCl was selectively fed to each electrode. The configuration fed with 0.5 M NaCl at the cathode and 0.5 M KOH at the anode operated at a current density 75 mA·cm^{-2} higher at 1.7 V than the symmetric system fed with a mix of the two electrolytes. The asymmetric cell operated at < 1.7 V at 1 A·cm^{-2}. The faradic efficiency at low current densities (100 mA·cm^{-2}) was near 100% but decreased with current density to 93.4% at 1 A·cm^{-2}, indicating Cl^- oxidation may be occurring, though no OCl^- was detected by titration. [24] While Na^+ did not appear to affect device stability over 12 h, natural saltwater feed to the system may poison the cathode due to other reducible cationic contaminants. Asymmetric impure-water flow could, thus, be a useful approach for seawater electrolysis in both PEM and AEM systems. These studies are an important step toward practical systems, though a better understanding of the mechanism for Cl^- oxidation suppression and studies in natural water with other competing contaminants remain needed.

Co-based catalysts have also shown selectivity for OER over halogen oxidation. Nocera and co-workers developed Co (oxy)hydroxide/phosphate (Co-P$_i$), Co (oxy)hydroxide/borate (Co-B$_i$), and Ni (oxy)hydroxide/borate (Ni-B$_i$) catalysts that operate in electrolytes of a range of purity. [25-27] Surendranath et al. showed OER performance for Co-P$_i$ catalyst in 0.1 M K$_3$PO$_4$ buffer containing 0.5 M NaCl that matched that in buffer made with pure water. Elemental analysis revealed a 6:1 ratio of Na^+ to Cl^- in the film, indicating exchange of Na^+ for K^+ but low incorporation of Cl^-.[25]

Esswein et al. investigated the performance of Co-P_i in 1.0 M borate buffer prepared using natural river and ocean waters. Compared with electrolyte prepared with pure water, a lower overpotential was observed in river water, but a higher overpotential was observed in ocean (salt) water. This discrepancy was attributed to cations, such as Ca^{2+} and Mg^{2+}, in ocean water deactivating the catalyst. [27] This could be due to M-OH precipitates forming on the surface, either blocking active sites or disrupting the formation of the active-phase (oxy)hydroxide. Keane tested Co-B_i and Ni-B_i films in natural seawater and showed 100% faradic efficiency for OER over Cl^- and Br^-.[26] This work highlights the necessity for understanding the roles of all the various impurities present in natural water. Future work could also focus on understanding the impurity effects in an MEA configuration where pH and concentration are not controlled.

Blocking layers have also been used to repel Cl^- from the active catalyst surface. MnO_x layers, for example, typically provide >90% OER selectivity across a wide pH window from 1 – 10. [28-30] Vos et al. found that depositing MnO_x onto IrO_x increases the OER selectivity from 14% to >90% in pH conditions < 1, where CER is thermodynamically and kinetically favored. [12] The MnO_x film acts as a noncatalytic, permeable, cation-selective overlayer that slows Cl^- transport. [12] Kuang et al. reported a multilayer Ni-Fe/NiS_x-Ni anode electrocatalyst with near-unity faradic efficiency for OER in alkaline electrolyte, even when operating at an overpotential of 560 mV. They hypothesize that polyatomic sulfate- and carbonate-rich passivating layers are generated *in situ* and retard Cl^- transport to the active catalyst surface during saltwater splitting. [31] The system was operated at up to 1 A·cm^{-2} over 1,000 h in 1 M KOH containing 0.5 M

NaCl. While this was a significant step toward higher-current-density studies, the cell potential at 1 A·cm^{-2} was 2.44 V, which is high for a KOH-based system. [32]

Cation Poisoning

OER catalysts are also susceptible to failure in the presence of cationic contaminants. In addition to the aforementioned degradation of Co-Pi by Ca^{2+} and Mg^{2+} in seawater, [27] Zaffran et al. showed Ni-Fe oxyhydroxide catalysts operated in electrolyte containing alkali-earth metals decreased OER activity. [33] Clearly cations can have detrimental effects at the anode and it would be useful to further study the failure mechanisms.

Table 6.1. Maximum contaminant levels (MCLs) for cations in drinking water

	Contaminant	MCL (mg/L)
Primary	Barium	2
	Chromium	0.1
	Selenium	0.05
	Arsenic	0.01
	Antimony	0.006
	Cadmium	0.005
	Beryllium	0.004
	Tellurium	0.002
Secondary	Zinc	5
	Copper	1.3
	Iron	0.3
	Aluminum	0.2
	Silver	0.1
	Manganese	0.05

Cationic contaminants can also be detrimental at the cathode. OH$^-$ is produced at the cathode during the hydrogen evolution reaction (HER). As discussed by Tong et al., this locally basic pH can precipitate divalent cations, [3] such as Ca^{2+} and Mg^{2+}, as

hydroxides and could, thus, block catalyst active sites (Figure 6.1b). The ions Ca^{2+} and Mg^{2+} may transport (slowly) as co-ions through the AEM, which has imperfect permselectivity, to arrive at the cathode. Impure waters—such as tap water—also contain a number of other possible metal impurities (Table 6.1). [9] Of these impurities, Ag^+ and Cu^{2+}, for example, have sufficiently positive E^o values such that they will electroplate on the cathode under HER conditions and likely deactivate it. [34]

While most cationic impurities have negative effects during electrolysis, cationic Fe impurities appear essential for stable OER activity in alkaline conditions with earth-abundant catalysts. The dynamic role of Fe in alkaline OER catalysis has been studied extensively. [16-22] Zhang et al. showed that when Fe^{3+} is introduced into KOH electrolyte, it binds to pure CoO_xH_y, activating it for OER, but the binding is reversible and Fe readily leaches when OER is then driven in Fe-free KOH. [21] Diaz-Morales proposed this process can be used to engineer balanced dissolution and deposition and thus stability. [35] Chung et al. showed that by tuning the Fe content and Fe-cation binding energy, the dissolution and redeposition can be optimized to result in a dynamically stable system. [36] A Fe-NiCu hydr(oxy)oxide catalyst in 0.1 M KOH spiked with 0.1 ppm Fe had lower dissolution rates but increased current densities compared with the Cu-free analog, which they attribute to the optimal Fe-Cu adsorption energy and therefore higher Fe coverage. [36] Liu et al. applied this under- standing of dynamic Fe sites to develop a "corrosion-engineering" approach for OER electrode preparation and operation. A Fe-foam electrode was soaked in mildly acidic (pH 5–6) aqueous solutions containing Ni^{2+}. Corrosion reactions led to the formation of a layered double-hydroxide structure on the surface that drove OER at a 340 mV overpotential at 1 A·cm^{-2} in 1 M KOH. The catalyst operated at 1

A·cm^{-2} for >8 months without large voltage changes. [37] The dissolution and deposition processes and catalytic mechanism resulting in stability at high current densities should be better understood and investigated in KOH as well as AEM electrolyzer configurations (with and without soluble base) to further applications.

Membrane and Ionomer Performance and Stability

While much effort has been directed toward catalyst development, further membrane and ionomer innovation for use with impure-water feed is needed. AEM and ionomer stability and performance are the major limitations in the development of AEM electrolyzers, regardless of water-feed purity. [1, 3-4] It thus remains of critical fundamental and practical importance to understand and mitigate degradation mechanisms in these components under operating potentials. It is also important to distinguish between the membrane and ionomer. Catalysts are dispersed with soluble anion-conducting ionomers to provide pathways for ion conduction to the high-surface-area catalyst. The ionomer is susceptible to the same degradation pathways as the membrane but is susceptible to additional oxidative degradation modes, as they are located at the catalyst interface where the OER occurs. Organic materials are notoriously difficult to stabilize under alkaline OER conditions, as has been shown for various carbon blacks. [38-39] Understanding degradation modes is limited by the lack of established baseline AEM materials, as degradation appears to vary substantially with membrane and ionomer structure (Figure 6.3). [31, 40-43] For PEM systems, Nafion has become uniformly adopted, but there is no such analog for AEMs.

Figure 6.3 shows some possible failure mechanisms of various AEMs. Multiple chemical-degradation pathways have been identified for a variety of membranes in pure water. Ionomers are susceptible to nucleophilic substitution, elimination, phenyl oxidation, and methyl and/or proton-rearrangement reactions, depending on polymer structure (Figure 6.3). [31, 40-41, 44-45] Water-transport limitations enhance degradation due to locally increased OH$^-$ concentration. [46-48] These pathways break down the membrane structure (leading to possible solubility of ionomer fragments) and lead to loss of charged end groups (reducing ion conductivity). Fenton oxidation processes (involving Fe species) forming radical oxygen species can also degrade the ionomer and membrane. [49-51] Fenton processes may be a prominent source of degradation in AEM systems with active nonprecious-metal OER catalysts that all contain Fe but have not been studied extensively in this context.
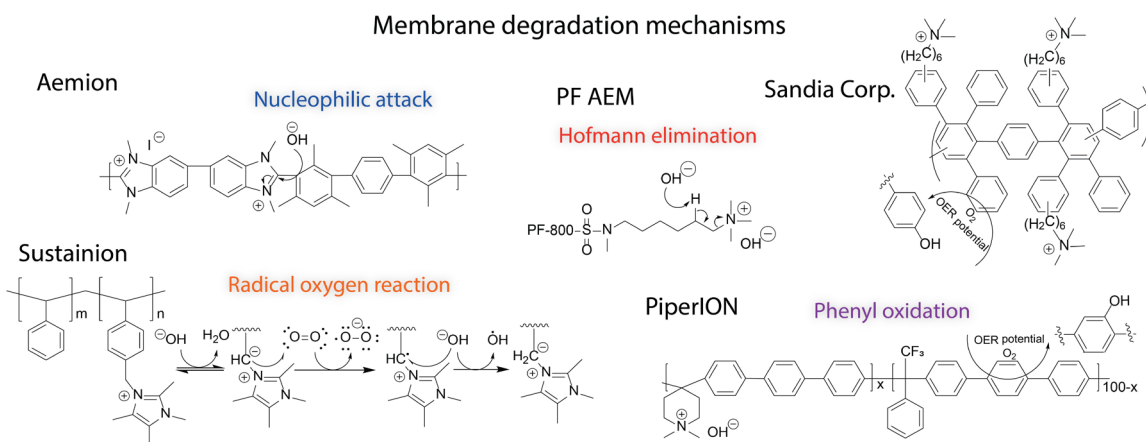

Figure 6.3. Possible AEM degradation mechanisms. The chemical reactions shown are not the only possible degradation pathways and are not specific to the designated membranes, which are used as examples only.

Many of these chemical-degradation pathways can be addressed by advanced polymer development, as discussed by Gottesfield et al. [51] One route to mitigate chemical

degradation is maintaining a high level of hydration in the membrane. AEM electrolyzers are already susceptible to membrane dehydration at the cathode, and this is accelerated in the presence of ionic salts. [52] Controlling water content in the system is thus key in mitigating membrane degradation, and will likely become increasingly important in impure water.

Physical degradation of the membrane is another issue that is likely accelerated in dirty water. Just as metal hydroxides can deposit to poison the cathode, these precipitates can mechanically damage the membrane and/or ionomer causing irreversible performance loss. Ionic contaminants can also affect mass transport and lead to performance losses even when not involved in faradic processes. In the context of membrane electrolyzers, ions can be classified as those with the same charge as the fixed membrane charges (co-ions) and ions of opposite charge to the fixed mem- brane charges (counter-ions). Counter-ions directly compete with H^+ transport in the PEM and OH^- transport in the AEM. In PEM fuel cells, ionic contaminants have been shown to intercalate into the cation-exchange membrane, [53] increasing membrane resistivity and slowing water transport, therefore increasing membrane hydration. [54] Degradation at the metal catalyst/ionomer interface, already a significant site for degradation, was found to accelerate in the presence of cationic contaminants. [54-55]

A recent modeling study, however, has indicated that ion exchange, resulting in decreased ionic resistance in the bulk membrane phase, is likely not a significant issue. When comparing an AEM electrolyzer fed with KOH with one fed K_2CO_3, Stanislaw et al. showed that ion exchange by HCO_3^-/CO_3^{2-} did not substantially affect conductivity. [56] In contrast, the electrode interfaces are strongly influenced. As carbonate species are not

involved in the faradic reactions, they accumulate at the anode. This leads to concentration polarization[57] and a Nernstian voltage loss due to the lower concentration of OH^- at the anode relative to the cathode (i.e., a pH gradient).[56] Other contaminant anions are likely to lead to similar results.

Many of the opportunities and challenges of membrane-based impure-water electrolysis are shared with the established field of electrodialysis where ions can be separated via permselective membranes in the presence of an electrochemical potential gradient.[58] Reviews on electrodialysis by Strathmann and others are available.[58-61] Electrodialysis has also been specifically proposed for desalination and purification of water feeds of various impurity levels.[62-64] Membranes that are nominally selective for transport of counter-ions (i.e., anions in an AEM) over co-ions (i.e., cations in an AEM) motivate their use as ionic barriers for unwanted co-ion transport. However, the permselectivity is strongly affected by various factors,[64] including membrane hydrophilicity[65] or the co-ion concentration in the adjacent electrolyte.[66] In electrodialysis, these permselectivity properties limit the product purity, e.g., of acid and base solutions produced.[67] In terms of increasing the resilience of water electrolyzers with respect to the water-feed purity, limited permselectivities in available membranes put an emphasis on advanced membrane development.[68] Electrodialysis and related fields can, thus, inform advanced membrane design for higher resilience against ionic contaminants in the water feed of electrolyzers.

Outlook

Membrane and Ionomer Improvements

One key research direction is to distinguish between degradation mechanisms of the bulk membrane, membrane interfaces, ionomer binders, and the catalysts themselves in the presence of pure water, pure-water alkaline electrolyte, and impure-water feeds. A recent study by Li et al. probed the performance difference observed when varying the chemical structure of the binder polymer using the same membrane. [69] They showed that the performance depended on the ionomer structure and loading. This was attributed to interfacial pH control. Phenyl groups in the polymer backbone can oxidize to form phenol (Figure 6.3), which was hypothesized to decrease surface pH and neutralize hydroxide associated with the cationic ionomer groups. [43] By removing phenyl groups in the ionomer backbone, they hypothesize that oxidative degradation is mitigated and a higher local pH is maintained. Future research could work to understand the performance and stability of ionomer binders at the membrane interface.

There are other possible routes to advance membrane electrolysis by controlling ion flow for impure-water feeds. For example, bipolar membrane (BPM) electrolyzers operate the cathode at an acidic cation-exchange layer (CEL) and the anode at an alkaline anion-exchange layer (AEL) surface. To maintain the two dissimilar pH environments at steady state, water is dissociated (H_2O 4 H^+ + OH^-) inside a narrow junction region between the CEL and AEL (Figure 6.4). [70] Recently, we studied the water-dissociation catalysis occurring inside the bipolar junction, realizing BPM electrolyzers that can match the performance of conventional AEM electrolyzer-control de- vices up to ~ 0.5 $A \cdot cm^{-2}$. [71] Compared to conventional AEM electrolyzers, a locally acidic environment is provided at the cathode, resulting in a kinetically favored environment for hydrogen evolution.

A key feature of BPMs is that ion flow occurs via H^+ and OH^- moving out from the center of the BPM through the cation- and anion-exchange layers, respectively. This constant *outward* ionic flux should substantially retard the crossover of other counter-ions (i.e., ionic contaminants), significantly reducing ion crossover in the system. Blommaert et al. showed that the outward H^+ flux in a BPM suppresses the K^+ crossover to the cathode in an H-cell setup.[72] At 5 mA·cm^{-2}, the K^+ flow is negligible, highlighting an interesting approach to mitigating contaminant-ion crossover during electrolysis. Such functionality has not been explored for increasing system tolerance against ionic contaminants.
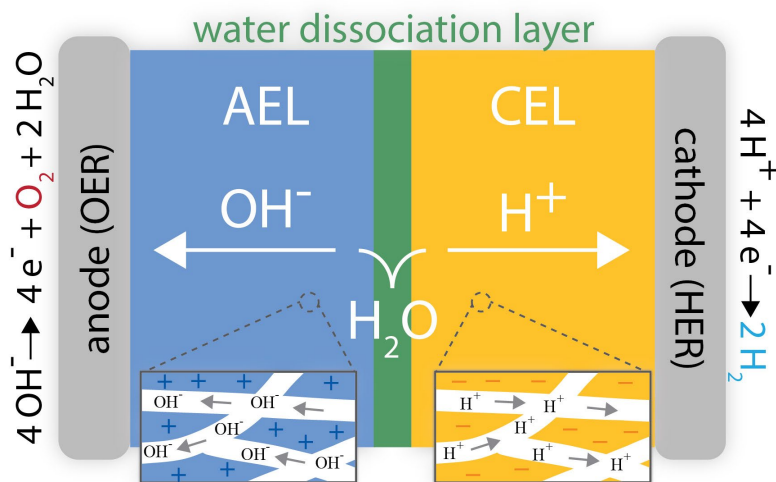
Figure 6.4. Bipolar membrane electrolyzer. The electrolyzer operates the anode in locally basic conditions, ideal for water oxidation, while the cathode is in locally acidic conditions, ideal for hydrogen evolution. The ionic current is predominantly out from the center of the BPM, perhaps retarding crossover of unwanted impurity ions like Cl^-.

Co-ion conduction has been studied in BPM systems, but the underlying factors that modulate the relative transport efficiency of H^+ and OH^- relative to co-ions have not been fully articulated. A review from Luo et al. discusses the complexity of transport in

ion-selective membranes. [64] As the AEL and CEL can be processed independently, tuning membrane parameters of each layer, such as pore size and membrane thickness, could be an effective approach to achieve optimum performance. Recently, Oener et al. showed that thinning the CEL improves BPM performance, presumably due to improved water transport to the BPM junction, [73] while Mayerhofer et al. showed improvement from thinning the AEL. [74] However, this will likely decrease system tolerance to either anion or cation crossover.

Rather than rely on membrane permselectivity, alternative approaches may be necessary to control ion contamination. The junction chemistry might be engineered to promote water dissociation and introduce additional components to provide further barriers to co-ion crossover. Membrane and junction parameters could also be tuned to favor specific ion-transport mechanisms (e.g., Grotthuss mechanisms to transport H^+ and OH^- over vehicular transport of co-ions) and selectively modulate ion transport and contamination, rather than simply block ion crossover.

Electrocatalyst Engineering

While most approaches to impurity-tolerant electrolyzers focus on the anode reactions, additional improvements might be made at the cathode through careful design that could address problems broadly facing electrolyzer technology, not just AEM systems. Cation poisoning might be overcome by optimizing water flow rate and current density to minimize co-ion transport or through engineering approaches. For example, because earth-abundant catalyst materials are inexpensive, high catalyst loadings (e.g. >10 mg cm^{-2}) can be used, as long as the electrode structure and conductivity are

119

maintained in the MEA. Impurity deposition will occur nearest to the membrane, perhaps leaving catalyst further from the membrane unaffected.

Understanding the relationships between catalyst durability in impure water and the morphology, composition, and phase of the catalyst material is also important. For example, Ag^+ and Cu^{2+}, which have already been mentioned as metals that may be reduced on the cathode, deposit in face-centered cubic (fcc) crystal structures, which is the same structure that Pt adopts. By choosing cathode catalysts with crystal structures incommensurate with these poisoning metals (for example, MoS_2 which adopts a layered 2D hexagonal structure), this deposition might be avoided.[85] Impurities that deposit as fcc metals are not expected to epitaxially deposit onto the surface of MoS_2 in a way that blocks active sites at sheet edges and defects. [75] High-surface-area earth-abundant catalysts, with ~103 higher loading than precious-metal counterparts, would also be expected to degrade more slowly via these mechanisms. Impurity deposition might be relegated to specific regions of the catalyst, for example, near the membrane or near the outer surface, leaving interior active sites pristine. Because these processes are likely to occur in all electrolysis systems (albeit at different rates due to different concentrations of impurities), understanding the relationships between the poisoning capacity of trace metals in impure water, crystal structures of the electroplated impurities, and catalyst structure are broadly important research directions.

Conclusion

Much of current impure-water electrolysis research is aimed toward direct saltwater electrolysis. Expanding the research focus to include a variety of impure-water sources

and developing a mechanistic understanding of the underlying processes could lead to enhanced lifetimes and durability more broadly in electrolyzer technology. While significant effort has focused on the catalysts, particularly for the OER, membrane and ionomers have received less attention, and approaches are needed to establish performance and durability at higher current densities in electrolyzer hardware with various water feeds and impurities. Understanding ion crossover in these membrane systems is crucial, as is obtaining reliable and reproducible baseline data on membrane and ionomer performance. Understanding Cl^- reactivity at the anode and distinguishing between different possible products as a function of conditions would be useful for designing robust, selective anodes. Attention should also be directed toward preventing cathode fouling and considering HER-catalyst crystal structure, morphology, and loading effects.

Membrane electrolysis to generate green hydrogen fuel is expected to grow rapidly[2] and contribute substantially to the renewable economy. Advances in membrane technology will accelerate the growth of this industry to meet future renewable hydrogen demands. Developing membrane electrolysis systems that are more robust and tolerant of feed-water impurities could play a significant role in improving electrolyzer lifetimes, reducing capital costs, and lowering maintenance expenditures, while expanding electrolyzer technology applications.

APPENDIX A

CHAPTER II SUPPLEMENTAL INFORMATION

Additional notes on electrode coating

The stainless-steel material has a graded porosity, so it is important the catalyst be coated on the layer with smaller pores (visually smoother side). When applying catalyst, the airbrush was held 5 to 8 cm from the hot plate and the catalyst was sprayed in short, even bursts of the airbrush to prevent any large droplets or catalyst aggregation. The hot plate was rotated every few sprays to ensure even coating. Slow coating was found essential, as the ink will soak into the bulk of the material if too wet and will result in an inconsistent top coating. Inks were sprayed in short bursts while waiting multiple (5-10) seconds between each burst. The solvent evaporation can be observed as the coating color changes from dark to light. Additional ink was not added until the previous layer was visually dry. A progression of coating a GDL is shown in Figure A.1 with an example of an electrode sprayed too quickly (Figure A.1e).

The IrO_2 catalyst was found to be particularly difficult to disperse. The ink was sonicated until it was fully opaque and would remain on the side of the vial before dripping down when swirled or shaken. These visual indicators are not intended to be a quantitative determination of the solution dispersion, but rather a qualitative check that the catalyst is dispersed. The catalyst dispersion was periodically checked throughout coating. If catalyst was observed to collect at the bottom of the vial, the ink was sonicated an additional ~60 s until re-dispersed.
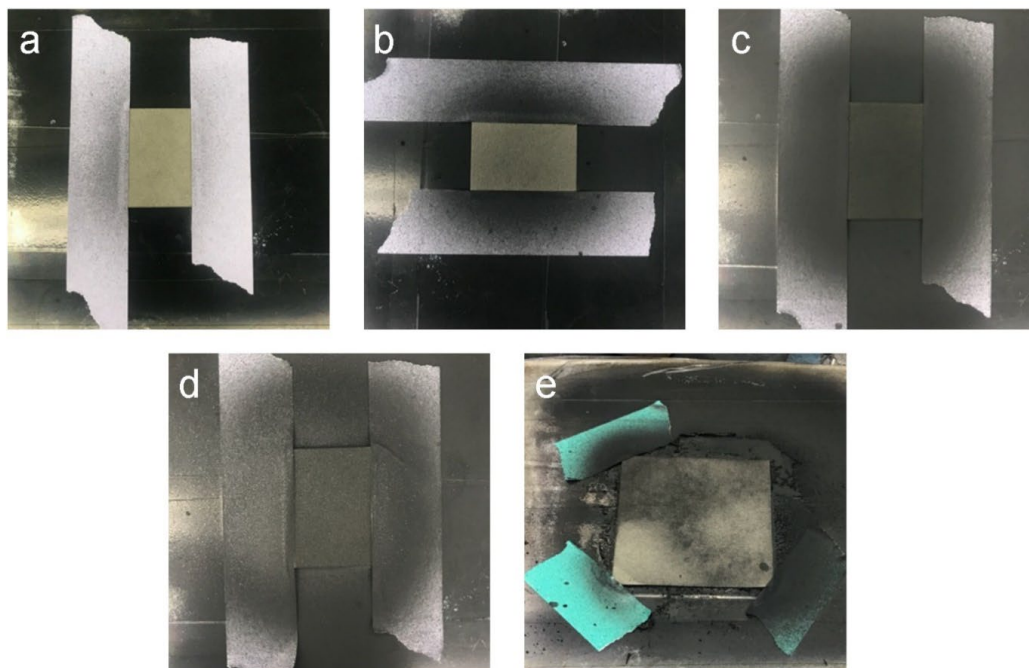
Figure A.1. Progression of spray coating stainless-steel GDLs. a) The color starts very light. Continue spraying slowly, ensuring the ink dries between layers. b) The hot plate is rotated to ensure even coverage. The color will start to darken slowly. c) The GDL is similar color to the coated tape when full loading is achieved. d) A thin layer of ionomer solution is sprayed on top of the catalyst. e) If coating too quickly and the GDL gets too wet, the material pulls the ink into the bulk leaving bare surface. Even after continued spraying these areas will not coat.
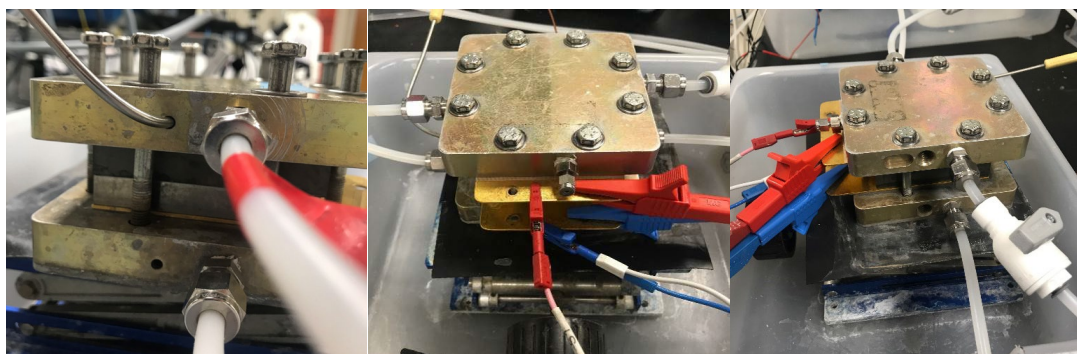

Figure A.2. Electrolyzer photos including side view showing thermocouple insert for monitoring temperature in the electrolyzer. The thermocouple is placed in the outer hardware on the cathode side.
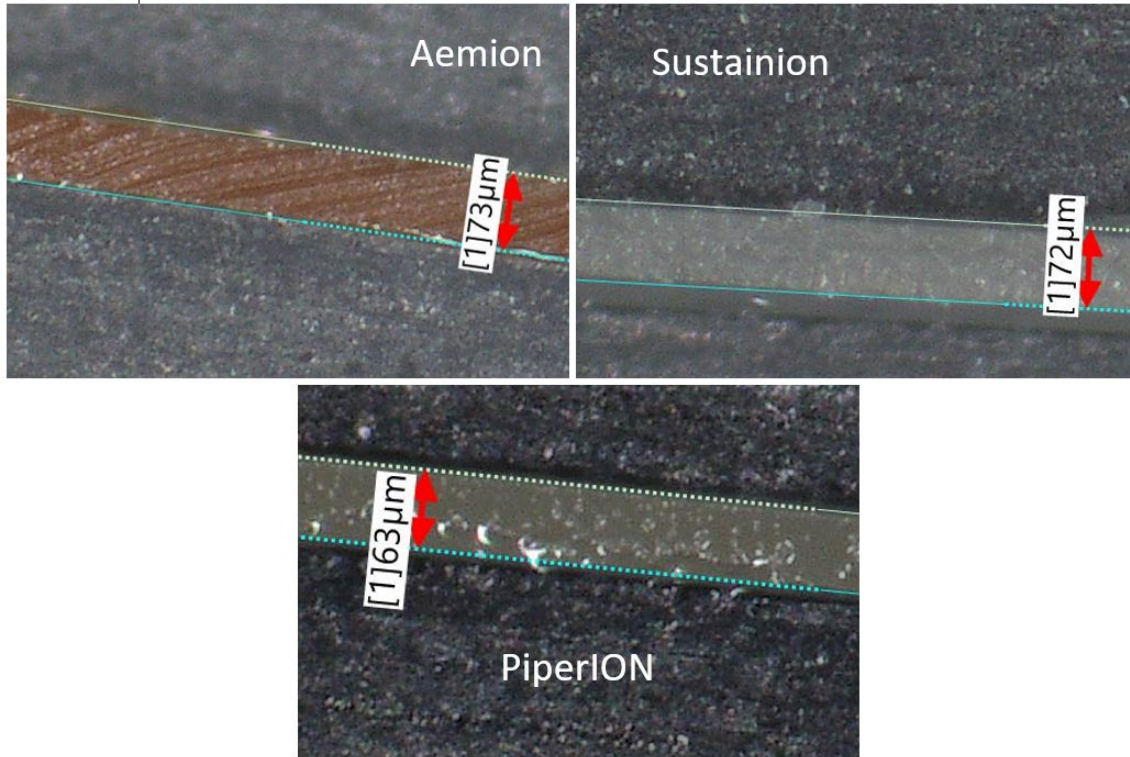
Figure A.3. Thickness of membranes hydrated in KOH. Membranes were clamped between two glass slides and thickness measured with a Keyence VHX 7000 digital microscope.
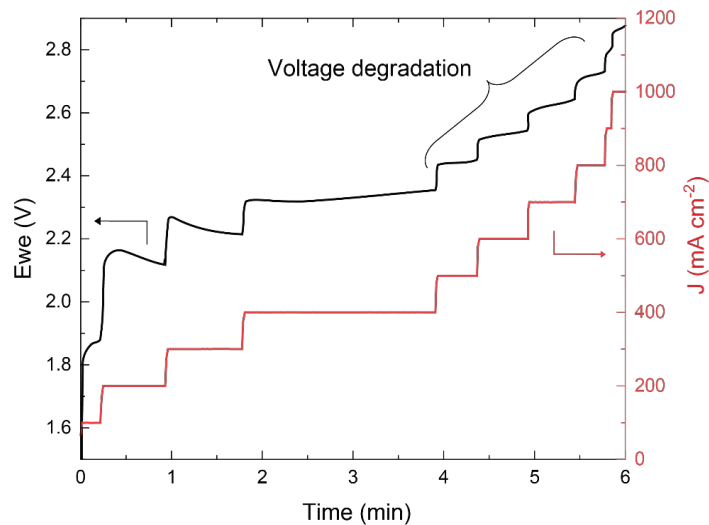
Figure A.4. Aemion operation at 69 °C. The high temperature causes the membrane to break down, as is observed by the voltage degradation (as opposed to the expected stabilization) at each current step.

Figure A.5. Effect of ion exchange on Aemion operation. Significant performance enhancements were observed when pre-soaking the membrane in 3 M KOH (black) versus 1 M KOH (red), showing the importance of sufficiently exchanging OH$^-$ for I$^-$ in the membrane.
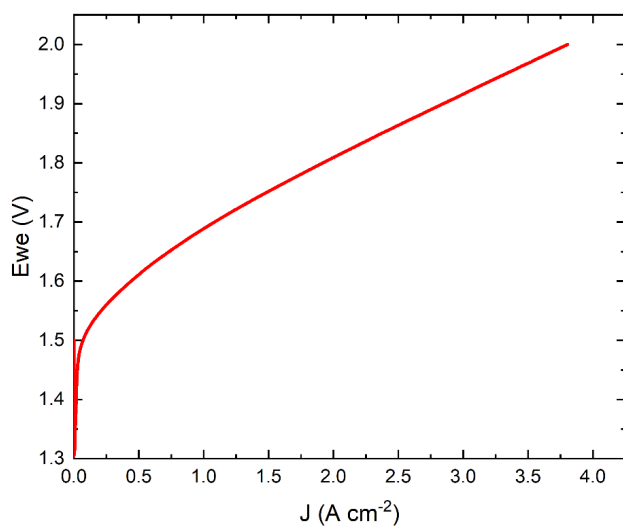
Figure A.6. Polarization curve of AEM electrolyzer prepared with baseline materials in 1 M KOH at 55 $\pm$ 1 °C.

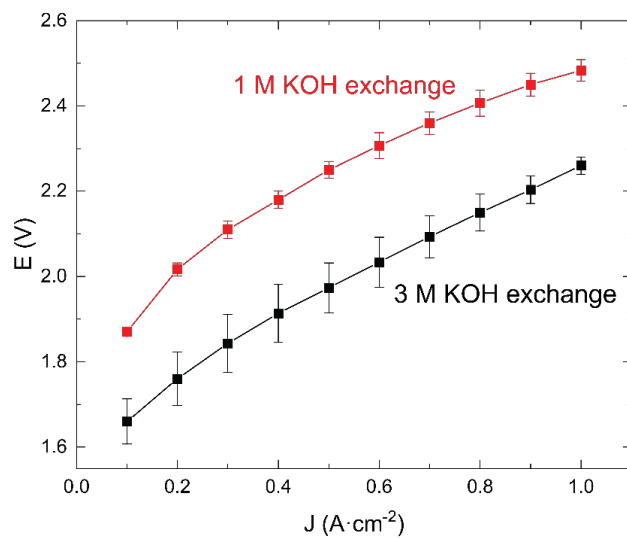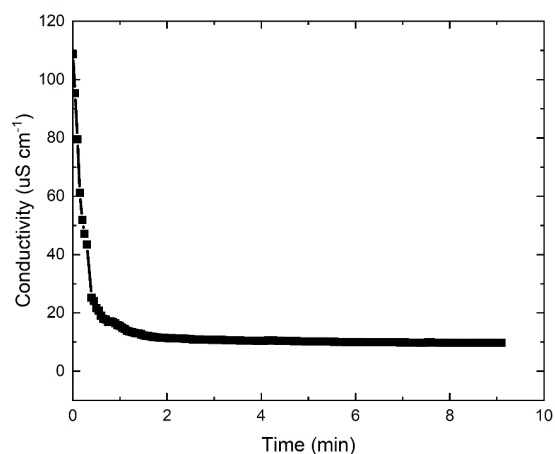**Figure A.7.** Conductivity of effluent electrolyte measured after the initial 500 mL of water had been purged through the electrolyzer.
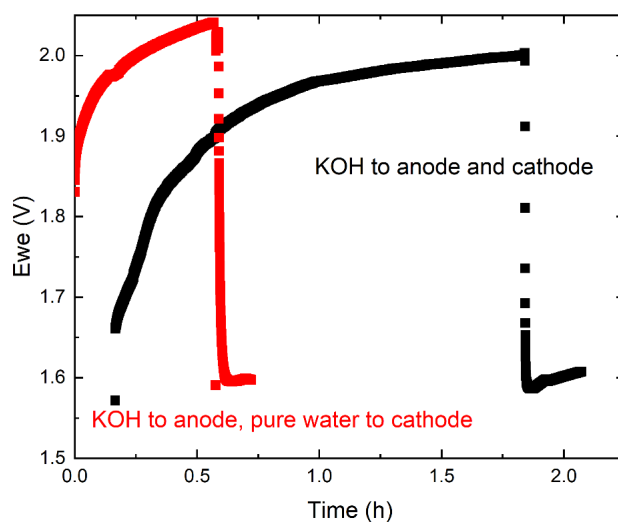
Figure A.8. Changes in degradation behavior in pure water and KOH. The cell was operated at 55 $\pm$ 1 °C. After conditioning in pure water, the cell was operated at 500 mA cm^{-2} and the voltage degradation observed. The anode and cathode streams were then switched to 1 M KOH at the same temperature (black). Water was then purged to the system for > 10 min, or > 5 L of water. The same cell was then again operated at 500 mA cm^{-2} in pure water, then 1 M KOH was added only to the anode stream maintaining pure water at the cathode (red).
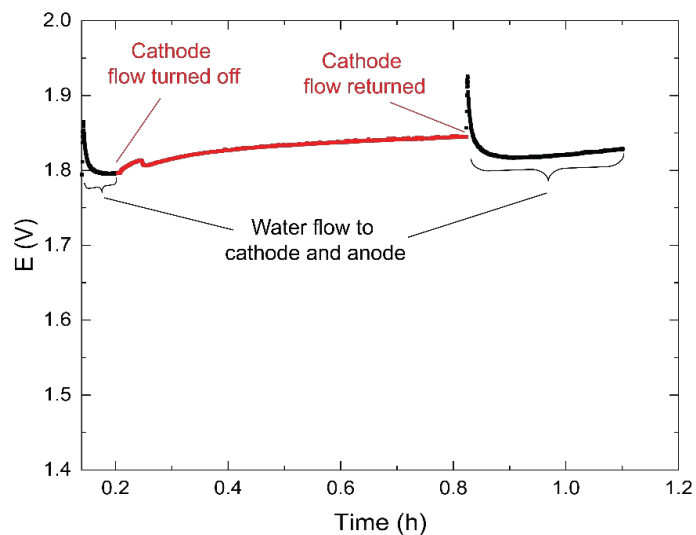
Figure A.9. Performance with different water feed modes. The cell was operated at 500 mA cm^{-2} at 69 ± 1 °C with water flowing to both the cathode and the anode. Water flow to the cathode was turned off and voltage degradation was observed before stabilizing (note – the small voltage recovery at approximately 0.3 h is attributed to water diffusing from the anode to the cathode after flow was turned off). After cathode flow was returned a partial voltage recovery was observed.

APPENDIX B

CHAPTER III SUPPLEMENTAL INFORMATION

Supplemental Materials and Methods

Catalyst Dispersions and Electrolyzer Operation. Co_3O_4 (99.9%, 15 nm), Co_3O_4 (99%, 10-30 nm), Co_3O_4 (>99.5%, 30-50 nm), Co_2O_3 (50 nm, US Nano) and CoO (50 nm, US Nano) nanoparticles were used at the anode. Cathode and anode inks were prepared identically to all experiments described in the main text. For every 100 mg of catalyst, 0.5 g of water, 1.7 g of IPA and 200 mg of 5 wt % TP-85 (Versogen) ionomer was added. Catalyst inks were sonicated for 1 h to disperse. GDL coating and MEA testing was conducted identical to electrolyzer experiments in the main text.

Faradaic efficiency measurements. The faradaic efficiency for the IrO_2 and Co_3O_4 anode catalysts was measured during operation in a pure-water-fed MEA. Two graduated cylinders were filled with water and inverted in the water bucket feeding the electrolyzer. The cell was operated at 20.5 °C and conditioned identical to the main body manuscript. After conditioning, the cell was returned to open circuit and water was flowed for 5 min (until all gas had excavated the water lines). The anode and cathode outlet feed tubes were then positioned under the graduated cylinders and 500 mA cm^{-2} was applied for 20 min. Water was then run for an additional 5 min to ensure all gas had accumulated in the cylinders, after which the gas volume was measured with the water level in the cylinder flush with the water in the bucket.

Catalyst layer conductivity measurements. Catalyst inks were sprayed on glass slides with a hand spray gun in a manner identical to GDL coating and dried at 80 °C. A

polarization curve was measured using a source meter unit (Keithley 2400) and the slope fit to obtain electrical resistance. Catalyst layer thickness was determined using a stylus profilometer.

Catalyst dissolution during electrolysis. Inductively coupled plasma mass spectrometry (ICP-MS, iCAP RQ, Thermo Fisher) was used to determine metal concentrations in the anode effluent stream of an electrolyzer operating with either a Co_3O_4 or $NiFe_2O_4$ anode catalyst. During operation, water was flowed to the anode and cathode, as for all other electrochemical testing. The cells were conditioned and operated identically to the durability testing in the main body section. During the 20 h durability testing at 500 mA cm^{-2}, 10 mL samples were collected from the water stream exiting the anode of the electrolyzer at various time points. Samples were collected in plastic centrifuge tubes that were previously acid cleaned to reduce any external metal contamination. The collected aliquots were then acidified with a small amount of concentrated, high-purity nitric acid (TraceMetal grade, Fisher Scientific) to stabilize any dissolved metal species. Metal concentrations were measured in kinetic energy discrimination (KED) mode to minimize isobaric interferences from polyatomic ions and with internal standardization using interpolation of ^{45}Sc and ^{89}Y intensities to correct for matrix effects. All calibration curves were linear with correlation coefficient greater than 0.999 for Fe, Ni, and Co.
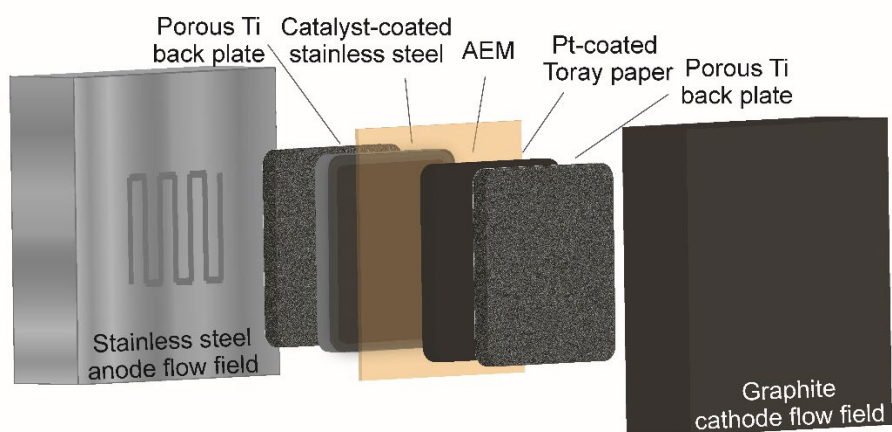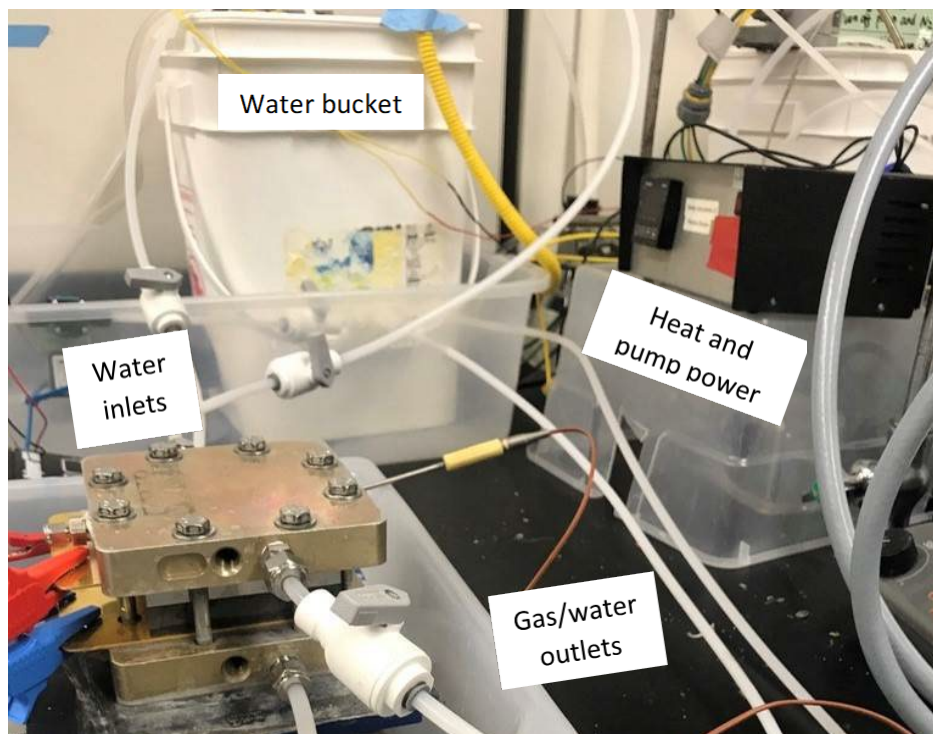
Figure B.1. Electrolyzer device for pure-water AEMWE testing. a) photo of home-built electrolyzer testing setup and b) schematic of internal 1 cm^2 MEA components.
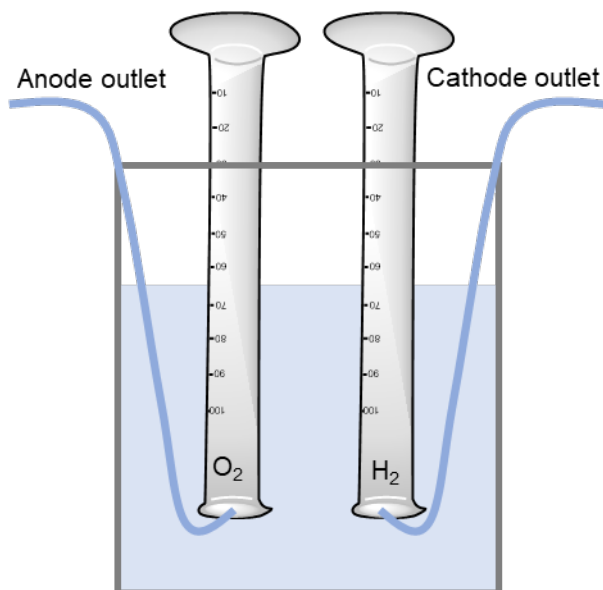
Figure B.2. Faradaic efficiency measurement experimental setup. The theoretical volumes for H_2 and O_2 produced at 500 mA for 20 min are 74 mL and 37 mL, respectively. The measured volumes for Co_3O_4 were 73.5 mL and 36 mL, or ~99% H_2 and ~97% O_2 efficiency. For IrO_2 the measured volumes were 73 mL and 36.1 mL, or ~99% H_2 and ~98% O_2. The lower efficiency could be attributed to a small amount of gas dissolving in water or gas escaping through tubing connections and not being measured in the cylinder. The lower O_2 efficiency relative to H_2 may also be attributed to oxidation of the ionomer at the anode.
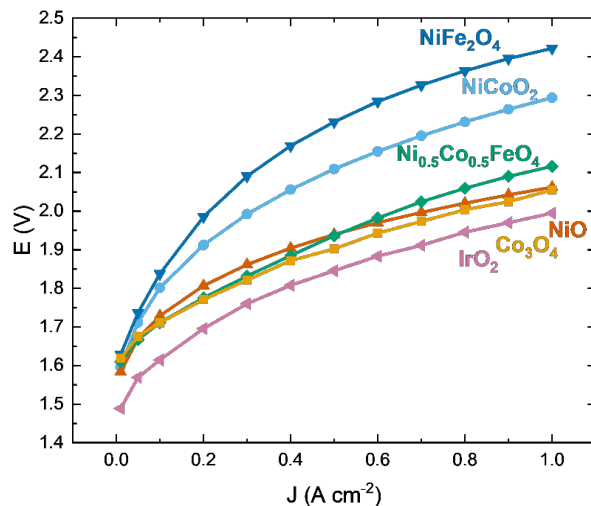
Figure B.3. Polarization curves for all catalysts in pure-water AEMWE **with** *iR*-correction. GEIS was collected at 50 mA cm^{-2} and R_u was obtained from the total high-frequency impedance at 500 kHz.
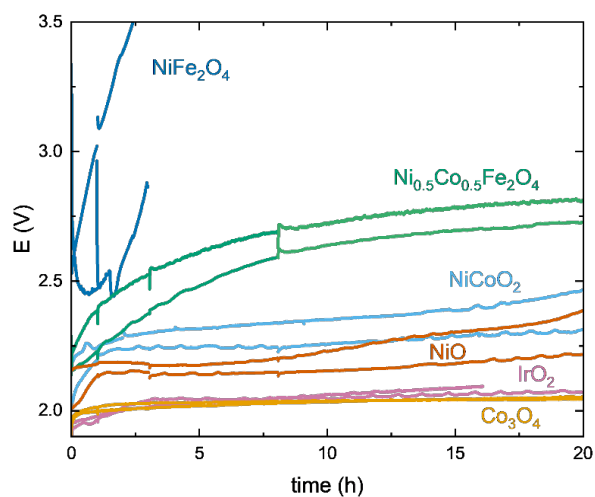
Figure B.4. Duplicate durability runs for each catalyst tested.
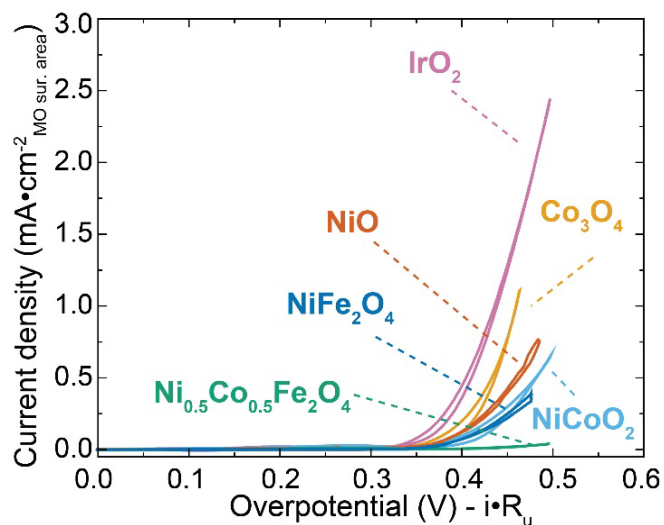
Figure B.5. Replicate data for CV testing on QCM. For IrO_2, NiO, and $Ni_{0.5}Co_{0.5}Fe_2O_4$ catalysts sample size $n = 3$. Due to a stir-bar malfunction, mechanical stirring was not conducted for one sample of the Co_3O_4, $NiCoO_2$, and $NiFe_2O_4$ catalysts, therefore sample size $n = 2$ was used. Data is presented as average ± one standard deviation. Samples averaged are independent of the sample shown in Figure 1d.
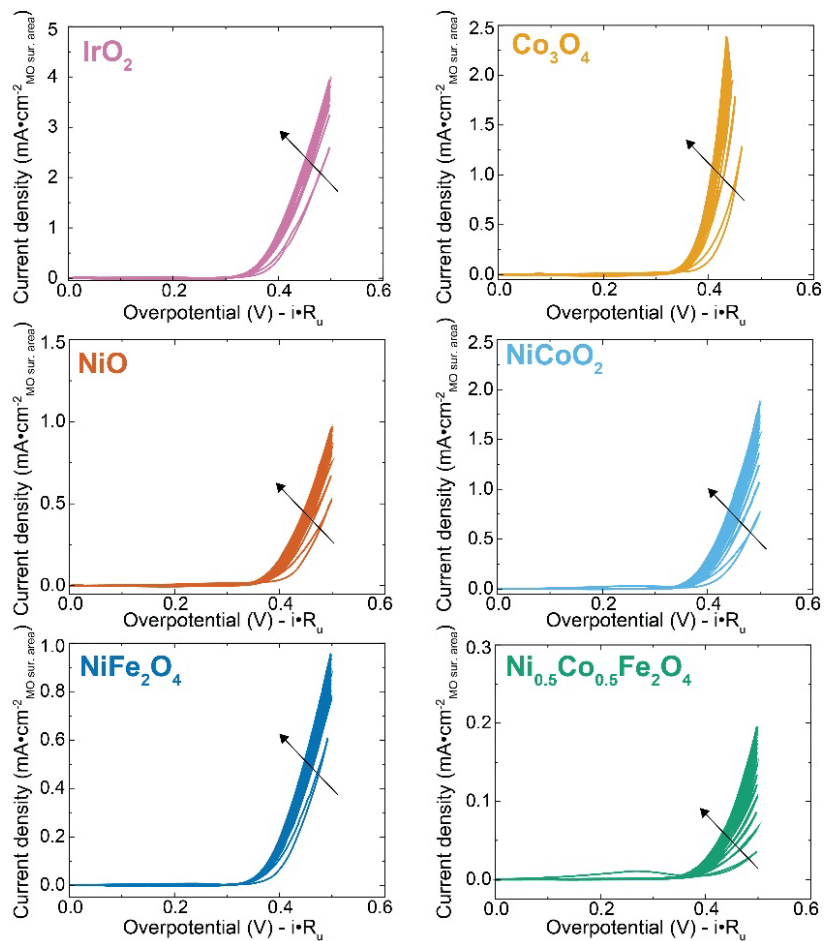
Figure B.6. Catalyst activation in KOH. Catalyst films on QCM crystals were cycled for 20 CV sweeps. Activity improves with cycling for all catalysts. The activation phenomena are certainly different in the MEA, so the first cycle data is shown in the main manuscript.
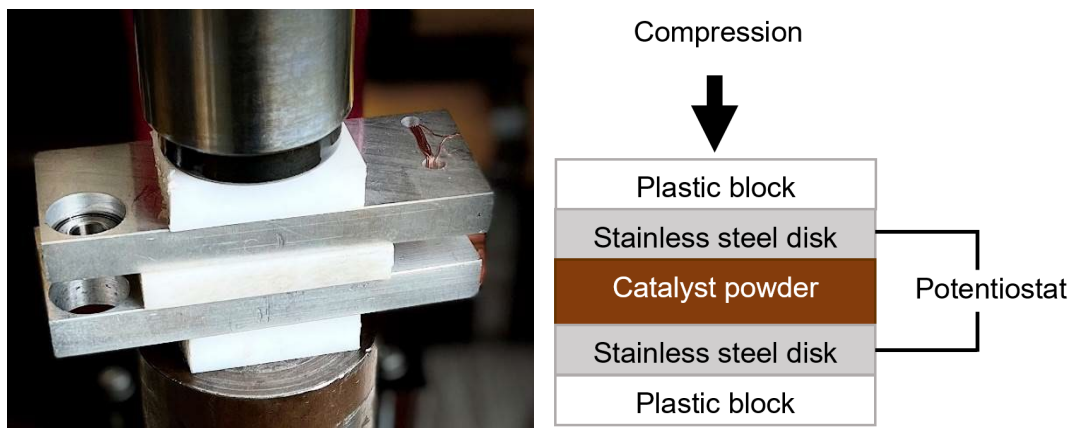
Figure B.7. Conductivity measurement experimental setup.
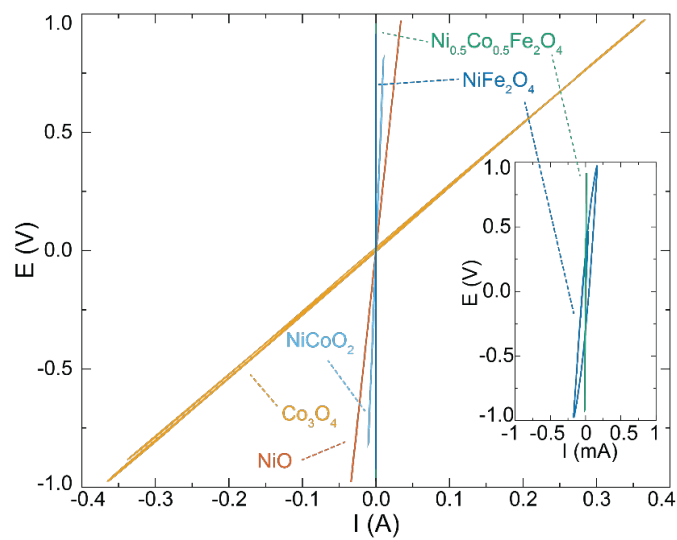
Figure B.8. Polarization curves of the measured catalyst powders from which conductivity data is extracted.
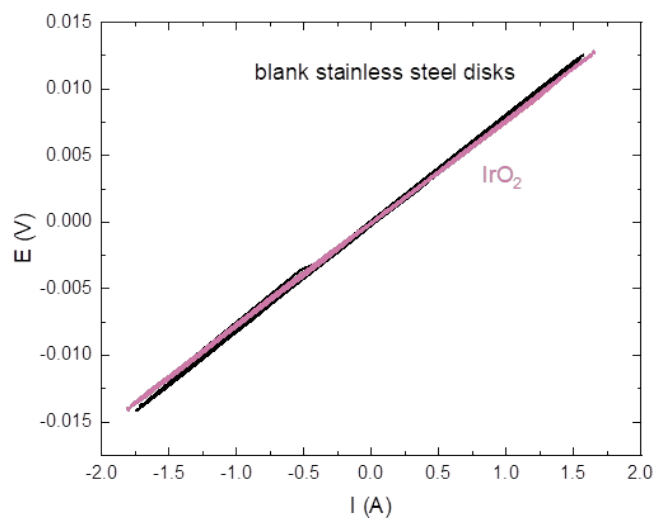
Figure B.9. Conductivity measurement of IrO_2 compared to the contact resistance measured between the two stainless steel disks.
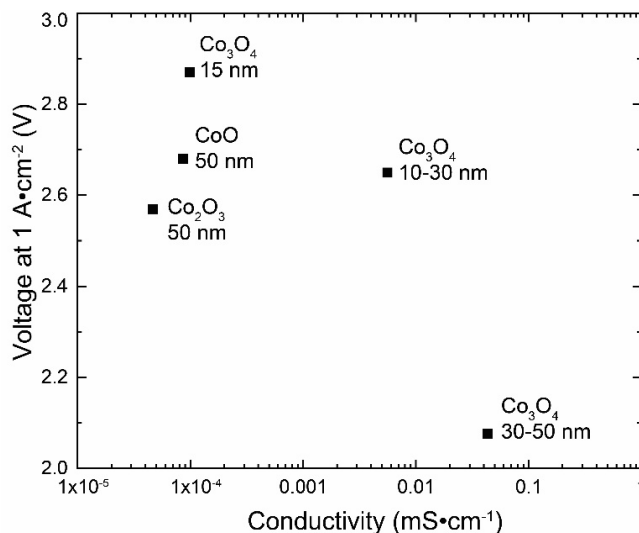
Figure B.10. Effect of catalyst layer conductivity on voltage performance for various Co-based anode catalysts. The indicated catalyst was sprayed in an ink with ionomer onto a glass slide and dried at 80 °C. Note the conductivity here is significantly lower than that in Figure 3.2. The conductivity here is a measurement of the uncompressed catalyst layer sprayed onto a glass slide, while the conductivity measurements in Figure 3.2 are of the catalyst powder only.
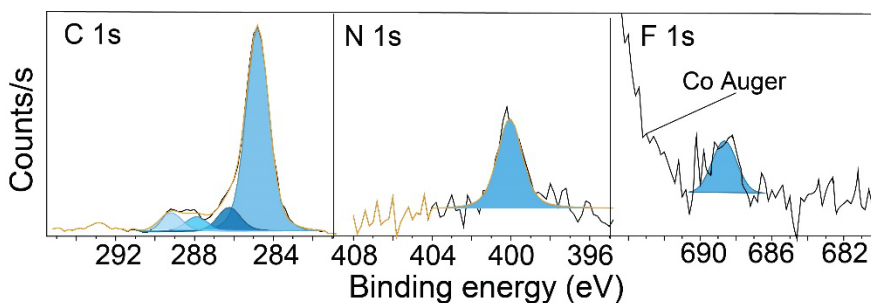
Figure B.11. XP Spectra of a Co_3O_4 anode operated in a pure-water AEMWE for 57 h. The N 1s peak is still resolved at 57 h but gone by 250 h, while the F 1s peak is barely present for the sample analyzed at 57 h and a bit better resolved for the sample operated for 250 h. We do not interpret this trend to represent different degradation products present at each time point, but rather highlighting the variable and uncontrolled nature in which the ionomer degrades. From these findings we can only conclude that the ionomer is oxidizing during operation with Co_3O_4 and do not make any claims regarding the mechanism or degradation products.
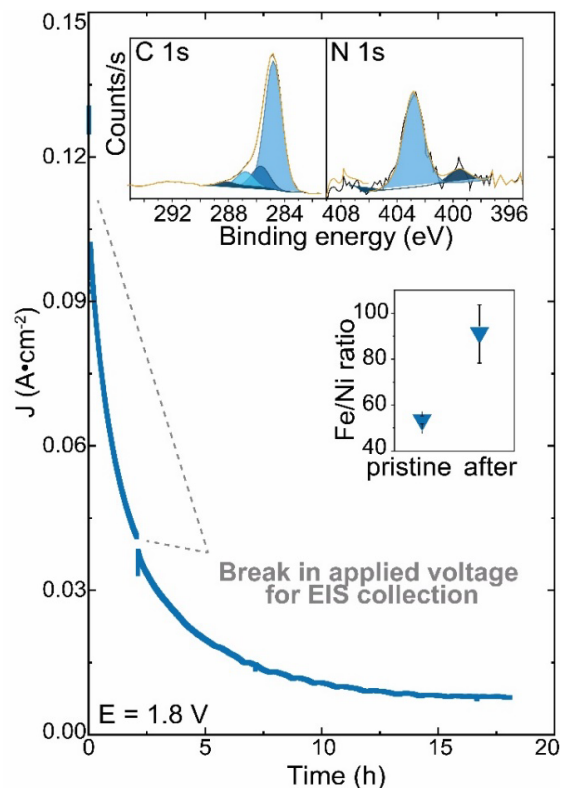
Figure B.12. Chronoamperometric durability testing of NiFe$_2$O$_4$ catalyst. NiFe$_2$O$_4$ was operated at 1.8 V with pure water at 57 °C. A stainless steel woven substrate was used as the anode GDL and Pt Black catalyst on Toray carbon paper was used as the cathode. The Fe/Ni ratio increases from 0.54 ± 0.20 to 0.91 ± 0.11 following the trend observed for the 20-hour electrolyzer run held at 500 mA cm^2 where the Fe/Ni ratio increased to 1.1 ± 0.1 (Figure 3.5a).
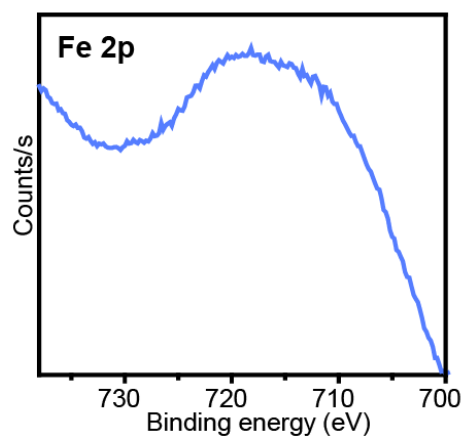
Figure B.13. Fe XPS data of the cathode GDL surface post Fe-spike experiment. No Fe is detected indicating the observed degradation is not due to Fe crossing the membrane to the cathode (consistent with the negative charge expected for soluble Fe species in alkaline conditions).

136
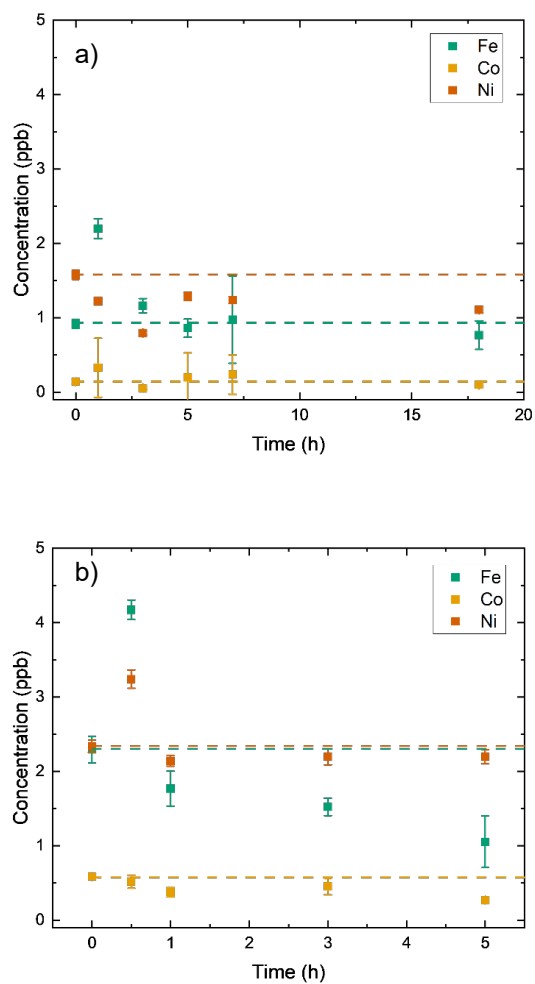
Figure B.14. Metal concentration in anode water effluent as determined by ICP-MS for a) Co_3O_4 and b) $Ni_{0.5}Co_{0.5}Fe_2O_4$ anode catalysts. The data point at $t = 0$ and dashed line shows the metal concentration in the water source feeding the inlet. The $Ni_{0.5}Co_{0.5}Fe_2O_4$ system was only sampled for 5 h because shortly after the cell was shut down due to the voltage exceeding 5 V (indicative of the formation of a highly resistive interface). For each catalyst sample size $n = 1$; five replicate scans were conducted per sample. Data is presented as mean ± one standard deviation.

137

APPENDIX C

CHAPTER IV SUPPLEMENTAL INFORMATION

Supplemental Materials and Methods

PNB ionomer conductivity, ion exchange capacity (IEC), and water uptake (WU). Conductivity was measured by four-probe electrochemical impedance spectroscopy (EIS) using a Scribner Membrane Conductivity Clamp and a Bio-Logic SP-150 Potentiostat as in our prior reports. [1-3] IEC was measured using standard back-titration methods and carried out according to our prior reports. [1-3] The material was in the Cl^- form after IEC analysis, and all manipulations for membrane electrode assembly fabrication were carried out on the membrane with a Cl^- counterion. Water uptake was determined using the following equation:

$$WU\ (\%) = \frac{Mw - Md}{Md} \times 100$$

Where Mw = mass of hydrated film in ^-OH form and Md = mass of the dry film in the Cl^- form.

Detailed description of electrolyzer assembly with integrated reference electrode. As described in the main body text, a reference electrode is integrated in the MEA by extending a strip of membrane outside the electrolyzer hardware and attaching a Hg/HgO reference electrode submerged in KOH. For assembly, the anode PTE is placed on the anode flow field with the appropriate number of gaskets (Figure C.3). Next, a support gasket is added and the membrane strip is placed across the flow field so the edge is touching the edge of the anode PTE (Figure C.4). The gasket under the membrane strip has a tab that extends outside the electrolyzer hardware to support the membrane strip

and isolate the strip from contacting the flow field (Figure C.5). Then, a thinner gasket is placed on top of the membrane strip (Figure C.6). This gasket has a slit cut in the tab to act as a water channel and help maintain water flow to the membrane strip (Figure C.7). After, the HEM is placed on top of the anode PTE, overlapping with the membrane strip (Figure C.8). Another isolation gasket (Figure C.5) is placed on top of the stack to keep the strip from touching the cathode flow field (Figure C.9). The cathode PTE is then placed on top of the AEM and stacked with the remaining gaskets (Figure C.10). Schematics of the regular and reference electrode MEAs are shown in Figure C.11.
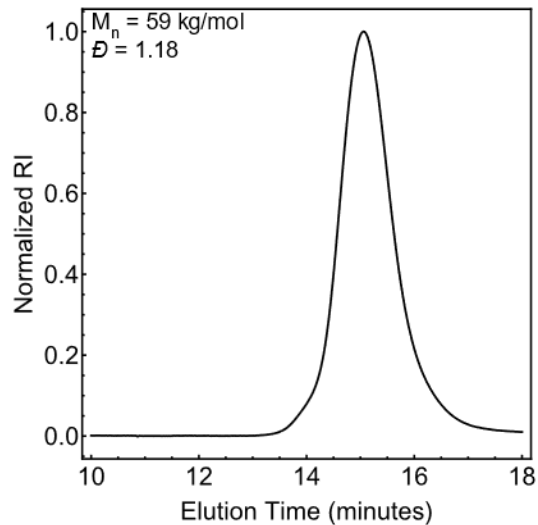
Figure C.1. GPC trace of 60:40 NB-5-Hex-co-NB-5-BuBr copolymer.

NB-5-Hex-*co*-NB-5-BuBr (60:40) in CDCl₃

$$\text{Percent NB-5-BuBr} = \frac{1}{1 + \dfrac{4.76}{3}} = 38.7\%$$

NB-5-Hex-*co*-NMe3 [Br] (60:40) in CDCl₃ and CD₃OD
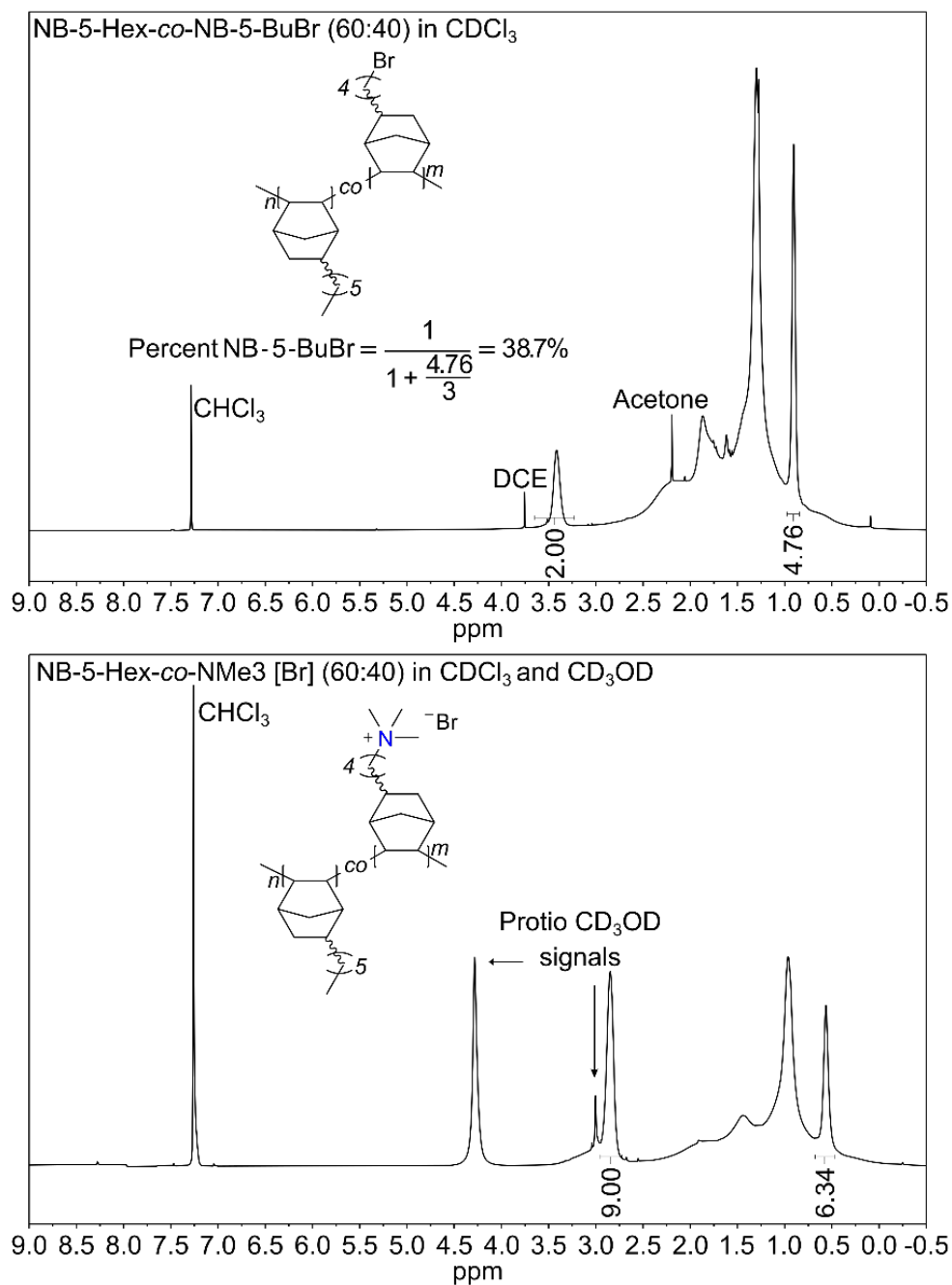
Figure C.2. ¹H NMR spectra (500 MHz) of DP 500 60:40 NB-5-Hex-co-NB-5-BuBr copolymer before (Top) and after (Bottom) NMe₃ substitution, collected in 1:1 CDCl₃:CD₃OD. A 9:4.5 ratio should be observed for the N-methyl groups of the trimethylammonium to the terminal methyl group from the hexyl chain of the NB-5-Hex for a 40 mol% ionic copolymer.

Table C.1. Membrane properties for the hydroxide exchange polymers used in this study.

	Water uptake (%)	$\sigma_{22\,°C}$ OH⁻ (mS/cm)	Ion exchange capacity (mmol/g)	λ
60:40 NB-5-Hex-*co*-NMe₃	88	45 ± 3	1.91	26
PiperION TP-85[4]	46	80 ± 5	2.30-2.37	N/A
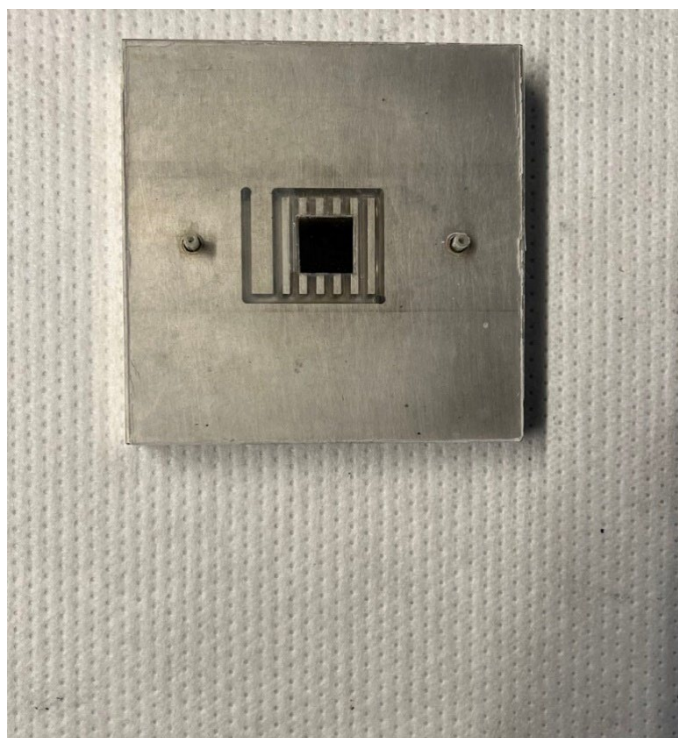
Figure C.3. Anode PTE on the anode flow field.
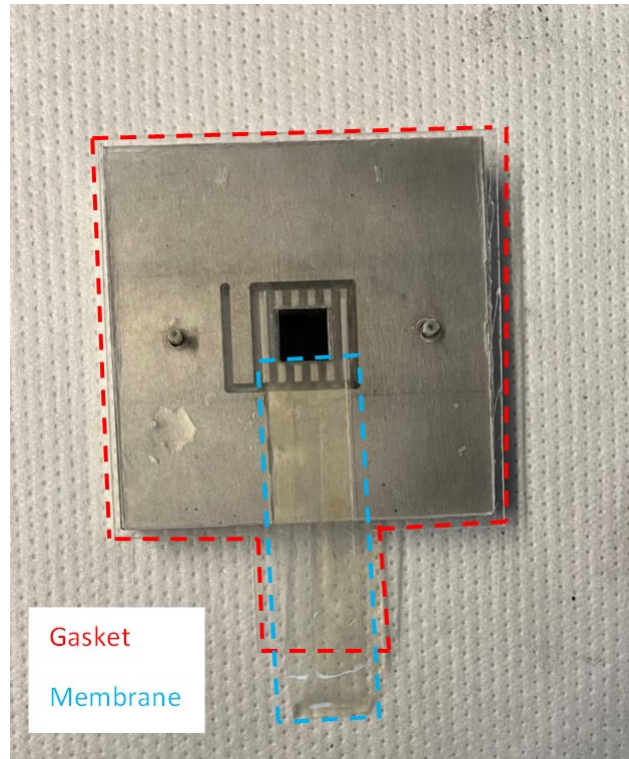
Figure C.4. Membrane strip placed on the support gasket and aligned at the edge of the anode PTE.
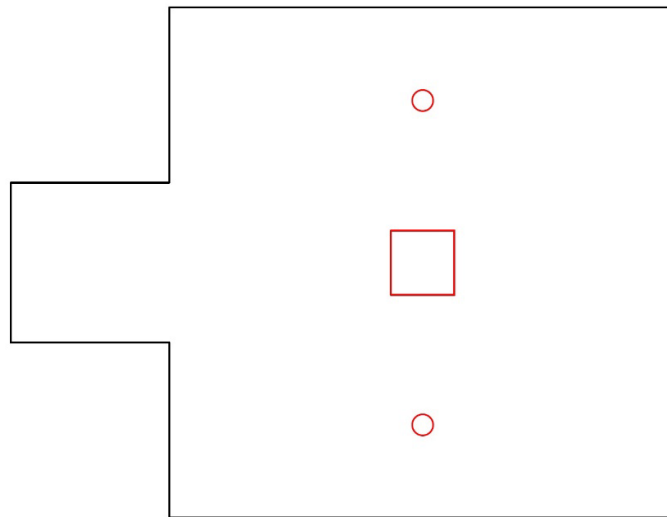
Figure C.5. Shape of gasket used under and above the membrane strip.
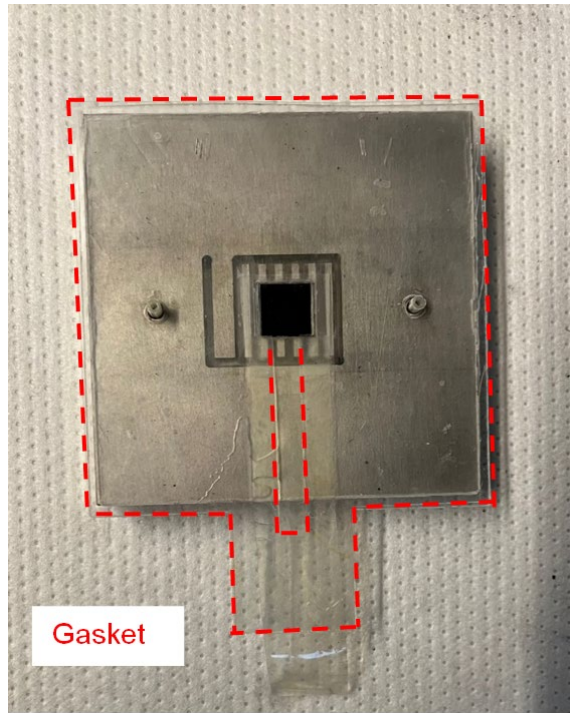
Figure C.6. Gasket with water channel placed on top of membrane strip.
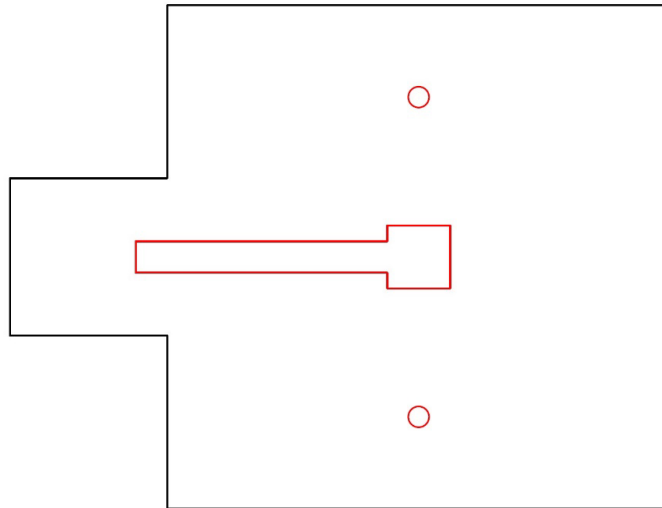
Figure C.7. Shape of gasket with water channel.
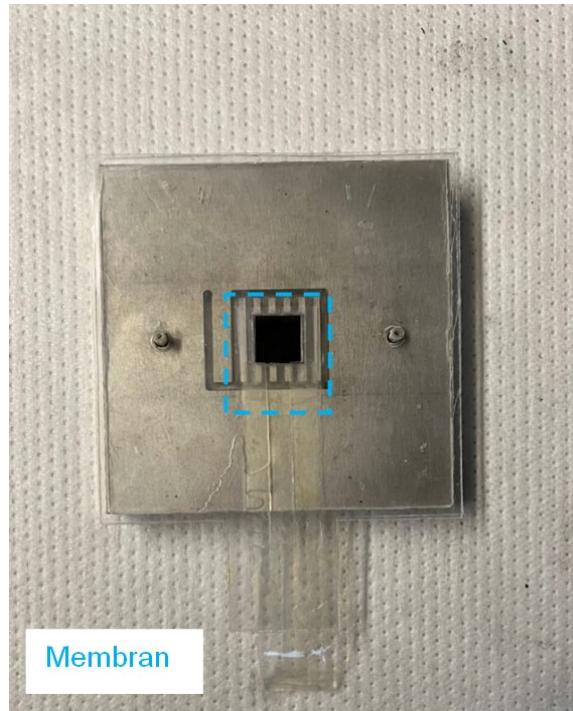
Figure C.8. AEM placed on top of the anode PTE. The AEM is cut wide enough to overlap with the membrane strip past the outer edge of the serpentine pattern.
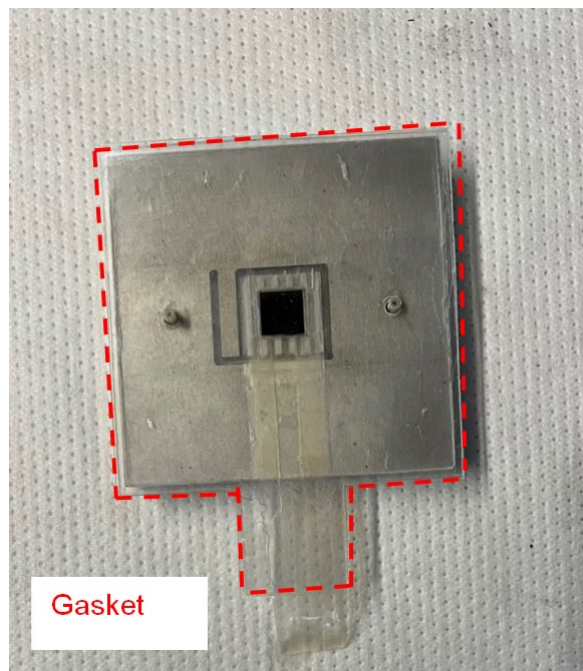
Figure C.9. Another isolation gasket is placed on top of the stack.

Figure C.10. Cathode PTE placed on top of the AEM, completing the MEA.
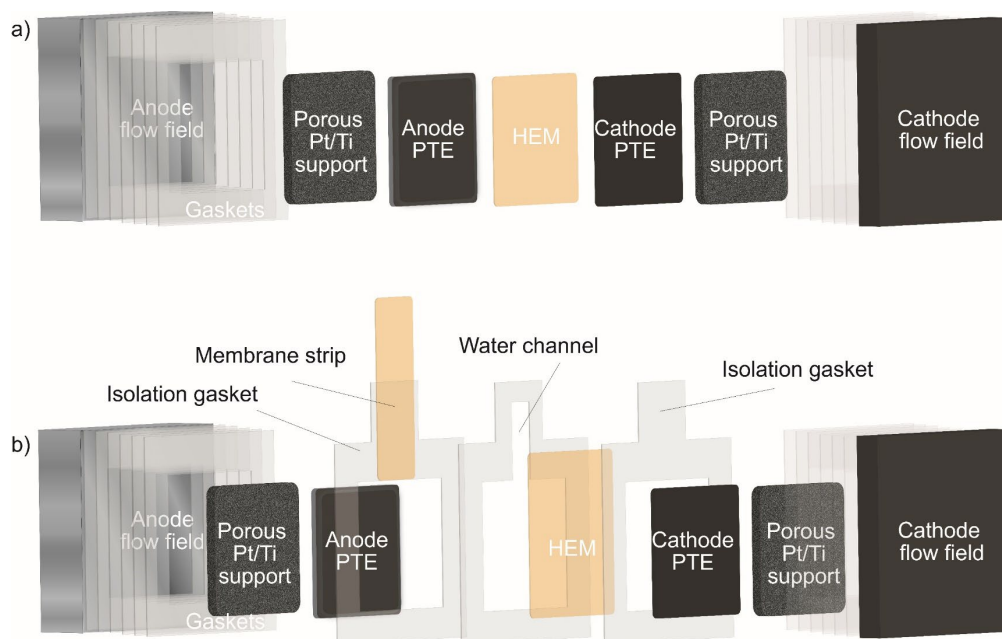
Figure C.11. Schematic of MEA components. a) standard MEA and b) MEA with integrated reference electrode. The membrane used was the PiperION TP-85 and cathode catalyst layer Pt black with TP-85 ionomer for all AEM studies.
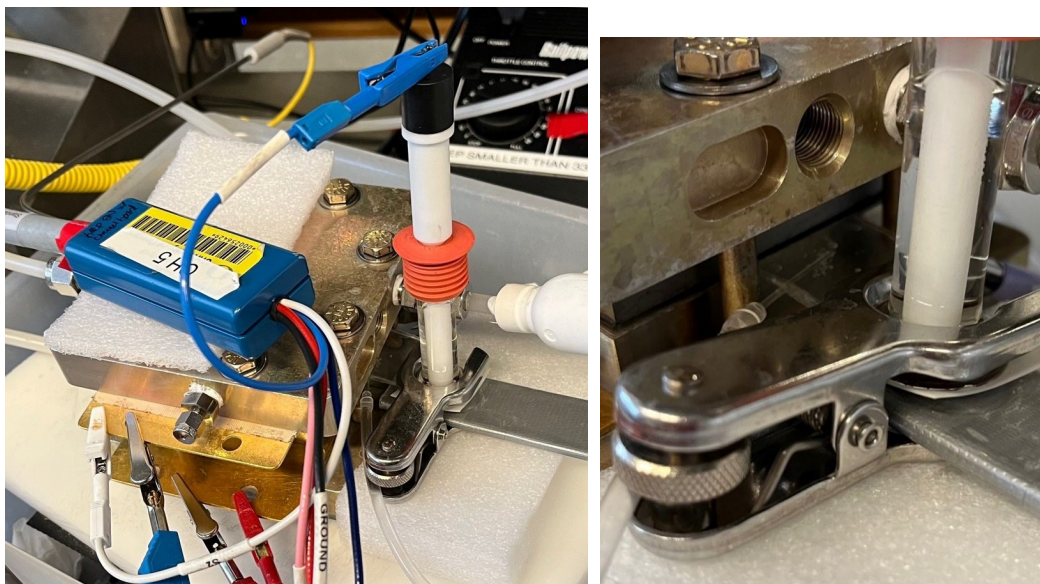
Figure C.12. Photos of electrolyzer hardware with reference electrode and close-up of strip with gaskets isolating contact with the flow fields. A water drip is clamped between the membrane strip gaskets to keep the membrane hydrated. A Schlenk line adapter is clamped to the membrane strip and filled with 0.1 M KOH. The Hg/HgO reference electrode is submerged in electrolyte.
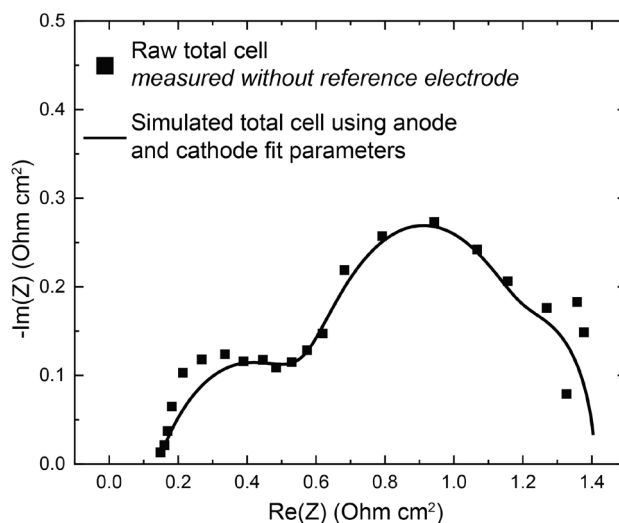
Figure C.13. Comparison of total cell impedance with and without reference electrode. The fit parameters obtained from the anode and cathode Nyquist plots were used to simulate the total cell impedance (line). The data agrees well with the raw total cell impedance measured without the reference electrode (points). Error in the high frequency region is due to high error from the anode signal, as the anode cannot be resolved above ~600 Hz due to a potentiostat limitaion. *This data demonstrates the accuracy of the refence cell impdeance in separating the individual electrode impedances.*
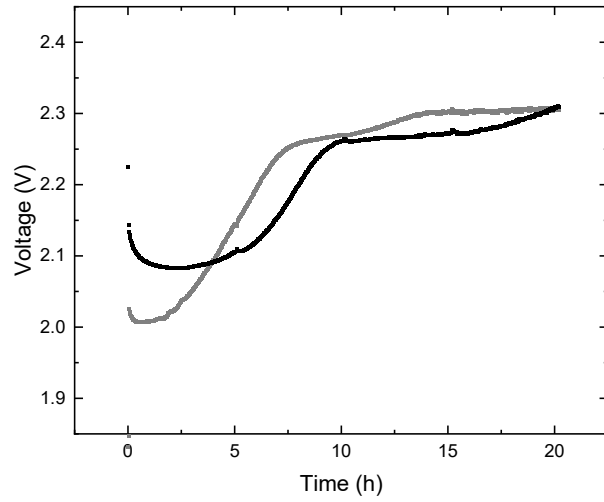
Figure C.14. Comparison of AEM operation with 10% anode ionomer content (gray) and 20% anode ionomer content (black).
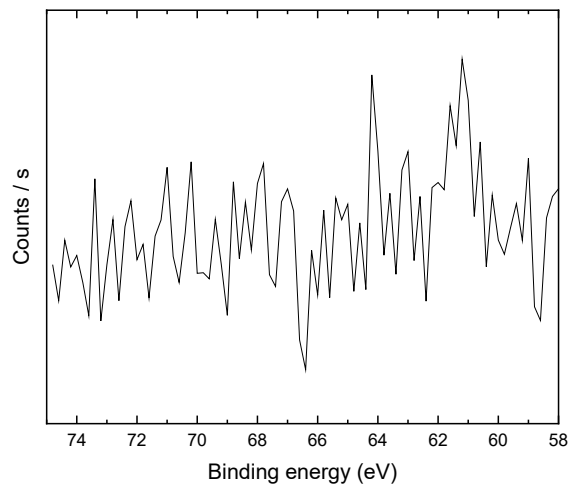
Figure C.15. Ir 4f XPS region of a pristine TP-85 anode. Ir signal is blocked by the top ionomer coating.
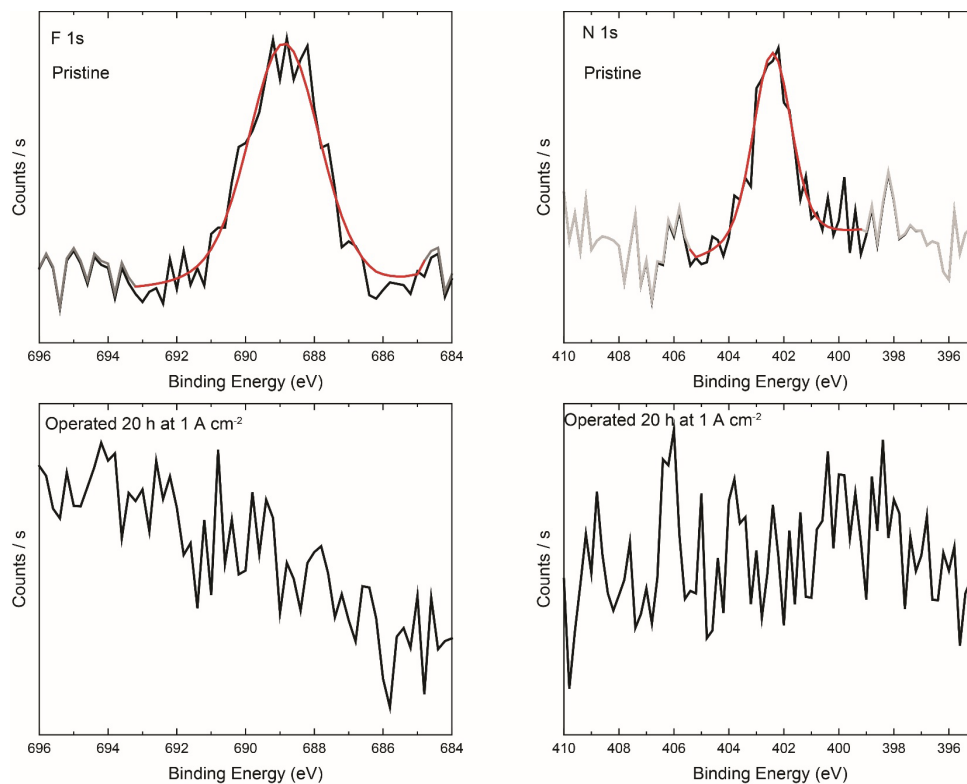
Figure C.16. F 1s and N 1s XP spectra of pristine TP-85 anode PTE (top) and PTE after operated (bottom). All F and N content is no longer resolved.
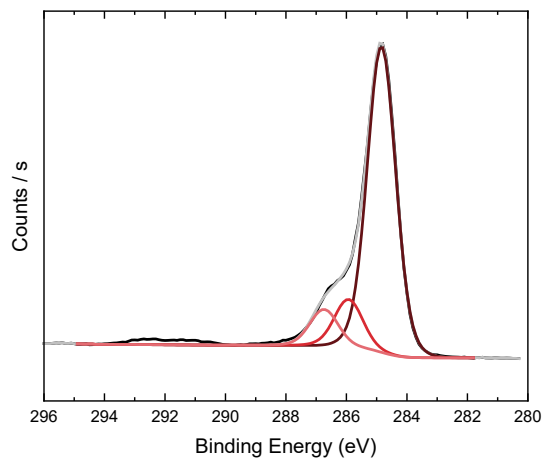
Figure C.17. C 1s XPS of an IrO_x/TP-85 anode PTE after assembled in a device and operated with only water flow (no applied current/voltage) for 24 h.
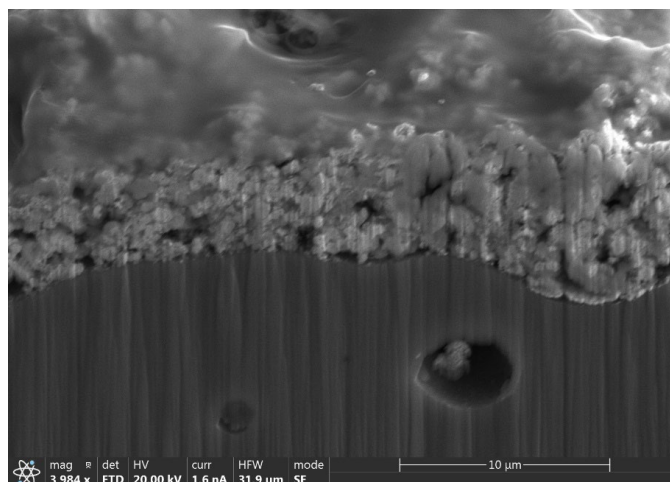
Figure C.18. Cross section of an IrO_x/TP-85 anode PTE after assembled in a device and exposed to water flow at 70 °C (no applied current) for 24 h. The top ionomer layer and ionomer network throughout the catalyst layer are still intact.
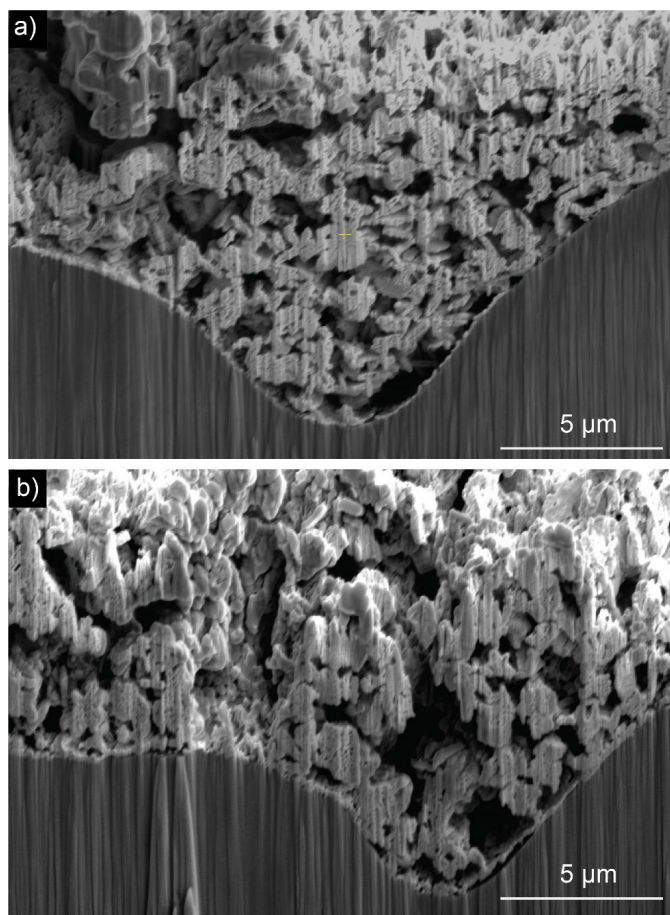
Fig. C.19. Cross section of an IrO_x/Nafion anode after operation with a) PEM and b) HEM.

REFERENCES CITED

Chapter I

1.   Hydrogen Council *Path to Hydrogen Competitiveness: A Cost Perspecitve*; 20 January, 2020.

2.   Hydrogen Europe. Hydrogen Applications. https://hydrogeneurope.eu/hydrogen-applications (accessed Jan 7).

3.   van Renssen, S. The Hydrogen Solution? *Nat. Clim. Change.* **2020,** *10* (9), 799-801.

4.   de Coninck, H.; Revi, A.; Babiker, M.; Bertoldi, P.; Buckeridge, M.; Cargtwright, A.; Dong, W.; Ford, J.; Fuss, S.; Hourcade, J.-C.; Ley, D.; Mechler, R.; Newman, P.; Revokatova, A.; Shchultz, S.; Steg, L.; Sugiyama, T., Strengthening and Implementing the Global Response. In *Global Warming of 1.5°C. An IPCC Special Report on the Impacts of Global Warming of 1.5°C above Pre-Industrial Levels and Related Global Greenhouse Gas Emission Pathways, in the Context of Strengthening the Global Response to the Threat of Climate Change, Sustainable Development, and Efforts to Eradicate Poverty*, 2018.

5.   IEA *The Future of Hydrogen*; International Energy Alliance: Paris, 2019.

6.   IEA *Technology Roadmap - Hydrogen and Fuel Cells*; International Energy Alliance: Paris, 2015.

7.   Bender, G. *Scalable Electrolytic Systems for Renewable Hydrogen Production: Cooperative Research and Development Final Report, Crada Number Crd-18-747*; NREL/TP-5900-76136 United States 10.2172/1601587 NREL English; ; National Renewable Energy Lab. (NREL), Golden, CO (United States): 2020; p Medium: ED; Size: 7.4 MB.

8.   IRENA *Green Hydrogen Cost Reduction: Scaling up Electrolysers to Meet the 1.5ºC Climate Goal*; International Renewable Energy Agency: 2020.

9.   Pivovar, B.; Rustagi, N.; Satyapal, S. Hydrogen at Scale (H2@Scale): Key to a Clean, Economic, and Sustainable Energy System. *Electrochem. Soc. Interface* **2018,** *27* (1), 47-52.

10.   Ayers, K. Gigawatt-Scale Renewable Hydrogen Via Water Splitting as a Case Study for Collaboration: The Need to Connect Fundamental and Applied Research to Accelerate Solutions. *MRS Energy Sustain.* **2017,** *4*, E11.

11.   Ayers, K.; Danilovic, N.; Ouimet, R.; Carmo, M.; Pivovar, B.; Bornstein, M. Perspectives on Low-Temperature Electrolysis and Potential for Renewable Hydrogen at Scale. *Annu. Rev. Chem. Biomol. Eng.* **2019,** *10* (1), 219-239.

12.   Zeng, K.; Zhang, D. Recent Progress in Alkaline Water Electrolysis for Hydrogen Production and Applications. *Prog. Energy Combust. Sci.* **2010,** *36* (3), 307-326.

13.   Nel Hydrogen M Series Proton Pem Electrolyzer.
        https://nelhydrogen.com/product/m-series-3/ (accessed April 2).

14.   Plug Power Plug Lands 1 Gw Electrolyzer Order with H2 Energy Europe.
        https://www.ir.plugpower.com/press-releases/news-details/2022/Plug-Lands-1-
        GW-Electrolyzer-Order-with-H2-Energy-Europe/default.aspx (accessed March
        29).

15.   Nel Hydrogen Nel Asa: Official Opening of the Herøya Facility.
        https://nelhydrogen.com/press-release/nel-asa-official-opening-of-the-heroya-
        facility/ (accessed March 29).

16.   Cummins Inc. Cummins Drives Domestic Green Hydrogen Economy Forward
        with First U.S. Electrolyzer Manufacturing Facility.
        https://www.cummins.com/news/releases/2022/10/10/cummins-drives-domestic-
        green-hydrogen-economy-forward-first-us (accessed March 29).

17.   Sumner, J. J.; Creager, S. E.; Ma, J. J.; DesMarteau, D. D. Proton Conductivity in
        Nafion® 117 and in a Novel Bis[(Perfluoroalkyl)Sulfonyl]Imide Ionomer
        Membrane. *J. Electrochem. Soc.* **1998,** *145* (1), 107.

18.   Sone, Y.; Ekdunge, P.; Simonsson, D. Proton Conductivity of Nafion 117 as
        Measured by a Four-Electrode Ac Impedance Method. *J. Electrochem. Soc.* **1996,**
        143 (4), 1254.

19.   Carmo, M.; Fritz, D. L.; Mergel, J.; Stolten, D. A Comprehensive Review on Pem
        Water Electrolysis. *Int. J. Hydrogen Energy* **2013,** *38* (12), 4901-4934.

20.   Millet, P.; Ngameni, R.; Grigoriev, S. A.; Fateev, V. N. Scientific and Engineering
        Issues Related to Pem Technology: Water Electrolysers, Fuel Cells and Unitized
        Regenerative Systems. *Int. J. Hydrogen Energy* **2011,** *36* (6), 4156-4163.

21.   Hemauer, J.; Rehfeldt, S.; Klein, H.; Peschel, A. Performance and Cost Modelling
        Taking into Account the Uncertainties and Sensitivities of Current and Next-
        Generation Pem Water Electrolysis Technology. *Int. J. Hydrogen Energy* **2023,**
        Available online April 6, 2023.

22.   Li, D.; Motz, A. R.; Bae, C.; Fujimoto, C.; Yang, G.; Zhang, F.-Y.; Ayers, K. E.;
        Kim, Y. S. Durability of Anion Exchange Membrane Water Electrolyzers. *Energy
        Environ. Sci.* **2021,** *14* (6), 3393-3419.

23.   Fan, J.; Willdorf-Cohen, S.; Schibli, E. M.; Paula, Z.; Li, W.; Skalski, T. J. G.;
        Sergeenko, A. T.; Hohenadel, A.; Frisken, B. J.; Magliocca, E.; Mustain, W. E.;
        Diesendruck, C. E.; Dekel, D. R.; Holdcroft, S. Poly(Bis-Arylimidaziums)
        Possessing High Hydroxide Ion Exchange Capacity and High Alkaline Stability.
        Nat. Commun. **2019,** *10* (1), 2306.

24.   Huang, G.; Mandal, M.; Hassan, N. U.; Groenhout, K.; Dobbs, A.; Mustain, W.
        E.; Kohl, P. A. Ionomer Optimization for Water Uptake and Swelling in Anion
        Exchange Membrane Electrolyzer: Oxygen Evolution Electrode. *J. Electrochem.
        Soc.* **2020,** *167* (16), 164514.

151

25.   Huang, G.; Mandal, M.; Hassan, N. U.; Groenhout, K.; Dobbs, A.; Mustain, W. E.; Kohl, P. A. Ionomer Optimization for Water Uptake and Swelling in Anion Exchange Membrane Electrolyzer: Hydrogen Evolution Electrode. *J. Electrochem. Soc.* **2021,** *168* (2), 024503.

26.   Chen, Y.; Su, D.; Chen, Y.; Zhu, Z.; Li, W. Three-Phase Interface-Assisted Advanced Electrochemistry-Related Applications. *Cell Rep. Phys. Sci.* **2021,** *2* (10), 100602.

27.   Faid, A. Y.; Xie, L.; Barnett, A. O.; Seland, F.; Kirk, D.; Sunde, S. Effect of Anion Exchange Ionomer Content on Electrode Performance in Aem Water Electrolysis. *Int. J. Hydrogen Energy* **2020,** *45* (53), 28272-28284.

28.   Alia, S. M.; Reeves, K. S.; Baxter, J. S.; Cullen, D. A. The Impact of Ink and Spray Variables on Catalyst Layer Properties, Electrolyzer Performance, and Electrolyzer Durability. *J. Electrochem. Soc.* **2020,** *167* (14), 144512.

29.   Lindquist, G. A.; Oener, S. Z.; Krivina, R.; Motz, A. R.; Keane, A.; Capuano, C.; Ayers, K. E.; Boettcher, S. W. Performance and Durability of Pure-Water-Fed Anion Exchange Membrane Electrolyzers Using Baseline Materials and Operation. *ACS Appl. Mater. Interfaces* **2021,** *13* (44), 51917-51924.

30.   Bernt, M.; Gasteiger, H. A. Influence of ionomer content in IrO_2/TiO_2 electrodes on pem water electrolyzer performance. *J. Electrochem. Soc.* **2016,** *163* (11), F3179-F3189.

Chapter II

1.   Henkensmeier, D.; Najibah, M.; Harms, C.; Žitka, J.; Hnát, J.; Bouzek, K. Overview: State-of-the Art Commercial Membranes for Anion Exchange Membrane Water Electrolysis. *J. Electrochem. Energy.* **2020,** *18* (2), 024001-0240018.

2.   Vincent, I.; Bessarabov, D. Low Cost Hydrogen Production by Anion Exchange Membrane Electrolysis: A Review. *Renew. Sust. Energ. Rev.* **2018,** *81*, 1690-1704.

3.   Miller, H. A.; Bouzek, K.; Hnat, J.; Loos, S.; Bernäcker, C. I.; Weißgärber, T.; Röntzsch, L.; Meier-Haack, J. Green Hydrogen from Anion Exchange Membrane Water Electrolysis: A Review of Recent Developments in Critical Materials and Operating Conditions. *Sustain. Energ. Fuels.* **2020,** *4* (5), 2114-2133.

4.   Leng, Y.; Chen, G.; Mendoza, A. J.; Tighe, T. B.; Hickner, M. A.; Wang, C.-Y. Solid-State Water Electrolysis with an Alkaline Membrane. *J. Am. Chem. Soc.* **2012,** *134* (22), 9054-9057.

5.   Li, D.; Park Eun, J.; Zhu, W.; Shi, Q.; Zhou, Y.; Tian, H.; Lin, Y.; Serov, A.; Zulevi, B.; Baca Ehren, D.; Fujimoto, C.; Chung Hoon, T.; Kim Yu, S. Highly Quaternized Polystyrene Ionomers for High Performance Anion Exchange Membrane Water Electrolysers. *Nat. Energ.* **2020,** *5*, 378-385.

6.   Soni, R.; Miyanishi, S.; Kuroki, H.; Yamaguchi, T. Pure Water Solid Alkaline Water Electrolyzer Using Fully Aromatic and High-Molecular-Weight Poly(Fluorene-Alt-Tetrafluorophenylene)-Trimethyl Ammonium Anion Exchange Membranes and Ionomers. *ACS Appl. Energy Mater.* **2020,** *4* (2), 1053-1058.

7.   Xiao, J.; Oliveira, A. M.; Wang, L.; Zhao, Y.; Wang, T.; Wang, J.; Setzler, B. P.; Yan, Y. Water-Fed Hydroxide Exchange Membrane Electrolyzer Enabled by a Fluoride-Incorporated Nickel–Iron Oxyhydroxide Oxygen Evolution Electrode. *ACS Catal.* **2021,** *11* (1), 264-270.

8.   Carmo, M.; Fritz, D. L.; Mergel, J.; Stolten, D. A Comprehensive Review on Pem Water Electrolysis. *Int. J. Hydrogen Energy* **2013,** *38* (12), 4901-4934.

9.   Mayerhöfer, B.; McLaughlin, D.; Böhm, T.; Hegelheimer, M.; Seeberger, D.; Thiele, S. Bipolar Membrane Electrode Assemblies for Water Electrolysis. *ACS Appl. Energy Mater.* **2020,** *3* (10), 9635-9644.

10.   Oener, S. Z.; Foster, M. J.; Boettcher, S. W. Accelerating Water Dissociation in Bipolar Membranes and for Electrocatalysis. *Science* **2020,** *369* (6507), 1099.

11.   Oener, S. Z.; Twight, L. P.; Lindquist, G. A.; Boettcher, S. W. Thin Cation-Exchange Layers Enable High-Current-Density Bipolar Membrane Electrolyzers Via Improved Water Transport. *ACS Energy Lett.* **2021,** *6* (1), 1-8.

12.   Jhong, H.-R. M.; Brushett, F. R.; Kenis, P. J. A. The Effects of Catalyst Layer Deposition Methodology on Electrode Performance. *Adv. Energy Mater.* **2013,** *3* (5), 589-599.

13.   Lim, A.; Kim, H.-j.; Henkensmeier, D.; Jong Yoo, S.; Young Kim, J.; Young Lee, S.; Sung, Y.-E.; Jang, J. H.; Park, H. S. A Study on Electrode Fabrication and Operation Variables Affecting the Performance of Anion Exchange Membrane Water Electrolysis. *J. Ind. Eng. Chem.* **2019,** *76*, 410-418.

14.   Schuler, T.; Ciccone, J. M.; Krentscher, B.; Marone, F.; Peter, C.; Schmidt, T. J.; Büchi, F. N. Hierarchically Structured Porous Transport Layers for Polymer Electrolyte Water Electrolysis. *Adv. Energy Mater.* **2020,** *10* (2), 1903216.

15.   Lettenmeier, P.; Kolb, S.; Sata, N.; Fallisch, A.; Zielke, L.; Thiele, S.; Gago, A. S.; Friedrich, K. A. Comprehensive Investigation of Novel Pore-Graded Gas Diffusion Layers for High-Performance and Cost-Effective Proton Exchange Membrane Electrolyzers. *Energy Environ. Sci.* **2017,** *10* (12), 2521-2533.

16.   Suermann, M.; Gimpel, T.; Bühre, L. V.; Schade, W.; Bensmann, B.; Hanke-Rauschenbach, R. Femtosecond Laser-Induced Surface Structuring of the Porous Transport Layers in Proton Exchange Membrane Water Electrolysis. *J. Mater. Chem. A.* **2020,** *8* (9), 4898-4910.

17.   Ionomr. Ionomer Hydrogen Info Sheet. https://ionomr.com/wp-content/uploads/2018/12/Ionomr-Hydrogen-Info-Sheet.pdf (accessed September 15).

18.   Materials, D. Sustainion Anion Exchange Membranes. https://dioxidematerials.com/technology/sustainion-membranes/ (accessed February 2).

19.   Wang, J.; Zhao, Y.; Setzler, B. P.; Rojas-Carbonell, S.; Ben Yehuda, C.; Amel, A.; Page, M.; Wang, L.; Hu, K.; Shi, L.; Gottesfeld, S.; Xu, B.; Yan, Y. Poly(Aryl Piperidinium) Membranes and Ionomers for Hydroxide Exchange Membrane Fuel Cells. *Nat. Energ.* **2019,** *4* (5), 392-398.

20.   Li, D.; Motz, A. R.; Bae, C.; Fujimoto, C.; Yang, G.; Zhang, F.-Y.; Ayers, K. E.; Kim, Y. S. Durability of Anion Exchange Membrane Water Electrolyzers. *Energy Environ. Sci.* **2021,** *14* (6), 3393-3419.

21.   Epsztein, R.; Shaulsky, E.; Qin, M.; Elimelech, M. Activation Behavior for Ion Permeation in Ion-Exchange Membranes: Role of Ion Dehydration in Selective Transport. *J. Membr. Sci.* **2019,** *580*, 316-326.

22.   Xu, Q.; Oener, S. Z.; Lindquist, G.; Jiang, H.; Li, C.; Boettcher, S. W. Integrated Reference Electrodes in Anion-Exchange-Membrane Electrolyzers: Impact of Stainless-Steel Gas-Diffusion Layers and Internal Mechanical Pressure. *ACS Energy Lett.* **2020,** *6* (2), 305-312.

23.   Bock, R.; Karoliussen, H.; Seland, F.; Pollet, B. G.; Thomassen, M. S.; Holdcroft, S.; Burheim, O. S. Measuring the Thermal Conductivity of Membrane and Porous Transport Layer in Proton and Anion Exchange Membrane Water Electrolyzers for Temperature Distribution Modeling. *Int. J. Hydrogen Energy* **2020,** *45* (2), 1236-1254.

24.   Evans, C. E.; Noble, R. D.; Nazeri-Thompson, S.; Nazeri, B.; Koval, C. A. Role of Conditioning on Water Uptake and Hydraulic Permeability of Nafion® Membranes. *J. Membr. Sci.* **2006,** *279* (1), 521-528.

25.   Peron, J.; Mani, A.; Zhao, X.; Edwards, D.; Adachi, M.; Soboleva, T.; Shi, Z.; Xie, Z.; Navessin, T.; Holdcroft, S. Properties of Nafion® Nr-211 Membranes for Pemfcs. *J. Membr. Sci.* **2010,** *356* (1), 44-51.

26.   Bezmalinović, D.; Radošević, J.; Barbir, F. Initial Conditioning of Polymer Eelectrolyte Membrane Fuel Cell by Temperature and Potential Cycling. *2014* **2014,** *62* (1), 5.

27.   Qi, Z.; Kaufman, A. Quick and Effective Activation of Proton-Exchange Membrane Fuel Cells. *J. Power Sources* **2003,** *114* (1), 21-31.

28.   Balogun, E.; Barnett, A. O.; Holdcroft, S. Cathode Starvation as an Accelerated Conditioning Procedure for Perfluorosulfonic Acid Ionomer Fuel Cells. *J. Power Sources Advances* **2020,** *3*, 100012.

29.   Zhegur-Khais, A.; Kubannek, F.; Krewer, U.; Dekel, D. R. Measuring the True Hydroxide Conductivity of Anion Exchange Membranes. *J. Membr. Sci.* **2020,** *612*, 118461.

30.   Lindquist, G. A.; Xu, Q.; Oener, S. Z.; Boettcher, S. W. Membrane Electrolyzers for Impure-Water Splitting. *Joule* **2020,** *4* (12), 2549-2561.

Chapter III

1.   Lindquist, G. A.; Oener, S. Z.; Krivina, R.; Motz, A. R.; Keane, A.; Capuano, C.; Ayers, K. E.; Boettcher, S. W. Performance and durability of pure-water-fed anion exchange membrane electrolyzers using baseline materials and operation. *ACS Appl. Mater. Interfaces* **2021,** *13* (44), 51917-51924.

2.   Soni, R.; Miyanishi, S.; Kuroki, H.; Yamaguchi, T. Pure water solid alkaline water electrolyzer using fully aromatic and high-molecular-weight poly(fluorene-alt-tetrafluorophenylene)-trimethyl ammonium anion exchange membranes and ionomers. *ACS Appl. Energy Mater.* **2020,** *4* (2), 1053-1058.

3.   Xu, D.; Stevens, M. B.; Cosby, M. R.; Oener, S. Z.; Smith, A. M.; Enman, L. J.; Ayers, K. E.; Capuano, C. B.; Renner, J. N.; Danilovic, N.; Li, Y.; Wang, H.; Zhang, Q.; Boettcher, S. W. Earth-abundant oxygen electrocatalysts for alkaline anion-exchange-membrane water electrolysis: Effects of catalyst conductivity and comparison with performance in three-electrode cells. *ACS Catal.* **2019,** *9* (1), 7-15.

4.   Stevens, M. B.; Enman, L. J.; Korkus, E. H.; Zaffran, J.; Trang, C. D. M.; Asbury, J.; Kast, M. G.; Toroker, M. C.; Boettcher, S. W. Ternary ni-co-fe oxyhydroxide oxygen evolution catalysts: Intrinsic activity trends, electrical conductivity, and electronic band structure. **2019,** *12* (9), 2288-2295.

5.   Stevens, M. B.; Trang, C. D. M.; Enman, L. J.; Deng, J.; Boettcher, S. W. Reactive fe-sites in ni/fe (oxy)hydroxide are responsible for exceptional oxygen electrocatalysis activity. *J. Am. Chem. Soc.* **2017,** *139* (33), 11361-11364.

6.   Trotochaud, L.; Young, S. L.; Ranney, J. K.; Boettcher, S. W. Nickel-iron oxyhydroxide oxygen-evolution electrocatalysts: The role of intentional and incidental iron incorporation. *J. Am. Chem. Soc.* **2014,** *136* (18), 6744-6753.

7.   Chen, P.; Hu, X. High-efficiency anion exchange membrane water electrolysis employing non-noble metal catalysts. *Adv. Energy Mater.* **2020,** *10* (39), 2002285.

8.   Wang, L.; Saveleva, V. A.; Eslamibidgoli, M. J.; Antipin, D.; Bouillet, C.; Biswas, I.; Gago, A. S.; Hosseiny, S. S.; Gazdzicki, P.; Eikerling, M. H.; Savinova, E. R.; Friedrich, K. A. Deciphering the exceptional performance of nife hydroxide for the oxygen evolution reaction in an anion exchange membrane electrolyzer. *ACS Appl. Energy Mater.* **2022**.

9.   Meena, A.; Thangavel, P.; Jeong, D. S.; Singh, A. N.; Jana, A.; Im, H.; Nguyen, D. A.; Kim, K. S. Crystalline-amorphous interface of mesoporous ni2p @ fepoxhy for oxygen evolution at high current density in alkaline-anion-exchange-membrane water-electrolyzer. *Applied Catalysis B: Environmental* **2022,** *306*, 121127.

10.   Mayerhöfer, B.; Speck, F. D.; Hegelheimer, M.; Bierling, M.; Abbas, D.; McLaughlin, D.; Cherevko, S.; Thiele, S.; Peach, R. Electrochemical- and mechanical stability of catalyst layers in anion exchange membrane water electrolysis. *Int. J. Hydrogen Energy* **2022,** *47* (7), 4304-4314.

11.   Li, D.; Park, E. J.; Zhu, W.; Shi, Q.; Zhou, Y.; Tian, H.; Lin, Y.; Serov, A.; Zulevi, B.; Baca, E. D.; Fujimoto, C.; Chung, H. T.; Kim, Y. S. Highly quaternized polystyrene ionomers for high performance anion exchange membrane water electrolysers. *Nat. Energ.* **2020,** *5* (5), 378-385.

12.   Xiao, J.; Oliveira, A. M.; Wang, L.; Zhao, Y.; Wang, T.; Wang, J.; Setzler, B. P.; Yan, Y. Water-fed hydroxide exchange membrane electrolyzer enabled by a fluoride-incorporated nickel–iron oxyhydroxide oxygen evolution electrode. *ACS Catal.* **2021,** *11* (1), 264-270.

13.   Yang, J.; Jang, M. J.; Zeng, X.; Park, Y. S.; Lee, J.; Choi, S. M.; Yin, Y. Non-precious electrocatalysts for oxygen evolution reaction in anion exchange membrane water electrolysis: A mini review. *Electrochem. Commun.* **2021,** *131*, 107118.

14.   Thangavel, P.; Ha, M.; Kumaraguru, S.; Meena, A.; Singh, A. N.; Harzandi, A. M.; Kim, K. S. Graphene-nanoplatelets-supported nife-mof: High-efficiency and ultra-stable oxygen electrodes for sustained alkaline anion exchange membrane water electrolysis. *Energy Environ. Sci.* **2020,** *13* (10), 3447-3458.

15.   Thangavel, P.; Kim, G.; Kim, K. S. Electrochemical integration of amorphous nife (oxy)hydroxides on surface-activated carbon fibers for high-efficiency oxygen evolution in alkaline anion exchange membrane water electrolysis. *J. Mater. Chem. A.* **2021,** *9* (24), 14043-14051.

16.   Hassan, N. U.; Mandal, M.; Zulevi, B.; Kohl, P. A.; Mustain, W. E. Understanding and improving anode performance in an alkaline membrane electrolyzer using statistical design of experiments. *Electrochim. Acta* **2022,** *409*, 140001.

17.   Krivina, R. A.; Lindquist, G. A.; Yang, M. C.; Cook, A. K.; Hendon, C. H.; Motz, A. R.; Capuano, C.; Ayers, K. E.; Hutchison, J. E.; Boettcher, S. W. Three-electrode study of electrochemical ionomer degradation relevant to anion-exchange-membrane water electrolyzers. *ACS Appl. Mater. Interfaces* **2022,** *14* (16), 18261-18274.

18.   Li, D.; Motz, A. R.; Bae, C.; Fujimoto, C.; Yang, G.; Zhang, F.-Y.; Ayers, K. E.; Kim, Y. S. Durability of anion exchange membrane water electrolyzers. *Energy Environ. Sci.* **2021,** *14* (6), 3393-3419.

19.   Martens, I.; Melo, L. G. A.; West, M. M.; Wilkinson, D. P.; Bizzotto, D.; Hitchcock, A. P. Imaging reactivity of the pt–ionomer interface in fuel-cell catalyst layers. *ACS Catal.* **2020,** *10* (15), 8285-8292.

20.   Tao, H. B.; Xu, Y.; Huang, X.; Chen, J.; Pei, L.; Zhang, J.; Chen, J. G.; Liu, B. A general method to probe oxygen evolution intermediates at operating conditions. *Joule* **2019,** *3* (6), 1498-1509.

21.   Hübner, G.; Roduner, E. Epr investigation of ho/ radical initiated degradation reactions of sulfonated aromatics as model compounds for fuel cell proton conducting membranes. *J. Mater. Chem.* **1999,** *9* (2), 409-418.

22.   Wang, J.; Zhao, Y.; Setzler, B. P.; Rojas-Carbonell, S.; Ben Yehuda, C.; Amel, A.; Page, M.; Wang, L.; Hu, K.; Shi, L.; Gottesfeld, S.; Xu, B.; Yan, Y. Poly(aryl piperidinium) membranes and ionomers for hydroxide exchange membrane fuel cells. *Nat. Energ.* **2019,** *4* (5), 392-398.

23.   Berlinger, S. A.; McCloskey, B. D.; Weber, A. Z. Probing ionomer interactions with electrocatalyst particles in solution. *ACS Energy Lett.* **2021,** *6* (6), 2275-2282.

24.   Chung, D. Y.; Lopes, P. P.; Farinazzo Bergamo Dias Martins, P.; He, H.; Kawaguchi, T.; Zapol, P.; You, H.; Tripkovic, D.; Strmcnik, D.; Zhu, Y.; Seifert, S.; Lee, S.; Stamenkovic, V. R.; Markovic, N. M. Dynamic stability of active sites in hydr(oxy)oxides for the oxygen evolution reaction. *Nat. Energ.* **2020,** *5* (3), 222-230.

25.   Zhang, T.; Nellist, M. R.; Enman, L. J.; Xiang, J.; Boettcher, S. W. Modes of fe incorporation in co–fe (oxy)hydroxide oxygen evolution electrocatalysts. *ChemSusChem* **2019,** *12* (9), 2015-2021.

26.   Dette, C.; Hurst, M. R.; Deng, J.; Nellist, M. R.; Boettcher, S. W. Structural evolution of metal (oxy)hydroxide nanosheets during the oxygen evolution reaction. *ACS Appl. Mater. Interfaces* **2019,** *11* (6), 5590-5594.

27.   Biesinger, M. C.; Lau, L. W. M.; Gerson, A. R.; Smart, R. S. C. The role of the auger parameter in xps studies of nickel metal, halides and oxides. *Phys. Chem. Chem. Phys.* **2012,** *14* (7), 2434-2442.

28.   Bergmann, A.; Martinez-Moreno, E.; Teschner, D.; Chernev, P.; Gliech, M.; de Araújo, J. F.; Reier, T.; Dau, H.; Strasser, P. Reversible amorphization and the catalytically active state of crystalline co3o4 during oxygen evolution. *Nat. Commun.* **2015,** *6* (1), 8625.

29.   Wiegmann, T.; Pacheco, I.; Reikowski, F.; Stettner, J.; Qiu, C.; Bouvier, M.; Bertram, M.; Faisal, F.; Brummel, O.; Libuda, J.; Drnec, J.; Allongue, P.; Maroun, F.; Magnussen, O. M. Operando identification of the reversible skin layer on co3o4 as a three-dimensional reaction zone for oxygen evolution. *ACS Catal.* **2022**, 3256-3268.

30.   Deng, J.; Nellist, M. R.; Stevens, M. B.; Dette, C.; Wang, Y.; Boettcher, S. W. Morphology dynamics of single-layered Ni(OH)2/NiOOH nanosheets and subsequent fe incorporation studied by in situ electrochemical atomic force microscopy. *Nano Lett.* **2017,** *17* (11), 6922-6926.

31.   Jinnouchi, R.; Kudo, K.; Kodama, K.; Kitano, N.; Suzuki, T.; Minami, S.; Shinozaki, K.; Hasegawa, N.; Shinohara, A. The role of oxygen-permeable ionomer for polymer electrolyte fuel cells. *Nat. Commun.* **2021,** *12* (1), 4956.

32.   Santoro, C.; Lavacchi, A.; Mustarelli, P.; Di Noto, V.; Elbaz, L.; Dekel, D. R.; Jaouen, F. What is next in anion-exchange membrane water electrolyzers? Bottlenecks, benefits, and future. *Chem Sus Chem 15* (8), e202200027.

33.   Lindquist, G. A.; Xu, Q.; Oener, S. Z.; Boettcher, S. W. Membrane electrolyzers for impure-water splitting. *Joule* **2020,** *4* (12), 2549-2561.

34.   Lu, H.-F.; Chen, H.-F.; Kao, C.-L.; Chao, I.; Chen, H.-Y. A computational study of the fenton reaction in different ph ranges. *Phys. Chem. Chem. Phys.* **2018,** *20* (35), 22890-22901.

Chapter IV

1.   Lohmann-Richters, F. P.; Renz, S.; Lehnert, W.; Müller, M.; Carmo, M. Review—Challenges and Opportunities for Increased Current Density in Alkaline Electrolysis by Increasing the Operating Temperature. *J. Electrochem. Soc.* **2021,** *168* (11), 114501.

2.   Hagesteijn, K. F. L.; Jiang, S.; Ladewig, B. P. A Review of the Synthesis and Characterization of Anion Exchange Membranes. *J. Mater. Sci.* **2018,** *53* (16), 11131-11150.

3.   Suter, T. A. M.; Smith, K.; Hack, J.; Rasha, L.; Rana, Z.; Angel, G. M. A.; Shearing, P. R.; Miller, T. S.; Brett, D. J. L. Engineering Catalyst Layers for Next-Generation Polymer Electrolyte Fuel Cells: A Review of Design, Materials, and Methods. *Adv. Energy Mater.* **2021,** *11* (37), 2101025.

4. Miller, H. A.; Bouzek, K.; Hnat, J.; Loos, S.; Bernäcker, C. I.; Weißgärber, T.; Röntzsch, L.; Meier-Haack, J. Green Hydrogen from Anion Exchange Membrane Water Electrolysis: A Review of Recent Developments in Critical Materials and Operating Conditions. *Sustain. Energ. Fuels.* **2020,** *4* (5), 2114-2133.

5. Ayers, K.; Danilovic, N.; Ouimet, R.; Carmo, M.; Pivovar, B.; Bornstein, M. Perspectives on Low-Temperature Electrolysis and Potential for Renewable Hydrogen at Scale. *Annu. Rev. Chem. Biomol. Eng.* **2019,** *10* (1), 219-239.

6. Li, D.; Motz, A. R.; Bae, C.; Fujimoto, C.; Yang, G.; Zhang, F.-Y.; Ayers, K. E.; Kim, Y. S. Durability of Anion Exchange Membrane Water Electrolyzers. *Energy Environ. Sci.* **2021,** *14* (6), 3393-3419.

7. Kusoglu, A.; Weber, A. Z. New Insights into Perfluorinated Sulfonic-Acid Ionomers. *Chem. Rev.* **2017,** *117* (3), 987-1104.

8. Wan, L.; Liu, J.; Xu, Z.; Xu, Q.; Pang, M.; Wang, P.; Wang, B. Construction of Integrated Electrodes with Transport Highways for Pure-Water-Fed Anion Exchange Membrane Water Electrolysis. *Small* **2022,** *18* (21), 2200380.

9. Krivina, R. A.; Lindquist, G. A.; Beaudoin, S. R.; Stovall, T. N.; Thompson, W. L.; Twight, L. P.; Marsh, D.; Grzyb, J.; Fabrizio, K.; Hutchison, J. E.; Boettcher, S. W. Anode Catalysts in Anion-Exchange-Membrane Electrolysis without Supporting Electrolyte: Conductivity, Dynamics, and Ionomer Degradation. *Adv. Mater.* **2022,** *34* (35), 2203033.

10. Razmjooei, F.; Morawietz, T.; Taghizadeh, E.; Hadjixenophontos, E.; Mues, L.; Gerle, M.; Wood, B. D.; Harms, C.; Gago, A. S.; Ansar, S. A.; Friedrich, K. A. Increasing the Performance of an Anion-Exchange Membrane Electrolyzer Operating in Pure Water with a Nickel-Based Microporous Layer. *Joule* **2021,** *5* (7), 1776-1799.

11. Chen, N.; Paek, S. Y.; Lee, J. Y.; Park, J. H.; Lee, S. Y.; Lee, Y. M. High-Performance Anion Exchange Membrane Water Electrolyzers with a Current Density of 7.68 a Cm−2 and a Durability of 1000 Hours. *Energy Environ. Sci.* **2021,** *14* (12), 6338-6348.

12. Xiao, J.; Oliveira, A. M.; Wang, L.; Zhao, Y.; Wang, T.; Wang, J.; Setzler, B. P.; Yan, Y. Water-Fed Hydroxide Exchange Membrane Electrolyzer Enabled by a Fluoride-Incorporated Nickel–Iron Oxyhydroxide Oxygen Evolution Electrode. *ACS Catal.* **2021,** *11* (1), 264-270.

13. Soni, R.; Miyanishi, S.; Kuroki, H.; Yamaguchi, T. Pure Water Solid Alkaline Water Electrolyzer Using Fully Aromatic and High-Molecular-Weight Poly(Fluorene-Alt-Tetrafluorophenylene)-Trimethyl Ammonium Anion Exchange Membranes and Ionomers. *ACS Appl. Energy Mater.* **2020,** *4* (2), 1053-1058.

14. Li, D. G.; Park, E. J.; Zhu, W. L.; Shi, Q. R.; Zhou, Y.; Tian, H. Y.; Lin, Y. H.; Serov, A.; Zulevi, B.; Baca, E. D.; Fujimoto, C.; Chung, H. T.; Kim, Y. S. Highly Quaternized Polystyrene Ionomers for High Performance Anion Exchange Membrane Water Electrolysers. *Nat. Energ.* **2020,** *5*, 378-385.

15.   Fan, J.; Willdorf-Cohen, S.; Schibli, E. M.; Paula, Z.; Li, W.; Skalski, T. J. G.; Sergeenko, A. T.; Hohenadel, A.; Frisken, B. J.; Magliocca, E.; Mustain, W. E.; Diesendruck, C. E.; Dekel, D. R.; Holdcroft, S. Poly(Bis-Arylimidazoliums) Possessing High Hydroxide Ion Exchange Capacity and High Alkaline Stability. *Nat. Commun.* **2019,** *10* (1), 2306.

16.   Fan, J. T.; Wright, A. G.; Britton, B.; Weissbach, T.; Skalski, T. J. G.; Ward, J.; Peckham, T. J.; Holdcroft, S. Cationic Polyelectrolytes, Stable in 10 M Kohaq at 100 Degrees C. *ACS Macro Lett.* **2017,** *6* (10), 1089-1093.

17.   Hugar, K. M.; Kostalik, H. A.; Coates, G. W. Imidazolium Cations with Exceptional Alkaline Stability: A Systematic Study of Structure-Stability Relationships. *J. Am. Chem. Soc.* **2015,** *137* (27), 8730-8737.

18.   Park, A. M.; Owczarczyk, Z. R.; Garner, L. E.; Yang-Neyerlin, A. C.; Long, H.; Antunes, C. M.; Sturgeon, M. R.; Lindell, M. J.; Hamrock, S. J.; Yandrasits, M.; Pivovar, B. S. Synthesis and Characterization of Perfluorinated Anion Exchange Membranes. *ECS Trans.* **2017,** *80* (8), 957.

19.   Park, E. J.; Maurya, S.; Hibbs, M. R.; Fujimoto, C. H.; Kreuer, K.-D.; Kim, Y. S. Alkaline Stability of Quaternized Diels–Alder Polyphenylenes. *Macromolecules* **2019,** *52* (14), 5419-5428.

20.   Arges, C. G.; Ramani, V. Two-Dimensional Nmr Spectroscopy Reveals Cation-Triggered Backbone Degradation in Polysulfone-Based Anion Exchange Membranes. *Proc. Nat. Acad. Sci.* **2013,** *110* (7), 2490-2495.

21.   Mustain, W. E.; Chatenet, M.; Page, M.; Kim, Y. S. Durability Challenges of Anion Exchange Membrane Fuel Cells. *Energy Environ. Sci.* **2020,** *13* (9), 2805-2838.

22.   Li, D.; Matanovic, I.; Lee, A. S.; Park, E. J.; Fujimoto, C.; Chung, H. T.; Kim, Y. S. Phenyl Oxidation Impacts the Durability of Alkaline Membrane Water Electrolyzer. *ACS Appl. Mater. Interfaces* **2019,** *11* (10), 9696-9701.

23.   Krivina, R. A.; Lindquist, G. A.; Yang, M. C.; Cook, A. K.; Hendon, C. H.; Motz, A. R.; Capuano, C.; Ayers, K. E.; Hutchison, J. E.; Boettcher, S. W. Three-Electrode Study of Electrochemical Ionomer Degradation Relevant to Anion-Exchange-Membrane Water Electrolyzers. *ACS Appl. Mater. Interfaces* **2022,** *14* (16), 18261-18274.

24.   Nemeth, T.; Nauser, T.; Gubler, L. On the Radical Induced Degradation of Quaternary Ammonium Cations for Anion-Exchange Membrane Fuel Cells and Electrolyzers. *ChemSusChem* **2022,** *15* (22), e202201571.

25.   Zhang, Y. Z.; Parrondo, J.; Sankarasubramanian, S.; Ramani, V. Detection of Reactive Oxygen Species in Anion Exchange Membrane Fuel Cells Using in Situ Fluorescence Spectroscopy. *ChemSusChem* **2017,** *10* (15), 3056-3062.

26.   Maurya, S.; Lee, A. S.; Li, D.; Park, E. J.; Leonard, D. P.; Noh, S.; Bae, C.; Kim, Y. S. On the Origin of Permanent Performance Loss of Anion Exchange Membrane Fuel Cells: Electrochemical Oxidation of Phenyl Group. *J. Power Sources* **2019,** *436*, 226866.

27.   Lindquist, G. A.; Oener, S. Z.; Krivina, R.; Motz, A. R.; Keane, A.; Capuano, C.; Ayers, K. E.; Boettcher, S. W. Performance and Durability of Pure-Water-Fed Anion Exchange Membrane Electrolyzers Using Baseline Materials and Operation. *ACS Appl. Mater. Interfaces* **2021,** *13* (44), 51917-51924.

28.   Adler, S. B. Reference Electrode Placement in Thin Solid Electrolytes. *J. Electrochem. Soc.* **2002,** *149* (5), E166.

29.   Zeng, R.; Slade, R. C. T.; Varcoe, J. R. An Experimental Study on the Placement of Reference Electrodes in Alkaline Polymer Electrolyte Membrane Fuel Cells. *Electrochim. Acta* **2010,** *56* (1), 607-619.

30.   Xu, Q.; Oener, S. Z.; Lindquist, G.; Jiang, H.; Li, C.; Boettcher, S. W. Integrated Reference Electrodes in Anion-Exchange-Membrane Electrolyzers: Impact of Stainless-Steel Gas-Diffusion Layers and Internal Mechanical Pressure. *ACS Energy Lett.* **2020,** *6* (2), 305-312.

31.   Vivier, V.; Orazem, M. E. Impedance Analysis of Electrochemical Systems. *Chem. Rev.* **2022,** *122* (12), 11131-11168.

32.   Thermo Fisher Scientific X-Ray Photoelectron Spectroscopy of Atomic Elements. https://www.thermofisher.com/us/en/home/materials-science/learning-center/periodic-table.html (accessed April 7).

33.   Leonard, D. P.; Lehmann, M.; Klein, J. M.; Matanovic, I.; Fujimoto, C.; Saito, T.; Kim, Y. S. Phenyl-Free Polynorbornenes for Potential Anion Exchange Ionomers for Fuel Cells and Electrolyzers. *Adv. Energy Mater.* **2023,** *13* (3), 2203488.

34.   Wu, X.; Chen, N.; Hu, C.; Klok, H.-A.; Lee, Y. M.; Hu, X. Fluorinated Poly(Aryl Piperidinium) Membranes for Anion Exchange Membrane Fuel Cells. *Adv. Mater.* (Published online January 15 2023), 2210432.

35.   Hassan, N.; Zheng, Y.; Kohl, P.; Mustain, W. E. Koh Vs. Deionized Water Operation in Anion Exchange Membrane Electrolyzers. *J. Electrochem. Soc.* **2022,** *169*, 044526.

36.   Huang, G.; Mandal, M.; Hassan, N. U.; Groenhout, K.; Dobbs, A.; Mustain, W. E.; Kohl, P. A. Ionomer Optimization for Water Uptake and Swelling in Anion Exchange Membrane Electrolyzer: Oxygen Evolution Electrode. *J. Electrochem. Soc.* **2020,** *167* (16), 164514.

37.   Huang, G.; Mandal, M.; Hassan, N. U.; Groenhout, K.; Dobbs, A.; Mustain, W. E.; Kohl, P. A. Ionomer Optimization for Water Uptake and Swelling in Anion Exchange Membrane Electrolyzer: Hydrogen Evolution Electrode. *J. Electrochem. Soc.* **2021,** *168* (2), 024503.

38. Ghassemzadeh, L.; Holdcroft, S. Quantifying the Structural Changes of Perfluorosulfonated Acid Ionomer Upon Reaction with Hydroxyl Radicals. *J. Am. Chem. Soc.* **2013,** *135* (22), 8181-8184.

39. Mayerhöfer, B.; McLaughlin, D.; Böhm, T.; Hegelheimer, M.; Seeberger, D.; Thiele, S. Bipolar Membrane Electrode Assemblies for Water Electrolysis. *ACS Appl. Energy Mater.* **2020,** *3* (10), 9635-9644.

40. Mayerhöfer, B.; Ehelebe, K.; Speck, F. D.; Bierling, M.; Bender, J.; Kerres, J. A.; Mayrhofer, K. J. J.; Cherevko, S.; Peach, R.; Thiele, S. On the Effect of Anion Exchange Ionomer Binders in Bipolar Electrode Membrane Interface Water Electrolysis. *J. Mater. Chem. A.* **2021,** *9* (25), 14285-14295.

41. Kern, W. The Evolution of Silicon Wafer Cleaning Technology. *J. Electrochem. Soc.* **1990,** *137* (6), 1887.

42. Li, D.; Park Eun, J.; Zhu, W.; Shi, Q.; Zhou, Y.; Tian, H.; Lin, Y.; Serov, A.; Zulevi, B.; Baca Ehren, D.; Fujimoto, C.; Chung Hoon, T.; Kim Yu, S. Highly Quaternized Polystyrene Ionomers for High Performance Anion Exchange Membrane Water Electrolysers. *Nat. Energ.* **2020,** *5*, 378-385.

43. Maurya, S.; Dumont, J. H.; Villarrubia, C. N.; Matanovic, I.; Li, D.; Kim, Y. S.; Noh, S.; Han, J.; Bae, C.; Miller, H. A.; Fujimoto, C. H.; Dekel, D. R. Surface Adsorption Affects the Performance of Alkaline Anion-Exchange Membrane Fuel Cells. *ACS Catal.* **2018,** *8* (10), 9429-9439.

44. Matanovic, I.; Maurya, S.; Park, E. J.; Jeon, J. Y.; Bae, C.; Kim, Y. S. Adsorption of Polyaromatic Backbone Impacts the Performance of Anion Exchange Membrane Fuel Cells. *Chem. Mater.* **2019,** *31* (11), 4195-4204.

45. Motz, A. R.; Li, D.; Keane, A.; Manriquez, L. D.; Park, E. J.; Maurya, S.; Chung, H.; Fujimoto, C.; Jeon, J.; Pagels, M. K.; Bae, C.; Ayers, K. E.; Kim, Y. S. Performance and Durability of Anion Exchange Membrane Water Electrolyzers Using Down-Selected Polymer Electrolytes. *J. Mater. Chem. A.* **2021,** *9* (39), 22670-22683.

46. Maurya, S.; Fujimoto, C. H.; Hibbs, M. R.; Narvaez Villarrubia, C.; Kim, Y. S. Toward Improved Alkaline Membrane Fuel Cell Performance Using Quaternized Aryl-Ether Free Polyaromatics. *Chem. Mater.* **2018,** *30* (7), 2188-2192.

47. Chung, H. T.; Martinez, U.; Matanovic, I.; Kim, Y. S. Cation–Hydroxide–Water Coadsorption Inhibits the Alkaline Hydrogen Oxidation Reaction. *The Journal of Physical Chemistry Letters* **2016,** *7* (22), 4464-4469.

48. McCrum, I. T.; Hickner, M. A.; Janik, M. J. Quaternary Ammonium Cation Specific Adsorption on Platinum Electrodes: A Combined Experimental and Density Functional Theory Study. *J. Electrochem. Soc.* **2018,** *165* (2), F114.

49. Yamashita, M.; Takamiya, I.; Jin, K.; Nozaki, K. Syntheses and Structures of Bulky Monophosphine-Ligated Methylpalladium Complexes: Application to Homo- and Copolymerization of Norbornene and/or Methoxycarbonylnorbornene. *Organometallics* **2006,** *25* (19), 4588-4595.

50. Selhorst, R.; Gaitor, J.; Lee, M.; Markovich, D.; Yu, Y.; Treichel, M.; Olavarria Gallegos, C.; Kowalewski, T.; Kourkoutis, L. F.; Hayward, R. C.; Noonan, K. J. T. Multiblock Copolymer Anion-Exchange Membranes Derived from Vinyl Addition Polynorbornenes. *ACS Appl. Energy Mater.* **2021,** *4* (9), 10273-10279.

51. Glenn, J. R.; Lindquist, G. A.; Roberts, G. M.; Boettcher, S. W.; Ayers, K. E. Standard Operating Procedure for Post-Operation Component Disassembly and Observation of Benchtop Water Electrolyzer Testing. *Front. Energy Res.* **2022,** *10.*

Chapter V

1. Ayers, K.; Danilovic, N.; Ouimet, R.; Carmo, M.; Pivovar, B.; Bornstein, M. Perspectives on Low-Temperature Electrolysis and Potential for Renewable Hydrogen at Scale. *Annu. Rev. Chem. Biomol. Eng.* **2019,** *10* (1), 219-239.

2. Arges, C. G.; Zhang, L. Anion Exchange Membranes' Evolution toward High Hydroxide Ion Conductivity and Alkaline Resiliency. *ACS Appl. Energy Mater.* **2018,** *1* (7), 2991-3012.

3. Hagesteijn, K. F. L.; Jiang, S.; Ladewig, B. P. A Review of the Synthesis and Characterization of Anion Exchange Membranes. *J. Mater. Sci.* **2018,** *53* (16), 11131-11150.

4. Cao, H.; Pan, J.; Zhu, H.; Sun, Z.; Wang, B.; Zhao, J.; Yan, F. Interaction Regulation between Ionomer Binder and Catalyst: Active Triple-Phase Boundary and High Performance Catalyst Layer for Anion Exchange Membrane Fuel Cells. *Advanced Science* **2021,** *8* (19), 2101744.

5. Lindquist, G. A.; Oener, S. Z.; Krivina, R.; Motz, A. R.; Keane, A.; Capuano, C.; Ayers, K. E.; Boettcher, S. W. Performance and Durability of Pure-Water-Fed Anion Exchange Membrane Electrolyzers Using Baseline Materials and Operation. *ACS Appl. Mater. Interfaces* **2021,** *13* (44), 51917-51924.

6. Li, D. G.; Matanovic, I.; Lee, A. S.; Park, E. J.; Fujimoto, C.; Chung, H. T.; Kim, Y. S. Phenyl Oxidation Impacts the Durability of Alkaline Membrane Water Electrolyzer. *ACS Appl. Mater. Interfaces* **2019,** *11* (10), 9696-9701.

7. Krivina, R. A.; Lindquist, G. A.; Yang, M. C.; Cook, A. K.; Hendon, C. H.; Motz, A. R.; Capuano, C.; Ayers, K. E.; Hutchison, J. E.; Boettcher, S. W. Three-Electrode Study of Electrochemical Ionomer Degradation Relevant to Anion-Exchange-Membrane Water Electrolyzers. *ACS Appl. Mater. Interfaces* **2022,** *14* (16), 18261-18274.

8.   McCrory, C. C. L.; Jung, S.; Peters, J. C.; Jaramillo, T. F. Benchmarking Heterogeneous Electrocatalysts for the Oxygen Evolution Reaction. *J. Am. Chem. Soc.* **2013,** *135* (45), 16977-16987.

9.   Hunter, B. M.; Gray, H. B.; Müller, A. M. Earth-Abundant Heterogeneous Water Oxidation Catalysts. *Chem. Rev.* **2016,** *116* (22), 14120-14136.

10.   Stevens, M. B.; Enman, L. J.; Korkus, E. H.; Zaffran, J.; Trang, C. D. M.; Asbury, J.; Kast, M. G.; Toroker, M. C.; Boettcher, S. W. Ternary Ni-Co-Fe Oxyhydroxide Oxygen Evolution Catalysts: Intrinsic Activity Trends, Electrical Conductivity, and Electronic Band Structure. **2019,** *12* (9), 2288-2295.

11.   Fabbri, E.; Nachtegaal, M.; Binninger, T.; Cheng, X.; Kim, B.-J.; Durst, J.; Bozza, F.; Graule, T.; Schäublin, R.; Wiles, L.; Pertoso, M.; Danilovic, N.; Ayers, K. E.; Schmidt, T. J. Dynamic Surface Self-Reconstruction Is the Key of Highly Active Perovskite Nano-Electrocatalysts for Water Splitting. *Nat. Mater.* **2017,** *16* (9), 925-931.

12.   Wang, K.; Wang, X.; Li, Z.; Yang, B.; Ling, M.; Gao, X.; Lu, J.; Shi, Q.; Lei, L.; Wu, G.; Hou, Y. Designing 3d Dual Transition Metal Electrocatalysts for Oxygen Evolution Reaction in Alkaline Electrolyte: Beyond Oxides. *Nano Energy* **2020,** *77*, 105162.

13.   Mohammed-Ibrahim, J. A Review on Nife-Based Electrocatalysts for Efficient Alkaline Oxygen Evolution Reaction. *J. Power Sources* **2020,** *448*, 227375.

14.   Trotochaud, L.; Young, S. L.; Ranney, J. K.; Boettcher, S. W. Nickel-Iron Oxyhydroxide Oxygen-Evolution Electrocatalysts: The Role of Intentional and Incidental Iron Incorporation. *J. Am. Chem. Soc.* **2014,** *136* (18), 6744-6753.

15.   Stevens, M. B.; Trang, C. D. M.; Enman, L. J.; Deng, J.; Boettcher, S. W. Reactive Fe-Sites in Ni/Fe (Oxy)Hydroxide Are Responsible for Exceptional Oxygen Electrocatalysis Activity. *J. Am. Chem. Soc.* **2017,** *139* (33), 11361-11364.

16.   S. Burke, M.; Zou, S.; J. Enman, L.; E. Kellon, J.; A. Gabor, C.; Pledger, E.; W. Boettcher, S. Revised Oxygen Evolution Reaction Activity Trends for First-Row Transition-Metal (Oxy)Hydroxides in Alkaline Media. *The Journal of Physical Chemistry Letters* **2015,** *6* (18), 3737-3742.

17.   Trotochaud, L.; Ranney, J. K.; Williams, K. N.; Boettcher, S. W. Solution-Cast Metal Oxide Thin Film Electrocatalysts for Oxygen Evolution. *J. Am. Chem. Soc.* **2012,** *134* (41), 17253-17261.

18.   Xu, D.; Stevens, M. B.; Cosby, M. R.; Oener, S. Z.; Smith, A. M.; Enman, L. J.; Ayers, K. E.; Capuano, C. B.; Renner, J. N.; Danilovic, N.; Li, Y.; Wang, H.; Zhang, Q.; Boettcher, S. W. Earth-Abundant Oxygen Electrocatalysts for Alkaline Anion-Exchange-Membrane Water Electrolysis: Effects of Catalyst Conductivity and Comparison with Performance in Three-Electrode Cells. *ACS Catal.* **2019,** *9* (1), 7-15.

19. Krivina, R. A.; Lindquist, G. A.; Beaudoin, S. R.; Stovall, T. N.; Thompson, W. L.; Twight, L. P.; Marsh, D.; Grzyb, J.; Fabrizio, K.; Hutchison, J. E.; Boettcher, S. W. Anode Catalysts in Anion-Exchange-Membrane Electrolysis without Supporting Electrolyte: Conductivity, Dynamics, and Ionomer Degradation. *Adv. Mater.* **2022,** *34* (35), 2203033.

20. Vincent, I.; Lee, E.-C.; Kim, H.-M. Comprehensive Impedance Investigation of Low-Cost Anion Exchange Membrane Electrolysis for Large-Scale Hydrogen Production. *Scientific Reports* **2021,** *11* (1), 293.

21. Chen, N.; Paek, S. Y.; Lee, J. Y.; Park, J. H.; Lee, S. Y.; Lee, Y. M. High-Performance Anion Exchange Membrane Water Electrolyzers with a Current Density of 7.68 a Cm−2 and a Durability of 1000 Hours. *Energy Environ. Sci.* **2021,** *14* (12), 6338-6348.

22. Xiao, J.; Oliveira, A. M.; Wang, L.; Zhao, Y.; Wang, T.; Wang, J.; Setzler, B. P.; Yan, Y. Water-Fed Hydroxide Exchange Membrane Electrolyzer Enabled by a Fluoride-Incorporated Nickel–Iron Oxyhydroxide Oxygen Evolution Electrode. *ACS Catal.* **2021,** *11* (1), 264-270.

23. Razmjooei, F.; Morawietz, T.; Taghizadeh, E.; Hadjixenophontos, E.; Mues, L.; Gerle, M.; Wood, B. D.; Harms, C.; Gago, A. S.; Ansar, S. A.; Friedrich, K. A. Increasing the Performance of an Anion-Exchange Membrane Electrolyzer Operating in Pure Water with a Nickel-Based Microporous Layer. *Joule* **2021,** *5* (7), 1776-1799.

Chapter VI

1. Ayers, K.; Danilovic, N.; Ouimet, R.; Carmo, M.; Pivovar, B.; Bornstein, M. Perspectives on Low-Temperature Electrolysis and Potential for Renewable Hydrogen at Scale. *Annu. Rev. Chem. Biomol. Eng.* **2019,** *10* (1), 219-239.

2. d'Amore-Domenech, R.; Leo, T. J. Sustainable Hydrogen Production from Offshore Marine Renewable Farms: Techno-Energetic Insight on Seawater Electrolysis Technologies. *Acs Sustainable Chemistry & Engineering* **2019,** *7* (9), 8006-8022.

3. Tong, W.; Forster, M.; Dionigi, F.; Dresp Sren, a. Electrolysis of Low-Grade and Saline Surface Water. *Nat. Energ.* **2020**.

4. Dresp, S.; Dionigi, F.; Klingenhof, M.; Strasser, P. Direct Electrolytic Splitting of Seawater: Opportunities and Challenges. *ACS Energy Lett.* **2019,** *4* (4), 933--942.

5. Perveen, R.; Kishor, N.; Mohanty, S. R. Off-Shore Wind Farm Development: Present Status and Challenges. *Renew. Sust. Energ. Rev.* **2014,** *29*, 780-792.

6. Smitha, B.; Sridhar, S.; Khan, A. A. Solid Polymer Electrolyte Membranes for Fuel Cell Applications—a Review. *J. Membr. Sci.* **2005,** *259* (1), 10-26.

7. Satyapal, S. *Us Department of Energy Hydrogen and Fuel Cell Technology Perspectives*; US Department of Energy Office of Energy Efficiency and Renewable Energy: 2019.

8. International, A., Standard Practice for the Preparation of Substitute Ocean Water. 2013; Vol. D1141-98(2013).

9. National Primary Drinking Water Regulations. 2009.

10. Bard, A. J.; Parsons, R.; Jordan, J., *Standard Potentials in Aqueous Solution*. Marcel Dekker, Inc.,New York, NY; None: 1985; p Medium: X; Size: Pages: 846.

11. Vos, J. G.; Liu, Z.; Speck, F. D.; Perini, N.; Fu, W.; Cherevko, S.; Koper, M. T. M. Selectivity Trends between Oxygen Evolution and Chlorine Evolution on Iridium-Based Double Perovskites in Acidic Media. *ACS Catal.* **2019,** *9* (9), 8561-8574.

12. Vos, J. G.; Wezendonk, T. A.; Jeremiasse, A. W.; Koper, M. T. M. MnOx/IrOx as Selective Oxygen Evolution Electrocatalyst in Acidic Chloride Solution. *J. Am. Chem. Soc.* **2018,** *140* (32), 10270-10281.

13. Dionigi, F.; Reier, T.; Pawolek, Z.; Gliech, M.; Strasser, P. Design Criteria, Operating Conditions, and Nickel–Iron Hydroxide Catalyst Materials for Selective Seawater Electrolysis. *ChemSusChem* **2016,** *9* (9), 962--972.

14. Czarnetzki, L. R.; Janssen, L. J. J. Formation of Hypochlorite, Chlorate and Oxygen During Nacl Electrolysis from Alkaline Solutions at an RuO2/TiO2 Anode. *J. Appl. Electrochem.* **1992,** *22* (4), 315-324.

15. Gayen, P.; Saha, S.; Ramani, V. Selective Seawater Splitting Using Pyrochlore Electrocatalyst. *ACS Appl. Energy Mater.* **2020,** *3* (4), 3978-3983.

16. Trześniewski, B. J.; Diaz-Morales, O.; Vermaas, D. A.; Longo, A.; Bras, W.; Koper, M. T. M.; Smith, W. A. In Situ Observation of Active Oxygen Species in Fe-Containing Ni-Based Oxygen Evolution Catalysts: The Effect of pH on Electrochemical Activity. *J. Am. Chem. Soc.* **2015,** *137* (48), 15112-15121.

17. Batchellor, A. S.; Kwon, G.; Laskowski, F. A. L.; Tiede, D. M.; Boettcher, S. W. Domain Structures of Ni and Nife (Oxy)Hydroxide Oxygen-Evolution Catalysts from X-Ray Pair Distribution Function Analysis. *J. Phys. Chem. C* **2017,** *121* (45), 25421-25429.

18. Stevens, M. B.; Trang, C. D. M.; Enman, L. J.; Deng, J.; Boettcher, S. W. Reactive Fe-Sites in Ni/Fe (Oxy)Hydroxide Are Responsible for Exceptional Oxygen Electrocatalysis Activity. *J. Am. Chem. Soc.* **2017,** *139* (33), 11361-11364.

19. Deng, J.; Nellist, M. R.; Stevens, M. B.; Dette, C.; Wang, Y.; Boettcher, S. W. Morphology Dynamics of Single-Layered Ni(OH)2/NiOOH Nanosheets and Subsequent Fe Incorporation Studied by in Situ Electrochemical Atomic Force Microscopy. *Nano Lett.* **2017,** *17* (11), 6922-6926.

20.   Zou, S.; Burke, M. S.; Kast, M. G.; Fan, J.; Danilovic, N.; Boettcher, S. W. Fe (Oxy)Hydroxide Oxygen Evolution Reaction Electrocatalysis: Intrinsic Activity and the Roles of Electrical Conductivity, Substrate, and Dissolution. *Chem. Mater.* **2015,** *27* (23), 8011-8020.

21.   Zhang, T.; Nellist, M. R.; Enman, L. J.; Xiang, J.; Boettcher, S. W. Modes of Fe Incorporation in Co–Fe (Oxy)Hydroxide Oxygen Evolution Electrocatalysts. *ChemSusChem* **2019,** *12* (9), 2015-2021.

22.   Trotochaud, L.; Young, S. L.; Ranney, J. K.; Boettcher, S. W. Nickel-Iron Oxyhydroxide Oxygen-Evolution Electrocatalysts: The Role of Intentional and Incidental Iron Incorporation. *J. Am. Chem. Soc.* **2014,** *136* (18), 6744-6753.

23.   Dresp, S.; Dionigi, F.; Loos, S.; de Araujo, J.; Spri, C.; Gliech, M.; Dau, H.; Strasser, P. Direct Electrolytic Splitting of Seawater: Activity, Selectivity, Degradation, and Recovery Studied from the Molecular Catalyst Structure to the Electrolyzer Cell Level. *Adv. Energy Mater.* **2018,** *8* (22), 1800338.

24.   Dresp, S.; Ngo Thanh, T.; Klingenhof, M.; Brückner, S.; Hauke, P.; Strasser, P. Efficient Direct Seawater Electrolysers Using Selective Alkaline Nife-LDH as Oer Catalyst in Asymmetric Electrolyte Feeds. *Energy Environ. Sci.* **2020,** *13* (6), 1725-1729.

25.   Surendranath, Y.; Dincă, M.; Nocera, D. G. Electrolyte-Dependent Electrosynthesis and Activity of Cobalt-Based Water Oxidation Catalysts. *J. Am. Chem. Soc.* **2009,** *131* (7), 2615-2620.

26.   Keane, T. P.; Nocera, D. G. Selective Production of Oxygen from Seawater by Oxidic Metallate Catalysts. *ACS Omega* **2019,** *4* (7), 12860-12864.

27.   Esswein, A. J.; Surendranath, Y.; Reece, S. Y.; Nocera, D. G. Highly Active Cobalt Phosphate and Borate Based Oxygen Evolving Catalysts Operating in Neutral and Natural Waters. *Energy Environ. Sci.* **2011,** *4* (2), 499-504.

28.   Ghany, N. A. A.; Kumagai, N.; Meguro, S.; Asami, K.; Hashimoto, K. Oxygen Evolution Anodes Composed of Anodically Deposited Mn-Mo-Fe Oxides for Seawater Electrolysis. *Electrochim. Acta* **2002,** *48* (1), 21-28.

29.   El-Moneim, A. A.; Kumagai, N.; Hashimoto, K. Mn-Mo-W Oxide Anodes for Oxygen Evolution in Seawater Electrolysis for Hydrogen Production. *Mater. Trans.* **2009,** *50* (8), 1969-1977.

30.   El-Moneim, A. A. Mn-Mo-W-Oxide Anodes for Oxygen Evolution During Seawater Electrolysis for Hydrogen Production: Effect of Repeated Anodic Deposition. *Int. J. Hydrogen Energy* **2011,** *36* (21), 13398-13406.

31.   Kuang, Y.; Kenney Michael, J.; Meng, Y.; Hung, W.-H.; Liu, Y.; Huang Jianan, E.; Prasanna, R.; Li, P.; Li, Y.; Wang, L.; Lin, M.-C.; McGehee Michael, D.; Sun, X.; Dai, H. Solar-Driven, Highly Sustained Splitting of Seawater into Hydrogen and Oxygen Fuels. *Proc. Nat. Acad. Sci.* **2019,** *116* (14), 6624--6629.

32. Masel, R. I.; Liu, Z.; Sajjad, S. Anion Exchange Membrane Electrolyzers Showing 1 A/cm2 at Less Than 2 V. *ECS Trans.* **2016,** *75* (14), 1143-1146.

33. Zaffran, J. a. Influence of Electrolyte Cations on Ni(Fe)Ooh Catalyzed Oxygen Evolution Reaction. *Chem. Mater.* **2017,** *29* (11), 4761--4767.

34. Bard, A. J.; Faulkner, L. R., *Electrochemical Methods*. Second Edition ed.; John Wiley and Sons, Inc.: Department of Chemistry and Biochemistry, UT Austin, 2001.

35. Diaz-Morales, O. Impurity as a Virtue. *Nat. Energ.* **2020,** *5* (3), 193-194.

36. Chung, D. Y.; Lopes, P. P.; Martins, P.; He, H. Y.; Kawaguchi, T.; Zapol, P.; You, H. D.; Tripkovic, D.; Strmcnik, D.; Zhu, Y. S.; Seifert, S.; Lee, S. S.; Stamenkovic, V. R.; Markovic, N. M. Dynamic Stability of Active Sites in Hydr(Oxy)Oxides for the Oxygen Evolution Reaction. *Nat. Energ.* **2020,** *5* (3), 222-230.

37. Liu, Y. P.; Liang, X.; Gu, L.; Zhang, Y.; Li, G. D.; Zou, X. X.; Chen, J. S. Corrosion Engineering Towards Efficient Oxygen Evolution Electrodes with Stable Catalytic Activity for over 6000 Hours. *Nat. Commun.* **2018,** *9,* 10.

38. Alexander, C. T.; Abakumov, A. M.; Forslund, R. P.; Johnston, K. P.; Stevenson, K. J. Role of the Carbon Support on the Oxygen Reduction and Evolution Activities in Lanio3 Composite Electrodes in Alkaline Solution. *ACS Appl. Energy Mater.* **2018,** *1* (4), 1549-1558.

39. Möller, S.; Barwe, S.; Masa, J.; Wintrich, D.; Seisel, S.; Baltruschat, H.; Schuhmann, W. Online Monitoring of Electrochemical Carbon Corrosion in Alkaline Electrolytes by Differential Electrochemical Mass Spectrometry. *Angewandte Chemie International Edition* **2020,** *59* (4), 1585-1589.

40. Zhang, Y. Z.; Parrondo, J.; Sankarasubramanian, S.; Ramani, V. Detection of Reactive Oxygen Species in Anion Exchange Membrane Fuel Cells Using in Situ Fluorescence Spectroscopy. *ChemSusChem* **2017,** *10* (15), 3056-3062.

41. Hagesteijn, K. F. L.; Jiang, S.; Ladewig, B. P. A Review of the Synthesis and Characterization of Anion Exchange Membranes. *J. Mater. Sci.* **2018,** *53* (16), 11131-11150.

42. Hugar, K. M.; Kostalik, H. A.; Coates, G. W. Imidazolium Cations with Exceptional Alkaline Stability: A Systematic Study of Structure-Stability Relationships. *J. Am. Chem. Soc.* **2015,** *137* (27), 8730-8737.

43. Li, D.; Matanovic, I.; Lee, A. S.; Park, E. J.; Fujimoto, C.; Chung, H. T.; Kim, Y. S. Phenyl Oxidation Impacts the Durability of Alkaline Membrane Water Electrolyzer. *ACS Appl. Mater. Interfaces* **2019,** *11* (10), 9696-9701.

44. Parrondo, J.; Wang, Z.; Jung, M.-S. J.; Ramani, V. Reactive Oxygen Species Accelerate Degradation of Anion Exchange Membranes Based on Polyphenylene Oxide in Alkaline Environments. *Phys. Chem. Chem. Phys.* **2016,** *18* (29), 19705-19712.

45. Park, E. J.; Maurya, S.; Hibbs, M. R.; Fujimoto, C. H.; Kreuer, K.-D.; Kim, Y. S. Alkaline Stability of Quaternized Diels–Alder Polyphenylenes. *Macromolecules* **2019,** *52* (14), 5419-5428.

46. Zhegur, A.; Gjineci, N.; Willdorf-Cohen, S.; Mondal, A. N.; Diesendruck, C. E.; Gavish, N.; Dekel, D. R. Changes of Anion Exchange Membrane Properties During Chemical Degradation. *ACS Appl. Polym. Mater.* **2020,** *2* (2), 360-367.

47. Indusekhar, V. K.; Krishnaswamy, N. Water Transport Studies on Interpolymer Ion-Exchange Membranes. *Desalination* **1985,** *52* (3), 309 - 316.

48. Peng, J.; Roy Asa, L.; Greenbaum Steve, G.; Zawodzinski Thomas, A. Effect of CO2 Absorption on Ion and Water Mobility in an Anion Exchange Membrane. *J. Power Sources* **2018,** *380*, 64--75.

49. Ramaswamy, N.; Hakim, N.; Mukerjee, S. Degradation Mechanism Study of Perfluorinated Proton Exchange Membrane under Fuel Cell Operating Conditions. *Electrochim. Acta* **2008,** *53* (8), 3279--3295.

50. Sugawara, T.; Kawashima, N.; Murakami Takurou, N. Kinetic Study of Nafion Degradation by Fenton Reaction. *J. Power Sources* **2011,** *196* (5), 2615--2620.

51. Gottesfeld, S.; Dekel, D. R.; Page, M.; Bae, C.; Yan, Y.; Zelenay, P.; Kim, Y. S. Anion Exchange Membrane Fuel Cells: Current Status and Remaining Challenges. *J. Power Sources* **2018,** *375*, 170-184.

52. Epsztein, R.; Shaulsky, E.; Qin, M.; Elimelech, M. Activation Behavior for Ion Permeation in Ion-Exchange Membranes: Role of Ion Dehydration in Selective Transport. *J. Membr. Sci.* **2019,** *580*, 316-326.

53. Li, N.; Araya, S. S.; Kær, S. K. Long-Term Contamination Effect of Iron Ions on Cell Performance Degradation of Proton Exchange Membrane Water Electrolyser. *J. Power Sources* **2019,** *434*, 226755.

54. Okada, T. Effect of Ionic Contaminants. *Handbook of Fuel Cells* **2010**.

55. Martens, I.; Melo, L. G. A.; West, M. M.; Wilkinson, D. P.; Bizzotto, D.; Hitchcock, A. P. Imaging Reactivity of the Pt–Ionomer Interface in Fuel-Cell Catalyst Layers. *ACS Catal.* **2020,** *10* (15), 8285-8292.

56. Stanislaw, L. N.; Gerhardt Michael, R.; Weber Adam, Z. Modeling Electrolyte Composition Effects on Anion-Exchange-Membrane Water Electrolyzer Performance. *ECS Trans.* **2019,** *92* (8), 767-779.

57. Newman, J. Thermoelectric Effects in Electrochemical Systems. *Industrial and Engineering Chemistry Research* **1995,** *34* (10).

58. Mier, M. P.; Ibañez, R.; Ortiz, I. Influence of Ion Concentration on the Kinetics of Electrodialysis with Bipolar Membranes. *Sep. Purif. Technol.* **2008,** *59* (2), 197-205.

59.   Strathmann, H. Electrodialysis, a Mature Technology with a Multitude of New Applications. *Desalination* **2010,** *264* (3), 268-288.

60.   Xu, T.; Huang, C. Electrodialysis-Based Separation Technologies: A Critical Review. *AIChE J.* **2008,** *54* (12), 3147-3159.

61.   Mei, Y.; Tang, C. Y. Recent Developments and Future Perspectives of Reverse Electrodialysis Technology: A Review. *Desalination* **2018,** *425*, 156-174.

62.   Campione, A.; Gurreri, L.; Ciofalo, M.; Micale, G.; Tamburini, A.; Cipollina, A. Electrodialysis for Water Desalination: A Critical Assessment of Recent Developments on Process Fundamentals, Models and Applications. *Desalination* **2018,** *434*, 121-160.

63.   Al-Amshawee, S.; Yunus, M. Y. B. M.; Azoddein, A. A. M.; Hassell, D. G.; Dakhil, I. H.; Hasan, H. A. Electrodialysis Desalination for Water and Wastewater: A Review. *Chemical Engineering Journal* **2020,** *380*, 122231.

64.   Luo, T.; Abdu, S.; Wessling, M. Selectivity of Ion Exchange Membranes: A Review. *J. Membr. Sci.* **2018,** *555*, 429-454.

65.   Sata, T. Studies on Anion Exchange Membranes Having Permselectivity for Specific Anions in Electrodialysis – Effect of Hydrophilicity of Anion Exchange Membranes on Permselectivity of Anions. *J. Membr. Sci.* **2000,** *167* (1), 1-31.

66.   Moussaoui, R. E.; Pourcelly, G.; Maeck, M.; Hurwitz, H. D.; Gavach, C. Co-Ion Leakage through Bipolar Membranes Influence on I–V Responses and Water-Splitting Efficiency. *J. Membr. Sci.* **1994,** *90* (3), 283-292.

67.   Fernandez-Gonzalez, C.; Dominguez-Ramos, A.; Ibañez, R.; Irabien, A. Electrodialysis with Bipolar Membranes for Valorization of Brines. *Separation & Purification Reviews* **2016,** *45* (4), 275-287.

68.   Park, A. M.; Owczarczyk, Z. R.; Garner, L. E.; Yang-Neyerlin, A. C.; Long, H.; Antunes, C. M.; Sturgeon, M. R.; Lindell, M. J.; Hamrock, S. J.; Yandrasits, M.; Pivovar, B. S. Synthesis and Characterization of Perfluorinated Anion Exchange Membranes. *ECS Trans.* **2017,** *80* (8), 957.

69.   Li, D.; Park, E. J.; Zhu, W.; Shi, Q.; Zhou, Y.; Tian, H.; Lin, Y.; Serov, A.; Zulevi, B.; Baca, E. D.; Fujimoto, C.; Chung, H. T.; Kim, Y. S. Highly Quaternized Polystyrene Ionomers for High Performance Anion Exchange Membrane Water Electrolysers. *Nat. Energ.* **2020,** *5* (5), 378-385.

70.   Oener, S. Z.; Ardo, S.; Boettcher, S. W. Ionic Processes in Water Electrolysis: The Role of Ion-Selective Membranes. *ACS Energy Lett.* **2017,** *2* (11), 2625-2634.

71.   Oener, S. Z.; Foster, M. J.; Boettcher, S. W. Accelerating Water Dissociation in Bipolar Membranes and for Electrocatalysis. *Science* **2020,** *369* (6507), 1099.

72. Blommaert, M. A.; Verdonk, J. A. H.; Blommaert, H. C. B.; Smith, W. A.; Vermaas, D. A. Reduced Ion Crossover in Bipolar Membrane Electrolysis Via Increased Current Density, Molecular Size, and Valence. *ACS Appl. Energy Mater.* **2020**.

73. Oener, S. Z.; Twight, L. P.; Lindquist, G. A.; Boettcher, S. W. Thin Cation-Exchange Layers Enable High-Current-Density Bipolar Membrane Electrolyzers Via Improved Water Transport. *ACS Energy Lett.* **2021,** *6* (1), 1-8.

74. Mayerhöfer, B.; McLaughlin, D.; Böhm, T.; Hegelheimer, M.; Seeberger, D.; Thiele, S. Bipolar Membrane Electrode Assemblies for Water Electrolysis. *ACS Appl. Energy Mater.* **2020,** *3* (10), 9635-9644.

75. Jaramillo, T. F.; Jorgensen, K. P.; Bonde, J.; Nielsen, J. H.; Horch, S.; Chorkendorff, I. Identification of Active Edge Sites for Electrochemical H2 Evolution from MoS2 Nanocatalysts. *Science* **2007,** *317* (5834), 100-102.

Appendix C

1. J. C. Gaitor, M. Treichel, T. Kowalewski and K. J. T. Noonan, *ACS Appl. Polym. Mater.*, 2022, **4**, 8032-8042.

2. M. Treichel, C. Tyler Womble, R. Selhorst, J. Gaitor, T. M. S. K. Pathiranage, T. Kowalewski and K. J. T. Noonan, *Macromolecules*, 2020, **53**, 8509-8518.

3. R. Selhorst, J. Gaitor, M. Lee, D. Markovich, Y. Yu, M. Treichel, C. Olavarria Gallegos, T. Kowalewski, L. F. Kourkoutis, R. C. Hayward and K. J. T. Noonan, *ACS Appl. Energy Mater.*, 2021, **4**, 10273-10279.

4. J. Wang, Y. Zhao, B. P. Setzler, S. Rojas-Carbonell, C. Ben Yehuda, A. Amel, M. Page, L. Wang, K. Hu, L. Shi, S. Gottesfeld, B. Xu and Y. Yan, *Nat. Energ.*, 2019, **4**, 392-398.